LMSC
NSP
63-96 VOL 3

NSP-63-96-VOL 3 • NOV 1963

NSP-63-96-VOL 3

N64-24017
CODE-1
NASA CR 56646
Cat. 27

RIFT SYSTEMS ANALYSIS

VOL 3 AERODYNAMICS

Report 201, Contract NAS 8-5600

OTS PRICE

XEROX $ 9.60 ph

MICROFILM $ ________

NSP-63-96-VOL 3 • NOV 1963

NSP-63-96-VOL 3

RIFT SYSTEMS ANALYSIS

VOL 3 AERODYNAMICS

Report 201, Contract NAS 8-5600

Approved A. J. Steele
A. J. STEELE, Director
NSP Engineering

H. F. Plank
H. F. PLANK, Director
Nuclear Space Programs
Space Programs Division

Lockheed

MISSILES & SPACE COMPANY

A GROUP DIVISION OF LOCKHEED AIRCRAFT CORPORATION

SUNNYVALE, CALIFORNIA

S94-15313

Abstract

~~FOREWORD~~

2.4017

This volume of RIFT Systems Analysis, NSP-63-96, presents the results of aerodynamic analysis for the Saturn VN launch vehicles, both RIFT and operational, which are applicable to the 176,000-lb impulse propellant capacity S-N stage. The aerodynamic characteristics are obtained by a combination of theoretical methods and available scale-model experimental test data. The information included here covers aerodynamic data for the areas of stability and control, performance, and drag; data for structural design; data for ground transporter design; and jet wake characteristics of secondary propulsion systems.

AUTHOR Author

RIFT Systems Analysis. NSP-63-96, is submitted in accordance with the requirements of Report No. 201 of the Data Submittal Document, NSP-63-94, dated 3 August 1963. The eight-volume report constitutes the analysis summary of the second design iteration, with the S-N stage size of 176,000 impulse propellant capacity. Analyses establishing stage, support-system, and test requirements are reported. Intermediate reports which have been published regarding selected analytical areas are referenced as appropriate.

Because of the number of technical disciplines, the range of security classification, and amount of material to be documented, this report is divided into discrete volumes. The volume breakdown is as follows:

Volume	Title
1	Vehicle Description and Summary
2	Flight Performance
3	Aerodynamics
4	Flight Dynamics and Control
5	Propulsion
6	Nucleonics
7	Thermodynamics
8	Structural Loads

The participation of the Aero-Mechanics organization of the LMSC Research and Engineering Division in the preparation of this report is acknowledged. This organization has provided technical support in aerodynamics to Nuclear Space Programs for the development effort in the RIFT Program.

SUMMARY

Aerodynamic characteristics for the Saturn VN Reactor-In-Flight-Test (RIFT) and operational vehicle configurations, ML 471-105(01) and -5(01), are presented in this report. The intent is to present a summary of the aerodynamic effort as applied to these configurations embodying the 176,000 lb impulse propellant.

The areas of aerodynamic study concerned the following major areas:

- Stability and Control
- Performance and Drag
- Aerodynamics for Structural Design
- Aerodynamics for Ground Transporters Design
- Rocket Plume Investigations

Theoretical analyses were combined with experimental results (when available) to provide the required information. The span of aerodynamic analyses extended from the subsonic incompressible flow regime to the free-molecule flow regime.

Linear and non-linear aerodynamic characteristics which include normal force and center-of-pressure characteristics were utilized for evaluation of vehicle stability and for trajectory calculation. Primarily, initial trajectory calculations utilized the linear aerodynamic coefficients. These characteristics have been established through use of theory and experimental test results.

Aerodynamics in orbit were calculated for use in control system design analysis of the S-N stage (RIFT). The aerodynamic analysis concerned the free-molecular flow regime, and free-molecule flow methods developed at LMSC were utilized. Although air is extremely rarified at orbital altitudes, an aerodynamic moment exists and was accounted for in the analysis.

Preliminary calculations determined the venting orifice size required to alleviate aerodynamic forces on the 20-deg nose fairing for the first-stage flight to be 1.6 sq ft to vent a 27,622 cu ft volume and maintain a 2.0 psid, $(P_{inside} - P_{outside})$, for the entire flight.

Hypersonic aerodynamics in the continuum flow regime were calculated for application to the stage separation problem. Inclusion of the aerodynamic forces in a separation study showed their effect to be negligible due to the extremely low dynamic pressures existing at separation.

Axial force (drag) characteristics were established including effects of base aspiration and recirculation as well as protuberance drag values. Integrated velocity loss due to drag is 142 fps for the RIFT vehicle (lob) trajectory, 194 fps for the Saturn VN operational vehicle suborbital start trajectory, and 172 fps for the orbital start trajectory.

A special study was conducted to determine the effect of drag increments on payload capability. For the 176,000-lb capacity stage, using a suborbit start mode, the payload trade-off is -49 lb/percent increase in drag coefficient for a 72-hr lunar transfer mission. Side effects caused by protuberances – such as buffeting, noise and localized heating – must be considered. Protuberance test results, including effects of heating and oscillating pressures, are expected to be available in 1964.

Normal force and pressure distributions along the body in the region of maximum dynamic pressure were calculated for use in structural design. Fluctuating pressures caused by engine noise, boundary-layer noise, and local shocks were estimated throughout the complete Mach range.

To date, steady-state launch pad forces are based upon analytical analysis and test results of dynamically scaled models. Wind tunnel test results on Saturn V configurations will be available shortly and will be considered for any further estimates. A method has been selected for calculating the oscillatory aerodynamic forces which act in a direction transverse to the wind vector. The method gives results which are to be used in a preliminary design capacity only.

Drag characteristics for the overland transporter (truck-trailer) configuration and drag and oscillatory lift characteristics of the onsite transporter were estimated. These results are being used for determining the overturning moments and stability within a specified ground wind environment. Estimations of the oscillatory transverse aerodynamic forces on the vertical onsite transporter show that for frequencies of approximately one cps, the magnitude is of the same order as the steady drag forces.

Aerodynamic characteristics at liftoff were estimated for angles-of-attack from 0 to 90 deg. These coefficients, normal force, and center-of-pressure are for use in determining stability and control as the vehicle leaves the launch pad.

The jet wake from the attitude control jets has been determined for the range of operating conditions for the cold-gas reaction-jet attitude-control system. These plume characteristics are being used as a guide to the placement of this system on the S-N stage. A similar investigation of interstage retrorocket exhaust impingement was conducted to determine feasibility of submerged retrorocket installation designs.

CONTENTS

ILLUSTRATIONS

CONFIGURATION DESIGNATION

Where applicable, stage and vehicle configurations defined in this report are identified by model numbers to specify the different arrangements designated for engineering design and analysis. The basic LMSC model number assigned to the S-N Stage (RIFT) Program is ML 471. The different S-N stage models, vehicles, and flights are identified by a sequential series of dash numbers attached to the basic model number.

The S-N stage model numbers are of the form:

ML 471-XXX

- XXX — S-N stage number
- ML 471 — Program number

The first component attached to the basic model number identifies the S-N stage model. A new stage number is assigned upon significant variation of any of the stage elements. S-N stage numbers from ML 471-1 through ML 471-99 designate models associated with the operational vehicle; model numbers ML 471-101 and subsequent designate RIFT models.

The vehicle and flight or mission numbers are of the form:

ML 471-XXX (XX-XX)

- second XX — Flight or mission number
- first XX — Vehicle number

The next component of the model number is the vehicle number, designating a particular Saturn VN launch vehicle. For a particular S-N stage model, a new vehicle number is assigned upon significant physical or functional variation in any of the vehicle elements. Thus the operational launch vehicles associated with the first S-N stage model are designated by ML 471-1(01) and subsequent, while the RIFT launch vehicles associated with the first S-N stage model are designated by ML 471-101(01) and subsequent.

The final component of the model number is the flight or mission number. For a specific vehicle configuration number, significant flight trajectories or mission programs are identified by ML 471-XXX(XX-01) and subsequent.

DIMENSIONAL UNIT CONVERSION FACTORS

Quantity	Multiply	By	To Obtain
Acceleration	ft/sec^2	3.04800×10^{-1}	m/sec^2
Area	$in.^2$	6.45160×10^{-4}	m^2
	ft^2	9.29030×10^{-2}	m^2
Density	$\frac{lb\text{-}sec^2}{ft^4}$	5.25539×10^{1}	$\frac{kg\text{-}sec^2}{m^4}$
	$slug/ft^3$	5.25539×10^{1}	$\frac{kg\text{-}sec^2}{m^4}$
Energy	Btu	2.51996×10^{-1}	kcal
Force	lb	4.53592×10^{-1}	kg
Length	in.	2.54000×10^{-2}	m
	ft	3.0480×10^{-1}	m
Mass	$\frac{lb\text{-}sec^2}{ft}$	1.48816	$\frac{kg\text{-}sec^2}{m}$ = TMU
Mass Flow Rate	$\frac{lb\text{-}sec}{ft}$	1.48816	$\frac{kg\text{-}sec}{m}$
Pressure	$lb/in.^2$	7.03067×10^{-2}	kg/cm^2
	lb/ft^2	4.882×10^{-4}	kg/cm^2
Temperature	°F −32	5.55556×10^{-1}	°C
Velocity	ft/sec	3.04800×10^{-1}	m/sec
Volume	gal (U.S.)	3.78543×10^{-3}	m^3
	ft^3	2.83168×10^{-2}	m^3
Volume Flow	ft^3/sec	2.83168×10^{-2}	m^3/sec
	gal/sec	3.78543×10^{-3}	m^3/sec

NOTATIONS

A'	Area weighting factor
α	Angle-of-attack
β	$\sqrt{M^2 - 1}$
C	Coefficient
C_A	Axial force coefficient $= \frac{\text{Axial force}}{qS}$
C_D	Drag coefficient $\sim \frac{\text{DRAG}}{qS}$
C_L	Lift coefficient
C'_L	dC_L/dX (Local lift)
C_m	Pitching moment coefficient $= \left(\frac{\text{Pitching moment}}{qSD}\right)$
$Cm_{\bar{q}}$	Pitching damping derivative $= \frac{dCm}{d\left(\frac{\dot{\theta}D}{v}\right)}$
C_N	$\frac{\text{Normal force}}{qS}$
C_{N_α}	Normal force derivative, $\frac{dC_N}{d\alpha}$
C_p	Pressure Coefficient $= \frac{p - p_\infty}{q^\infty}$
D	Reference diameter, 33 ft
$\frac{dC_{N_\alpha}}{dX}$	Normal force curve slope distribution along the body, per degree, per inch
Δ	Maximum
δ	Instantaneous body deflection

η	Fineness ratio drag factor
$\dot{\theta}$	Pitch rate, $\frac{d\theta}{dt}$
f	Frequency, cps
K	Constant of proportionality
K_{B_F}	Interference factor due to fins
L	Length
M	Mach number
μ	Mass ratio
p	Static pressure
$\overline{p}$ or P_{rms}	Root-mean-square fluctuating pressure
p_e	Engine exit pressure
P_∞	Ambient pressure
q	Dynamic pressure, $\frac{1}{2} \rho V^2$
R	Fin aspect ratio $\sim$ $(\text{span})^2/\text{area}$
r	Span measured from body centerline
RE, RN	Reynolds number
rms	Root-mean-square
ρ	Density
S	Reference area $\sim \frac{\pi}{4} (33)^2 \sim \text{ft}^2$
(S)	Molecular speed ratio $= \frac{V}{\sqrt{2.0\ RT}}$
σ_1	Body deflection
T	Temperature, °R
V	Flight velocity

X	Axial coordinate along body centerline
X_{CP}	Center-of-pressure
2.0 RT	Most probable molecular speed
α'	Thermal accommodation coefficient
X_{MC}	Moment center

SUBSCRIPTS

c	Cone
B_F	Lift carryover onto body
F	Isolated fin
F_B	Induced lift on fin due to body-shroud upwash
i	Induced
o	Zero time
P	Protuberance based on added area
p_B	Base pressure (average)
S	Isolated shroud
S_B	Induced lift on shroud due to body upwash
S_F	Induced lift on shroud due to the fin
S_{ref}	Body reference area, 855 ft^2
∞	Refers to free-stream conditions

SYMBOLS

∂	Partial derivative
$>$	Greater than
$>>$	Much greater than
$<$	Less than
$\ll$	Much less than
$\approx$	Approximately equals

Section 1
INTRODUCTION

A summary of the aerodynamic effort expended on the Saturn VN Reactor-In-Flight-Test (RIFT) and Saturn VN operational vehicles employing the 176,000-lb impulse propellant and a resume of the various areas of aerodynamic work are presented in this report. The results are based upon available test results accomplished to date.

Thus far, all wind tunnel tests have been conducted on small-scale models. The full-scale RIFT vehicle is very large, thus duplication of full-scale Reynolds numbers in these tests has not been accomplished. Reynolds numbers are believed to be sufficiently high to negate any scale effects; however, determination of the validity of this assumption will depend upon future larger scale tests.

The correlation of estimated aerodynamic characteristics with available experimental data is shown.

In general, most areas of study did not have directly applicable test data. Only in the areas of linear aerodynamics were data available for the RIFT vehicle configuration. Aerodynamics in orbit, used for application in control system design of the S-N stage, employed only free-molecule flow theory. For determining linear and non-linear aerodynamics for the Saturn VN operational vehicle, base flow characteristics, normal force and pressure distributions, fluctuating pressures, and launch pad forces, a combination of theory and data correlations for similar configurations was utilized.

Where test results were unavailable, methods of analysis suitable for preliminary design were devised.

Precise evaluation of aerodynamic characteristics in determining launch pad transverse oscillatory aerodynamic coefficients has been one of the most difficult areas to analyze. To date, no completely satisfactory solution has been determined, and reliance is placed on experimental results. These transverse oscillatory forces are completely random for the Saturn V vehicles, and the importance of correctly establishing their magnitude is that they may establish structural design criteria rather than the maximum dynamic-pressure inflight condition.

Section 2
AERODYNAMIC FLOW REGIMES

Aerodynamic flow regimes which the Saturn VN Reactor-In-Flight-Test (RIFT) and operational vehicles encounter extend from the incompressible flow regime (Mach number $\approx$ 0) while the vehicle is sitting on the launch pad to the free-molecular flow regime when the S-N stage (RIFT) is in orbit. Theoretical methods are available for aerodynamic analysis throughout most of these regions. In the transonic region, theoretical solutions are not available, and reliance is placed on experimental results and on correlations of experimental results. The various flight regimes are shown in Fig. 2-1 along with the Saturn VN RIFT and operational vehicles (orbital and suborbital) trajectory characteristics up to S-N stage separation. Note that the dynamic pressure is essentially zero for all three trajectories at the beginning of the slip flow regime.

The flow regime boundaries are defined in terms of the ratio of the mean free path of the air molecules to a characteristic body dimension. If the mean free path is small compared to the body dimension, the air is considered to be a continuum. When the air is sufficiently rarefied, the molecules next to the surface no longer adhere but "slip" over the surface at a specific velocity. This type of flow is slip flow and is the regime immediately following the continuum regime.

The two boundaries for the onset of slip flow are given as:

For Reynolds numbers << than 1.0,

$$\frac{M}{RE_L} = 0.01$$

For Reynolds numbers >> than 1.0,

$$\frac{M}{\sqrt{RE_L}} = 0.01$$

where:

RE_L = Reynolds number based on body length, L
M = Mach number

The upper limit of the slip regime is defined where $\frac{M}{\sqrt{RE_L}} \approx 1.0$. Between slip flow and free-molecule flow is the transition regime where molecule-molecule interaction and molecule-body interaction are equally probable.

When the mean free path of the air molecules is much larger than the body dimensions, free-molecule flow exists. The boundary of free-molecule flow is given as:

$$\frac{M}{RE_L} > 10 \ , \ RE << 1.0$$

In free-molecule flow, the chance of molecule-molecule collision is much less than of molecule-body collision.

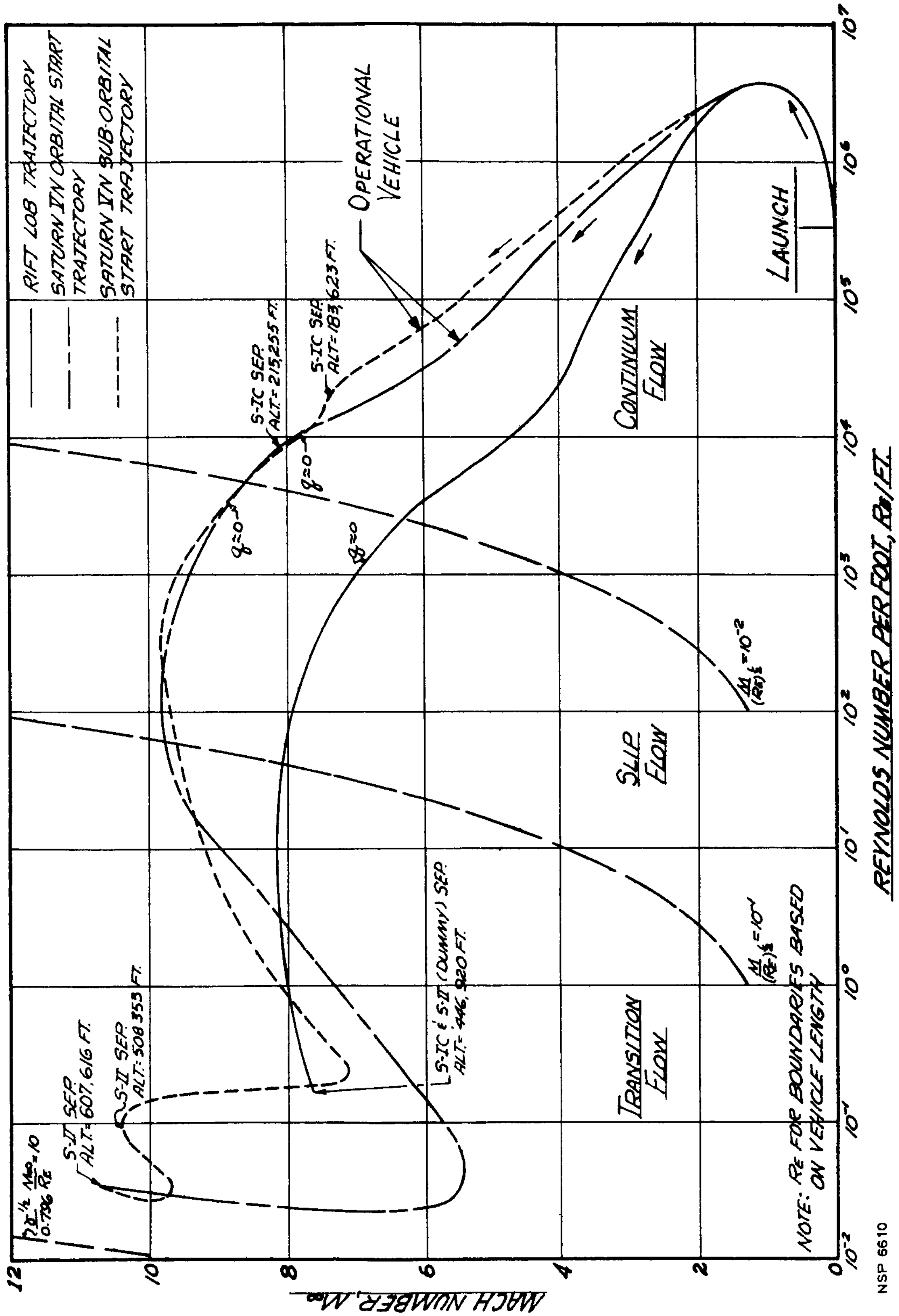

Fig. 2-1 Saturn VN RIFT and Operational Vehicles Aerodynamics Flow Regimes

Section 3
STABILITY AND CONTROL

3.1 LINEAR AERODYNAMIC CHARACTERISTICS

The normal force curve slope and center-of-pressure characteristics presented in this section were calculated in support of the effort to size the operational vehicle and are representative of aerodynamic estimates of the basic vehicles to date. Figure 3-1 shows RIFT and operational vehicles (Configs.: D – RIFT lob; and E – operational) configuration details for which these estimates were made. Note that Config. D is the Saturn VN RIFT vehicle encompassing the S-N stage (Reactor-In-Flight-Test – RIFT). This figure also shows configurations for which test data are available.

Figure 3-2 presents the normal force curve slope, C_{N_α}, for the complete RIFT vehicle. The slopes are shown versus Mach number and are based upon the correlation of all analytical and experimental results available to date. Experimental results were taken from Refs. 1 through 4.*

Those experimental results from Refs. 1 and 2 were used for establishing fin and shroud characteristics; the design curve shown is the most representative fairing of all the test data. For the complete configuration, most emphasis was placed on the P34 test data (Refs. 3 and 4). Normal force curve slope for the RIFT vehicle body-alone is indicated in Fig. 3-3. The design curve for the body-alone is assumed to follow the test data of Ref. 5 from Mach numbers 0.7 to 2.0; Allen's viscous cross-force theory, Ref. 6, for incompressible flow and design correlation curves at Mach number 3.0; and experimental data of Ref. 7 at Mach number 6.86. No emphasis was placed on the subsonic test data from the P34 test, because the results were erratic.

Supersonic results from the P34 test have the same trend versus Mach number, and the curves are slightly higher than the design curve. Normal force characteristics for the fins-plus-shrouds-plus carryover force on the body are shown in Fig. 3-4. The

*See Section 8 for list of references.

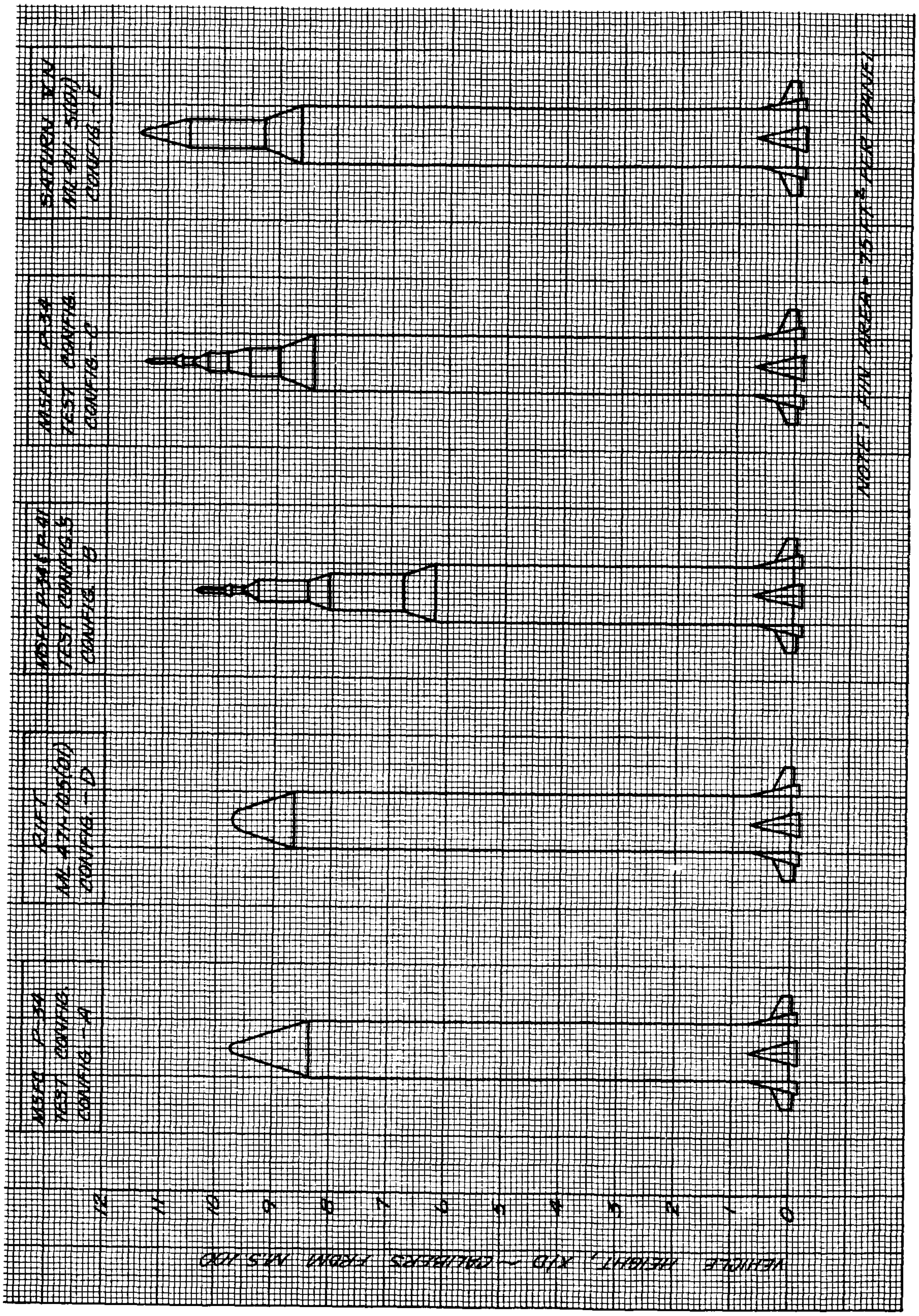

NSP 6611

Fig. 3-1 Configuration Details for Saturn VN RIFT and Operational Vehicles and Wind Tunnel Test Models

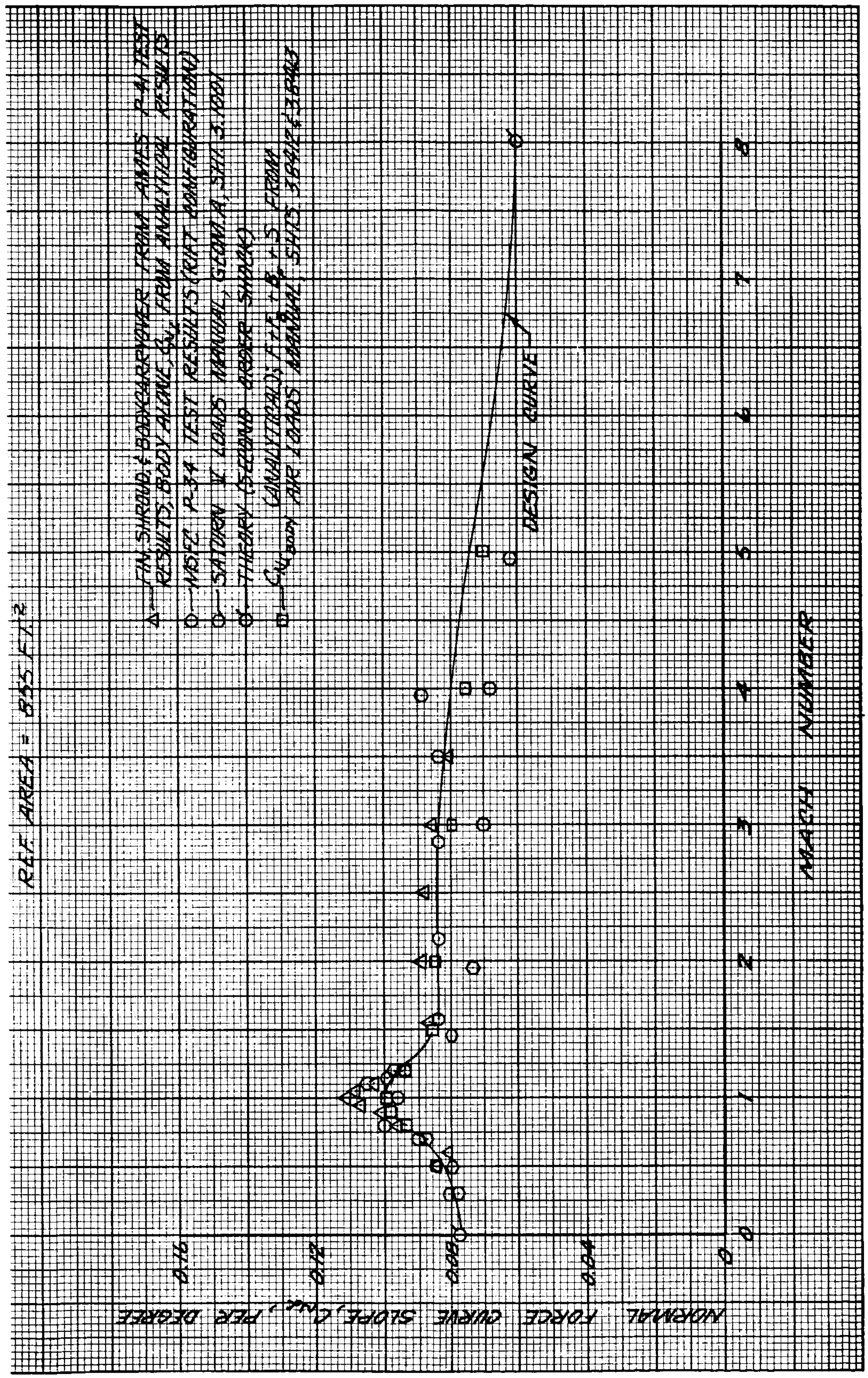

Fig. 3-2 RIFT Vehicle Normal Force Curve Slope versus Mach Number

NSP 6612

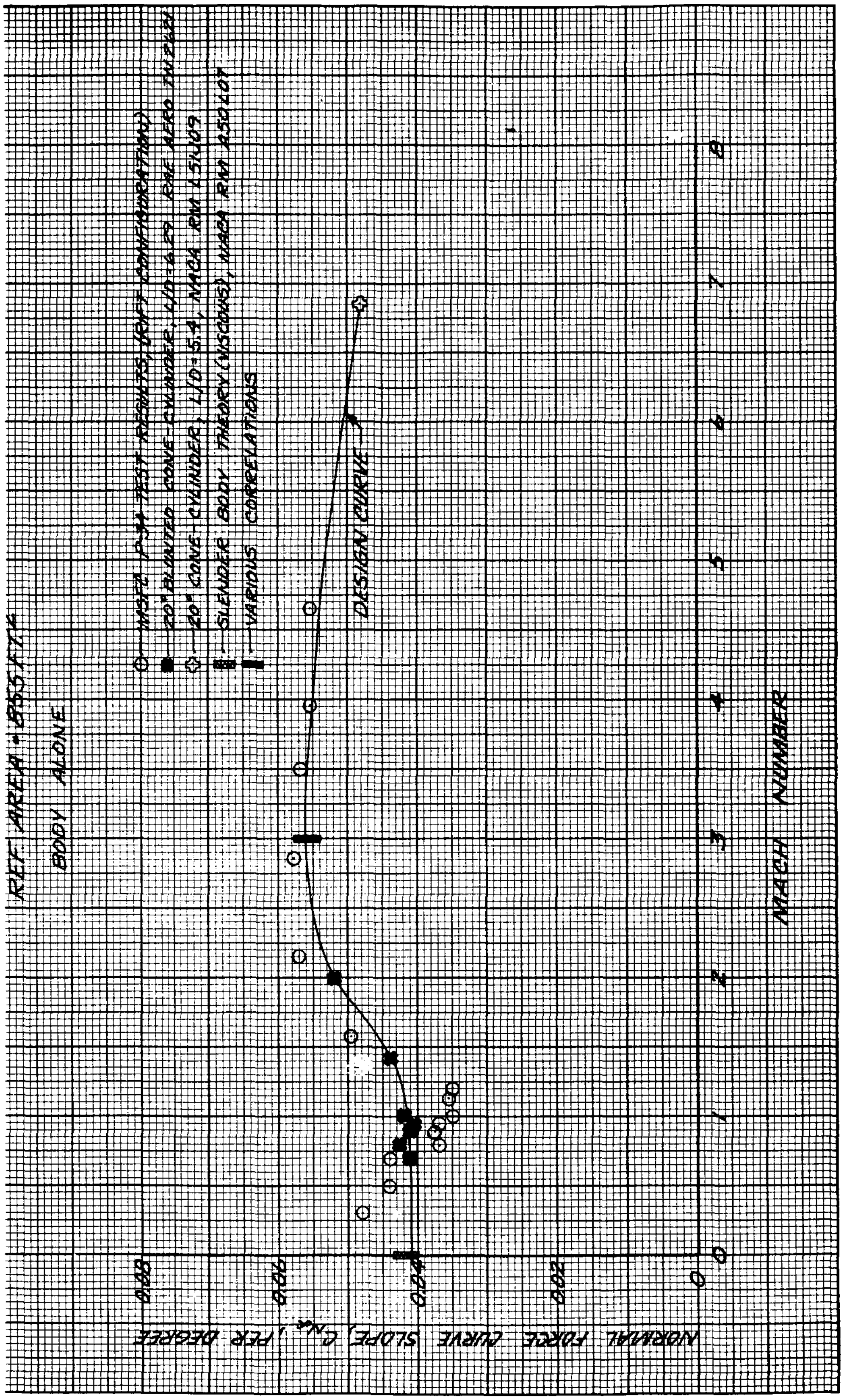

Fig. 3-3 RIFT Vehicle Body-Alone Normal Force Curve Slope versus Mach Number

NSP 6613

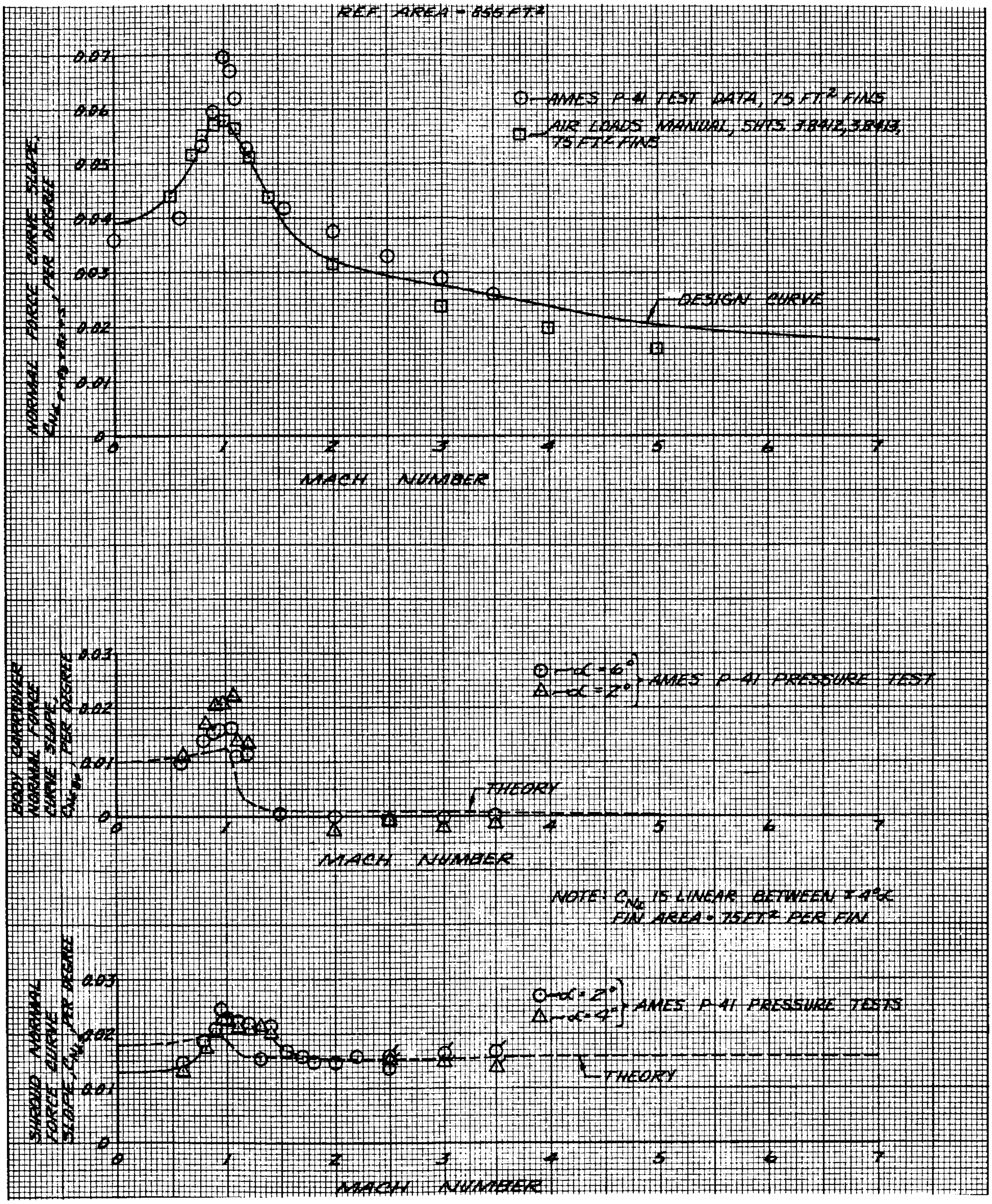

NSP 6614

Fig. 3-4 RIFT Vehicle Tail Section Normal Force Curve Slope versus Mach Number design fin normal force values are simply the difference between the total configuration value (Fig. 3-2) and the body-alone values (Fig. 3-3). These values are compared with small-scale test results obtained from Refs. 1 and 2.

In Fig. 3-4, theoretical and experimental engine-shroud normal force derivatives versus Mach number are also shown. The experimental results are from Ref. 1 and show extremely good agreement between theory and experiment for Mach numbers > 1.5. For Mach numbers < 1.5, the comparison with test data is acceptable only on an order-of-magnitude basis. Fin and shroud carryover lift on the body area (extending between the shrouds and fins) are also presented in Fig. 3-4. Again, the theoretical results are compared with test results from Ref. 1 and the comparison is quite satisfactory. Theoretical methods for calculating fin, shroud, and body carryover effects are described at the end of this section.

Normal force derivative, C_{N_α}, for the complete Saturn VN operational vehicle configuration is presented in Fig. 3-5. The body lift was determined from Allen's viscous cross-force theory (Ref. 6) for incompressible flow while in the transonic range data of Ref. 8 and experimental correlations for cone-cylinders were used. Experimental results for configuration CM-1 in Ref. 2 show good agreement with the estimates.

At supersonic speeds, second-order shock-expansion theory, tangent cone approximations, and empirical results from Ref. 8 and design curves were correlated. Modified Newtonian theory and the correlations of Ref. 9 were applied at hypersonic Mach numbers. The tail-section normal force characteristics are the same as those for the RIFT vehicle described previously.

Center-of-pressure variation with Mach number for the complete RIFT vehicle and for the tail section is presented in Fig. 3-6. The center-of-pressure location for the body carryover force was determined by observing force distribution over this area from Ref. 1 test results. This value was then taken as a constant corresponding to missile

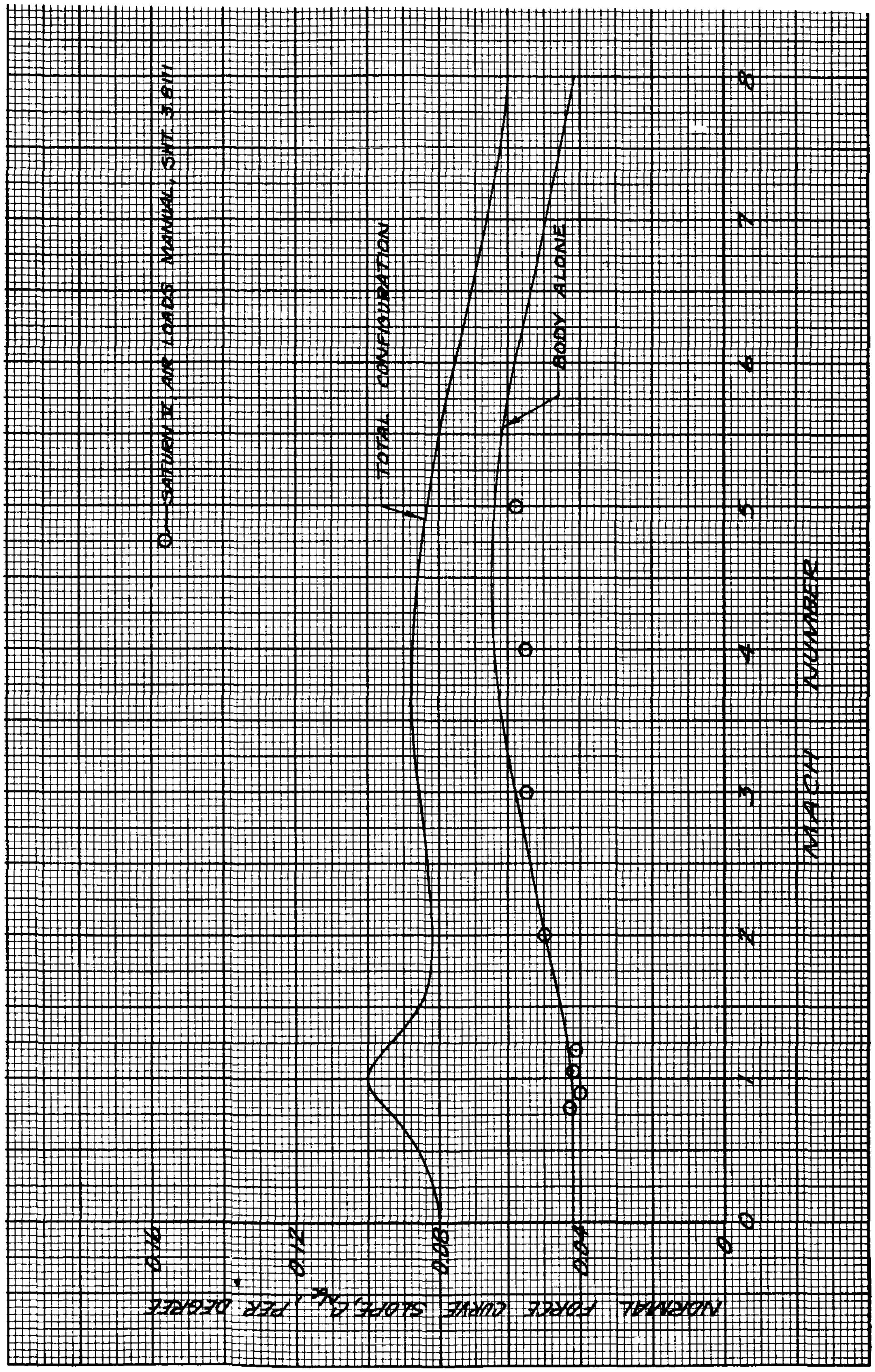

NSP 6615

Fig. 3-5 Operational Vehicle Normal Force Curve Slope for Complete Vehicle and for Body-Alone versus Mach Number

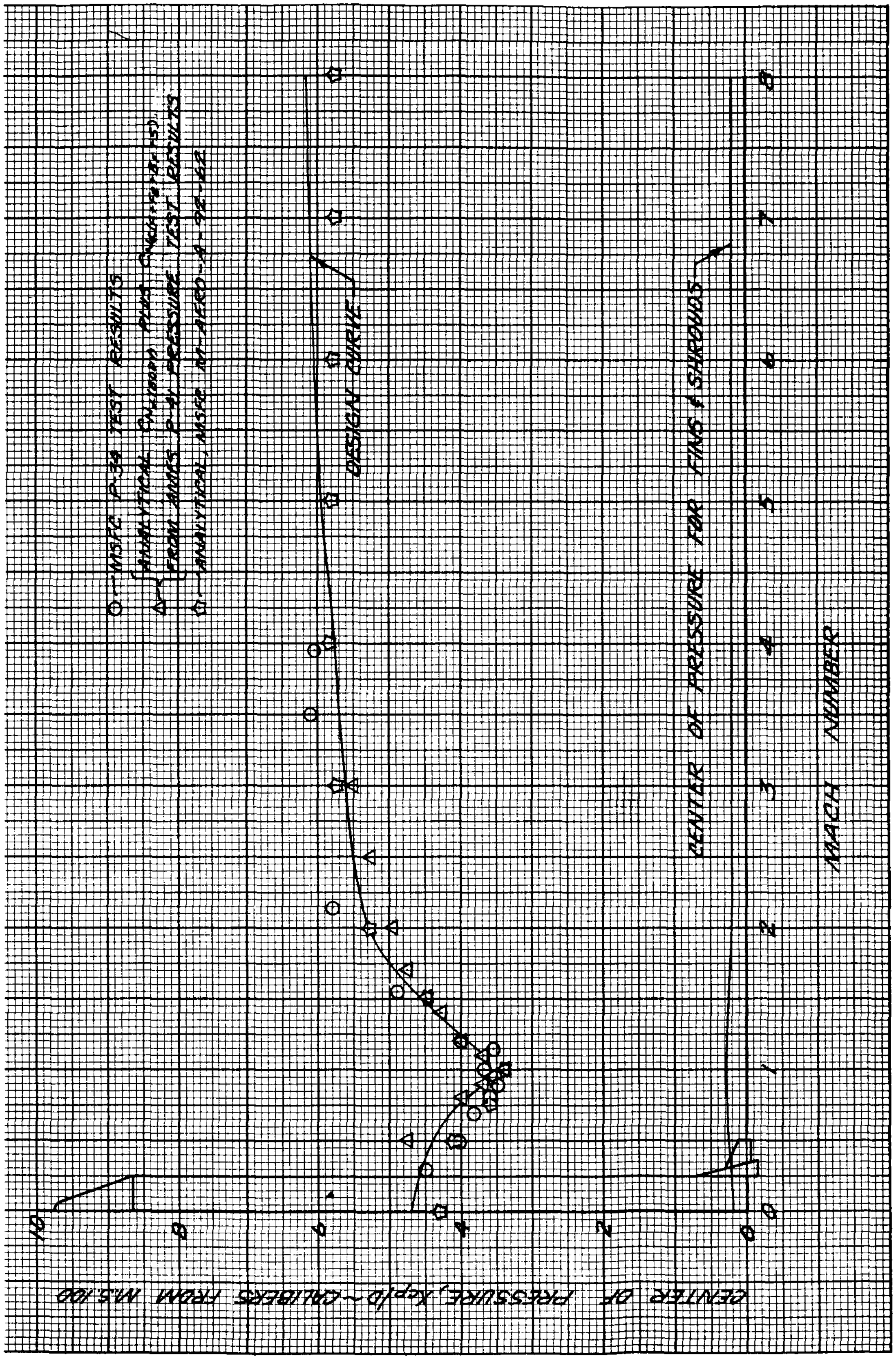

NSP 6616

Fig. 3-6 RIFT Vehicle Center-of-Pressure versus Mach Number station 237. The plot of the body-alone (no fins or shrouds) center-of-pressure is shown in Fig. 3-7. A profusion of test results from Refs. 3, 4, and 5 and test data for a 14-deg cone-cylinder, result in erratic answers in the transonic region. Analytical results are satisfactory up to Mach number of 2.0, but for Mach numbers > 2.0, reliance was placed on experimental correlations of similar configurations. Reference 7 provided a value at Mach number 6.86. The average spread in these results is approximately one-half caliber. Fin and shroud normal force characteristics (Fig. 3-4), body normal force derivative (Fig. 3-3), and body center-of-pressure (Fig. 3-7) were combined to solve for the center-of-pressure of the complete configuration.

The center-of-pressure for the Saturn VN operational vehicle body-alone configuration utilized the same methods described in calculating the normal force derivatives. Center-of-pressure variation with Mach number is presented in Fig. 3-8 for the complete Saturn VN operational vehicle and for the body-alone. Comparison of the design curve with test results from a similar configuration, CM-1 in Ref. 2 is satisfactory.

The lift of the Saturn-type vehicle's tail section consists of many component parts. Basically, these parts are the lift of the fins in presence of the body and engine shrouds, lift of the shrouds in presence of the body and fins, and lift on the body area extending between the shrouds due to carryover effects from the shrouds and fins. In equation form:

$$C_{N_\alpha}\ \text{tail} = \left(C_{N_\alpha}\right)_{F+F_B} + \left(C_{N_\alpha}\right)_{B_F} + \left(C_{N_\alpha}\right)_{S+S_B} + \left(C_{N_\alpha}\right)_{S_F}$$

$$C_{N_\alpha} = \frac{dC_N}{d\alpha}$$

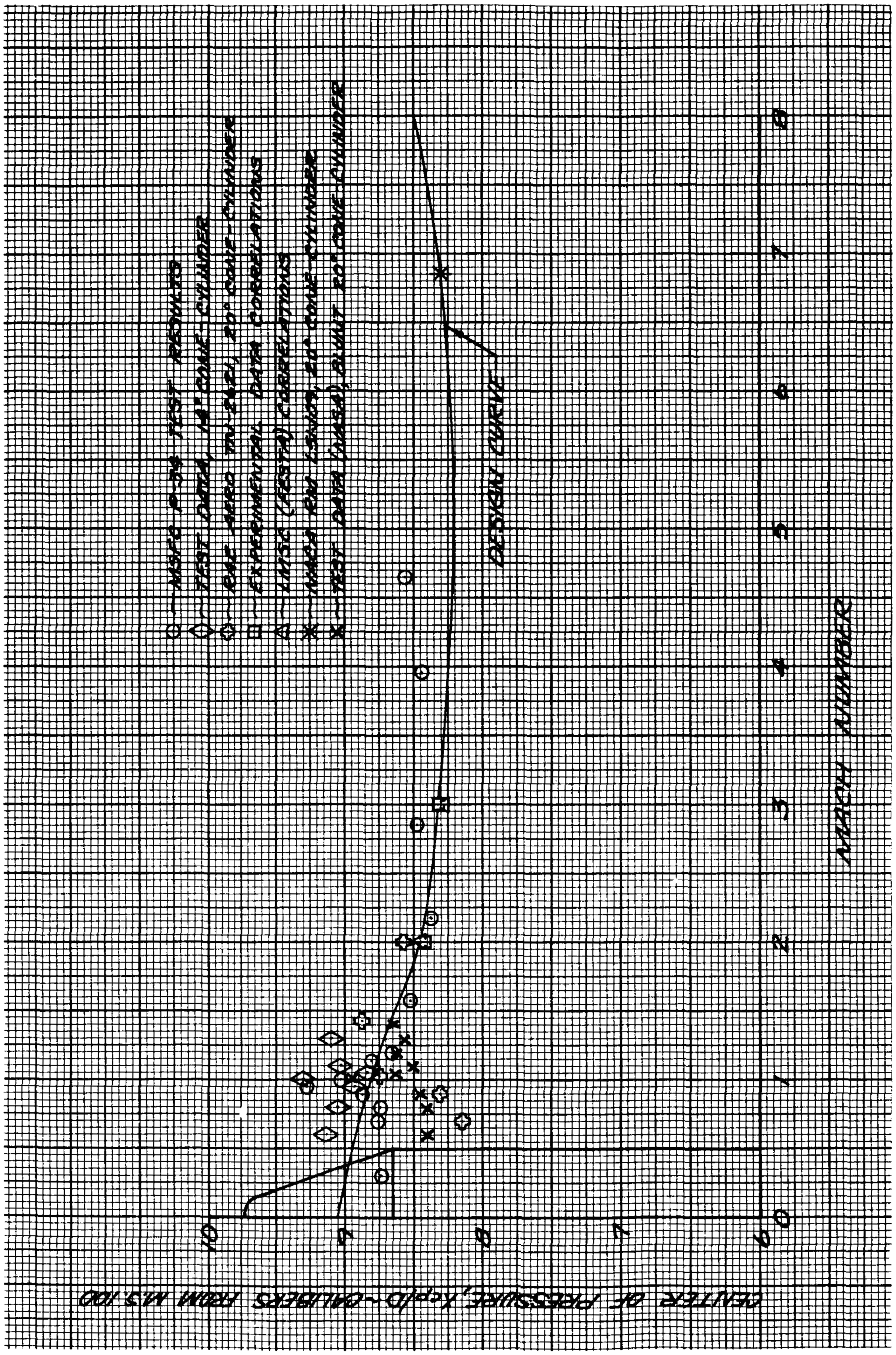

Fig. 3-7 RIFT Vehicle Body-Alone Center-of-Pressure versus Mach Number

NSP 5617

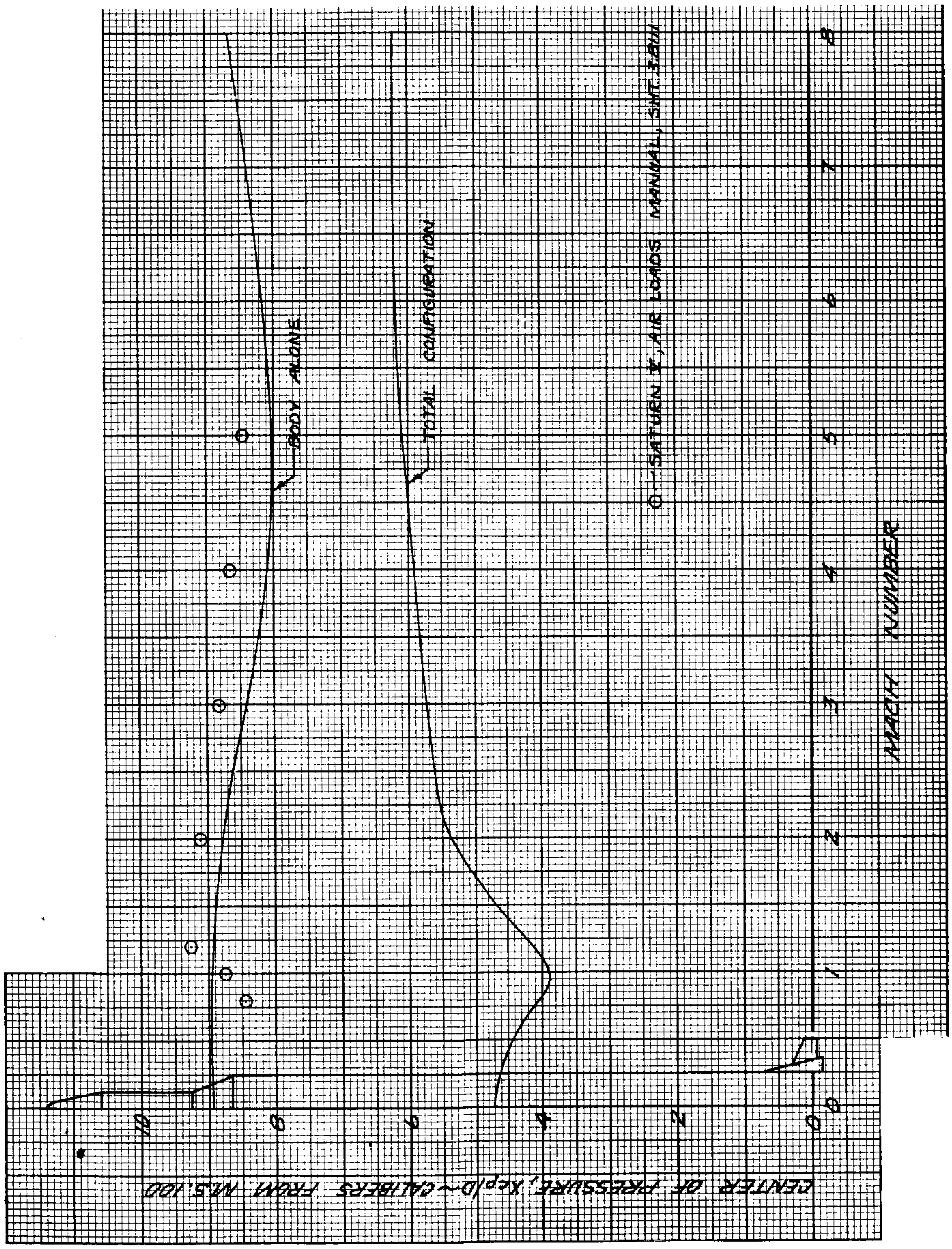

NSP 6618

Fig. 3-8 Operational Vehicle Center-of-Pressure for Complete Vehicle and for Body-Alone versus Mach Number

Subscripts refer to:

F = isolated fin

F_B = induced lift on fin due to body-shroud upwash

B_F = lift carryover onto body

S = isololated shroud (15 deg cone)

S_B = induced lift on shroud due to body upwash

S_F = induced lift on shroud due to the fin

Subsonically, the method of Ref. 10 was used to determine the normal force derivative of the isolated fin, $C_{N_{\alpha F}}$. Transonic values were faired in to reflect experimental results shown in Ref. 11. Supersonically, the linear "first-order" theory of Ackeret, pp. 73, 140, Ref. 12, corrected for effects of finite aspect ratio, was used. This expression is given as:

$$C_{N_\alpha} = \frac{4}{\beta}\left(1 - \frac{1}{2R\beta}\right), \text{ per radian}$$

where:

$\beta = \sqrt{M^2 - 1}$

R = fin aspect ratio $\sim$ (span)^2/area

Fins on the Saturn VN operational vehicle are mounted on the conical engine shrouds. For this reason, upwash effects were determined utilizing an equivalent body diameter.

The equivalent diameter was considered to extend out to the mid-point of the fin root chord and, therefore, includes an effect of upwash caused by engine shrouds. Upwash and carryover effects were determined using the methods of Nielsen and Kaatari, Ref. 13.

Total engine-shroud normal force derivatives in the presence of the body and fins were calculated using the following derived expression:

$$\left(C_{N_\alpha}\right)_{S+S_B} + \left(C_{N_\alpha}\right)_{S_F} = 2\left(C_{N_\alpha}\right)_c \left(\frac{S_c}{S_{ref}}\right) + K_{B_F} A^1 \left(C_{N_\alpha}\right)_F \left(\frac{S_F}{S_{ref}}\right)$$

where:

$\left(C_{N_\alpha}\right)_c$ = normal force derivative for a 15 deg cone

S_c = shroud (cone) base area

K_{B_F} = interference factor due to the fins, Ref. 13

S_F = exposed fin area (two panels)

S_{ref} = body reference area, 855 ft^2

A^1 = an area weighting factor

= $\left[\frac{\text{(planform area shrouds)}}{\text{planform area of body extending between shrouds}}\right]$

The factor, 2.0, is the body upwash factor and results from the induced angle-of-attack on the shrouds being twice the free-stream body angle-of-attack. The induced angle-of-attack was calculated by:

$$\alpha_i = \alpha_{body} \left[1 + \left(\frac{R}{r}\right)^2\right]$$

where:

R = body radius

r = span measured from body centerline

as given in Ref. 12. Utilizing these procedures, highly satisfactory correlations were obtained.

3.2 NON-LINEAR AERODYNAMIC CHARACTERISTICS

Normal force, center-of-pressure, and axial force characteristics as a function of angle-of-attack and covering a Mach number range from 0.8 to 3.0 are presented in this section. Non-linear characteristics are prepared for trajectory studies where gusts, missile angle-of-attack, and missile control are evaluated. Configurations for which test data are available are presented in Fig. 3-1.

Normal force coefficients, C_N , versus angle-of-attack for the RIFT vehicle are shown in Fig. 3-9, for Mach numbers from 0.8 to 3.0. Test data from Refs. 1 and 4 for the complete configuration are shown. In addition, test results for the body-alone, taken from Refs. 5 and 14, were combined with the tail-section force coefficients from the Ref. 1 test. The linear slope, $\left(C_{N_\alpha}\right)_{\alpha = 0}$, given in Section 3.1, is shown for comparison.

Note that subsonically the linearity extends up to 8-deg angle-of-attack, while for Mach numbers > 1.4, the linear range extends to only 4 deg.

Normal force coefficients for the Saturn VN operational vehicle are shown by Fig. 3-10. Test data from Refs. 1 and 4 are plotted for comparison. For low angles-of-attack, the linear characteristics, noted previously in Section 3.1, are in agreement with the test results. At angles-of-attack above the linear range, the design curve was faired through the most representative test data.

Centers-of-pressure versus angle-of-attack for the RIFT vehicle are presented in Fig. 3-11. Test data from Ref. 4 is plotted for comparison. The design center-of-pressure variation was established by using the method presented by Perkins and Allen in Ref. 6. At 90-deg angle-of-attack, the center-of-pressure is assumed to act at the planform area centroid. Agreement with the test results is satisfactory and within one-half caliber.

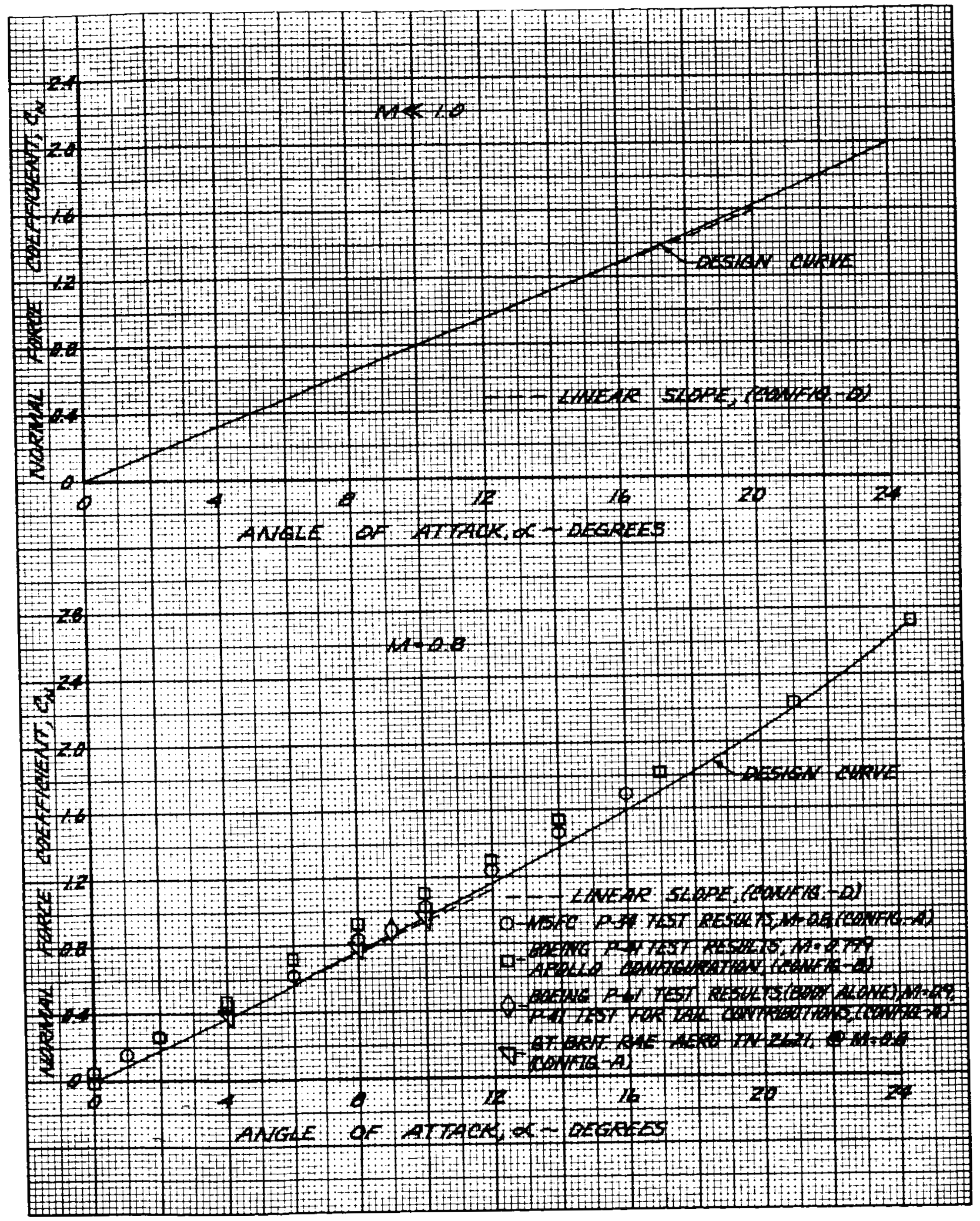

M << 1.0 and M = 0.8

Ref. Area = 855 ft^2

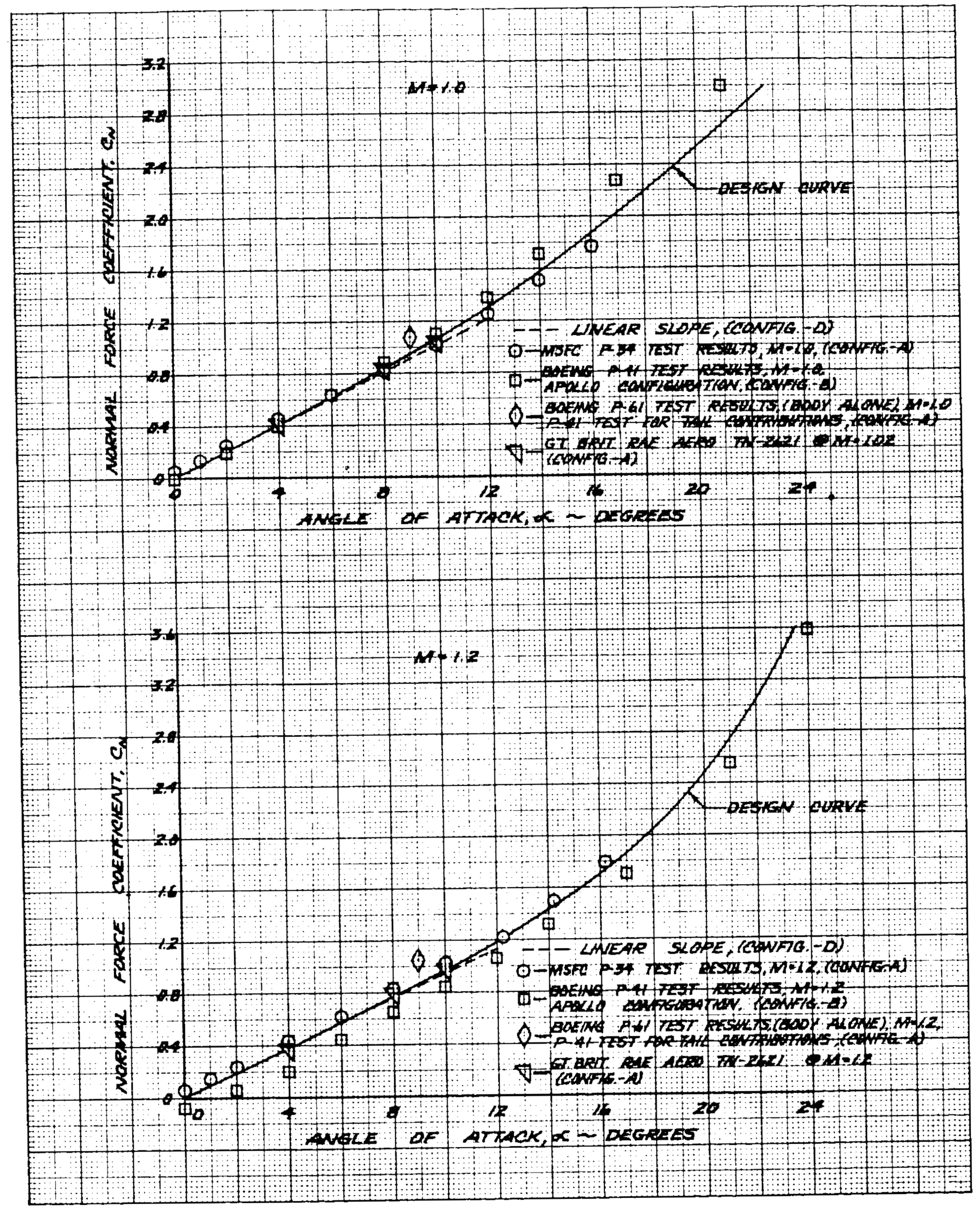

M = 1.0 and M = 1.2

Ref. Area = 855 ft^2

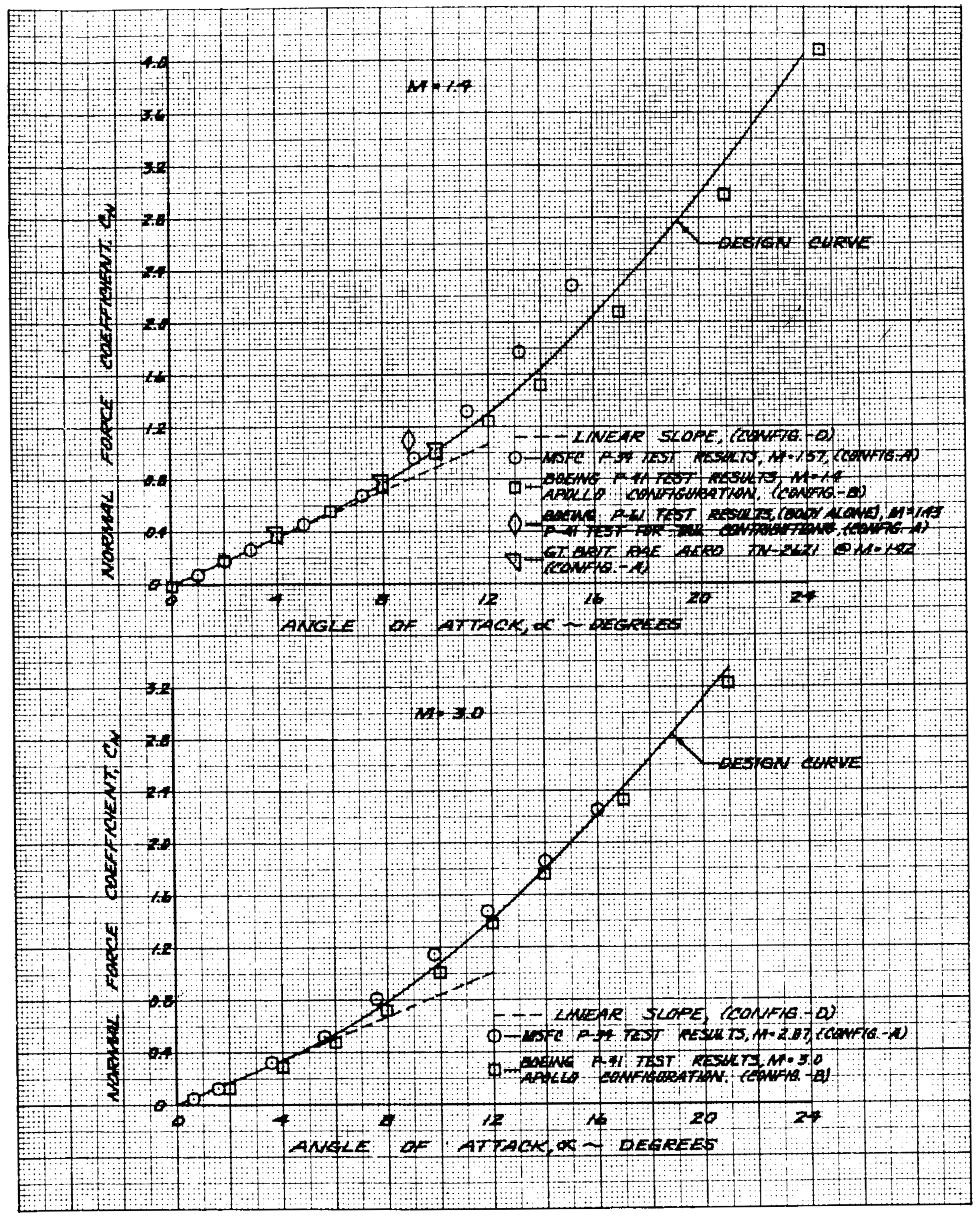

M = 1.4 and M = 3.0

Ref. Area = 855 ft^2

Fig. 3-9 RIFT Vehicle Normal Force Coefficient versus Angle-of-Attack

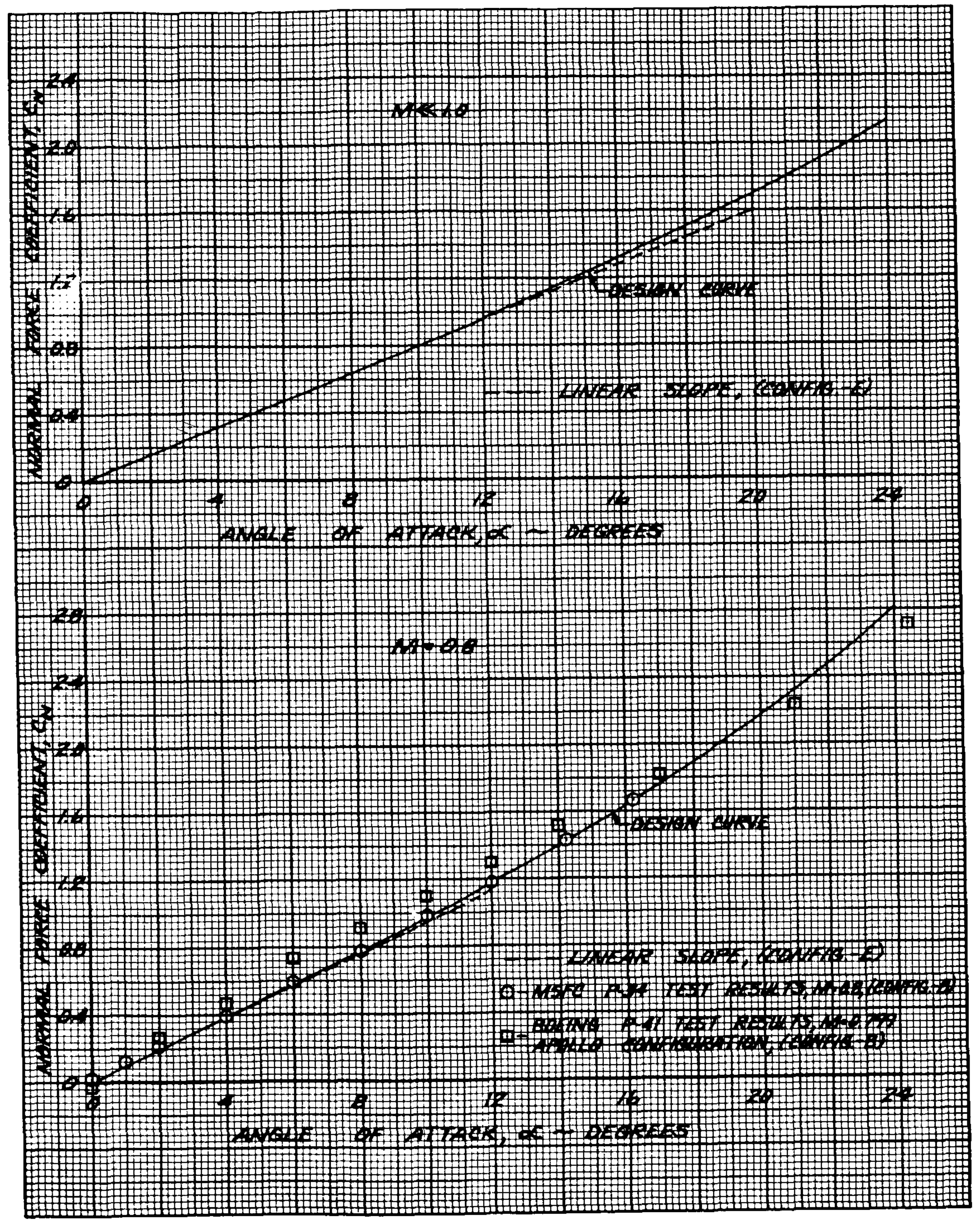

M << 1.0 and M = 0.8
Ref. Area = 855 ft^2

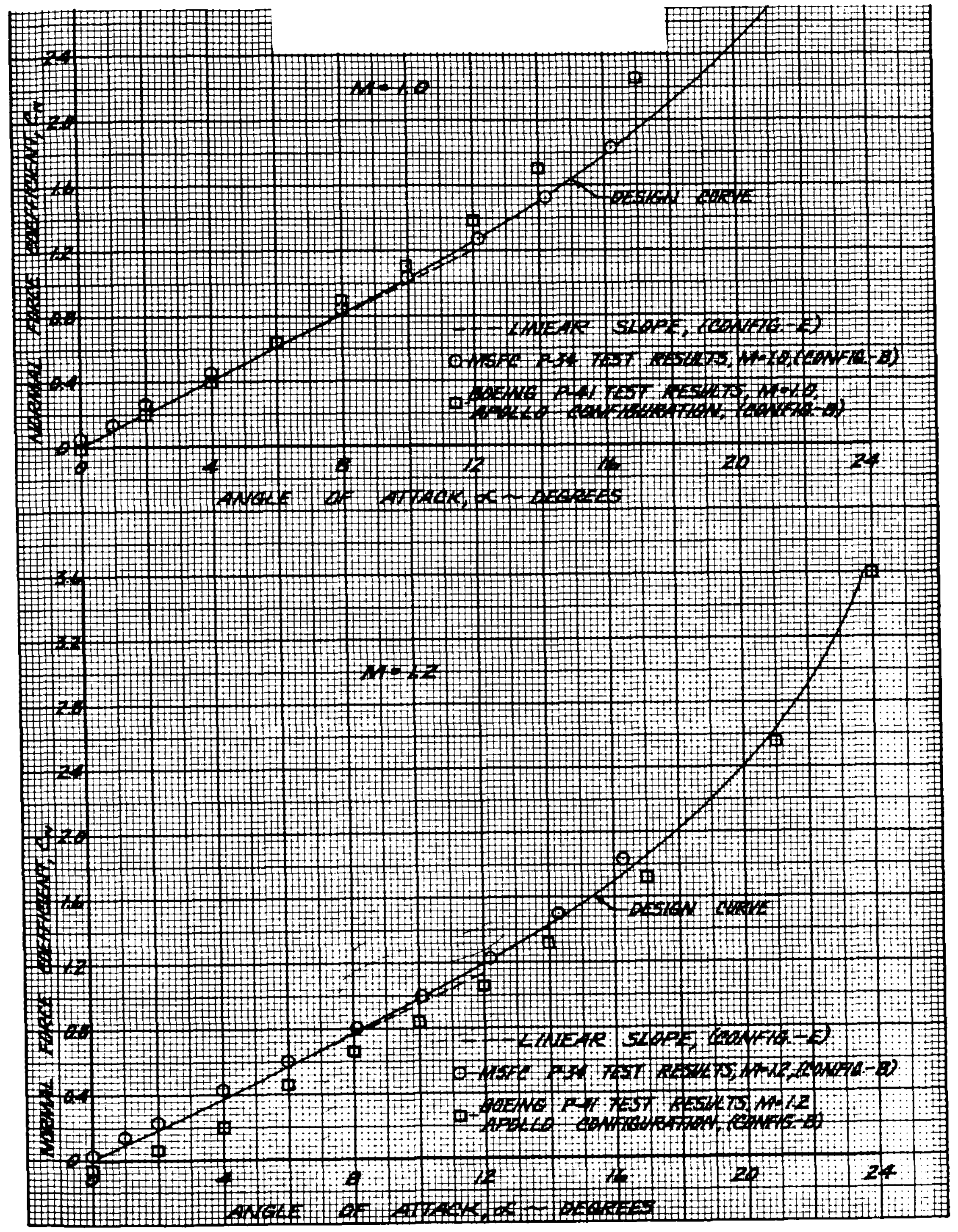

M = 1.0 and M = 1.2
Ref. Area = 855 ft^2

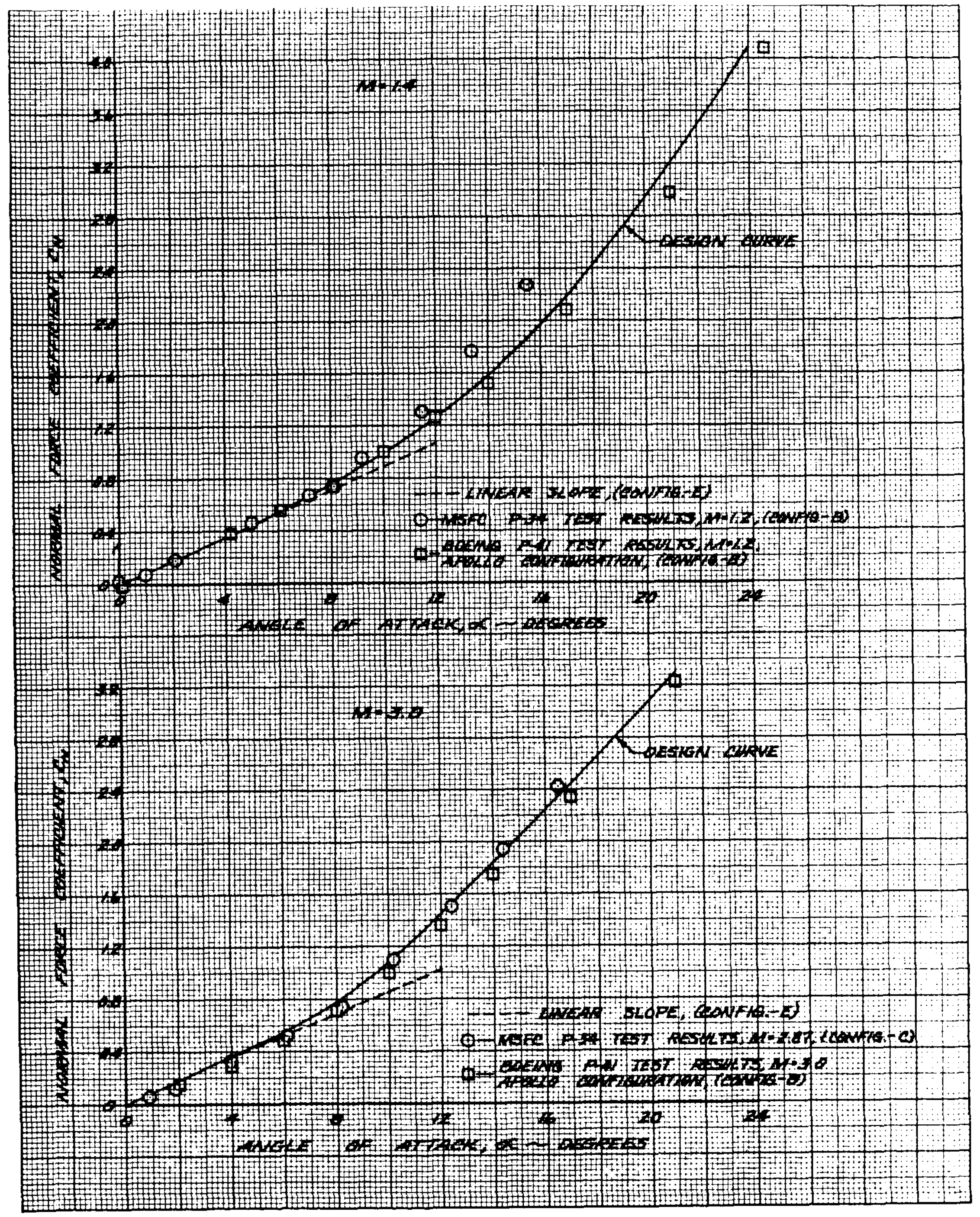

M = 1.4 and M = 3.0
Ref. Area = 855 ft^2

Fig. 3-10 Operational Vehicle Normal Force Coefficient versus Angle-of-Attack

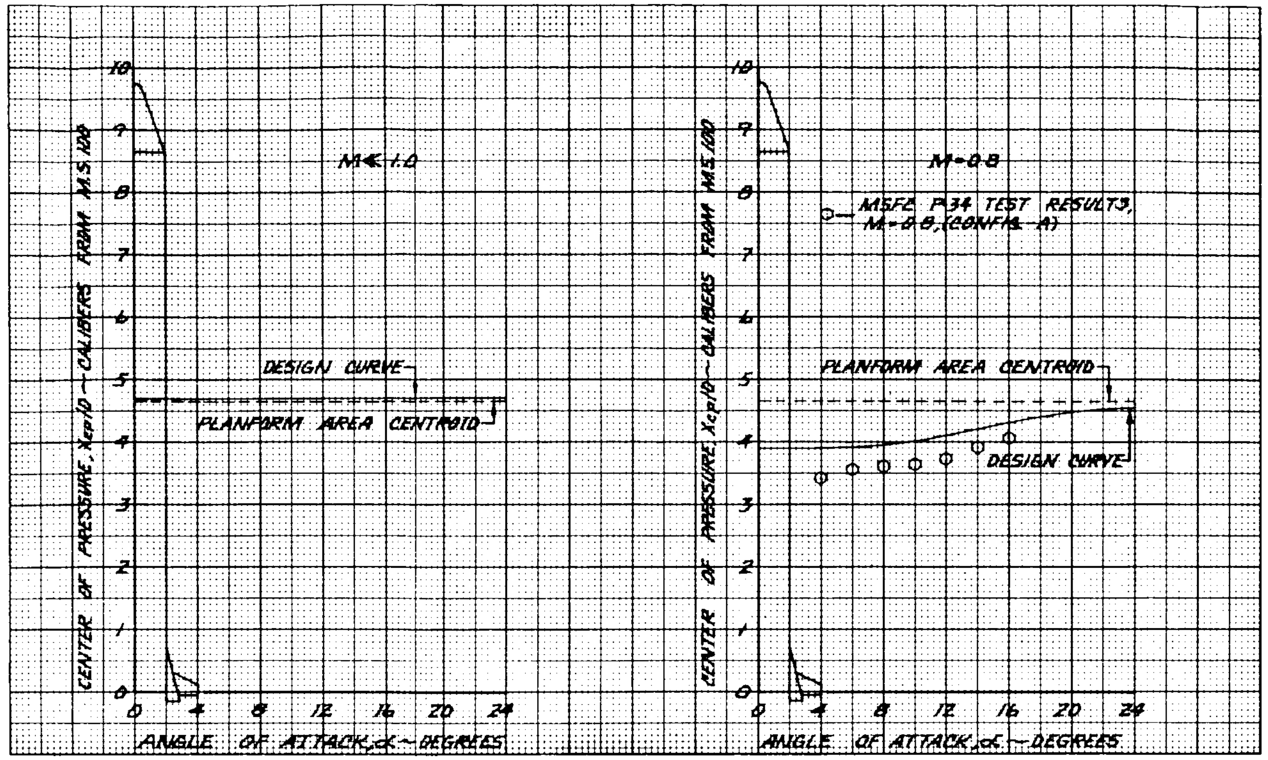

M << 1.0   M = 0.8

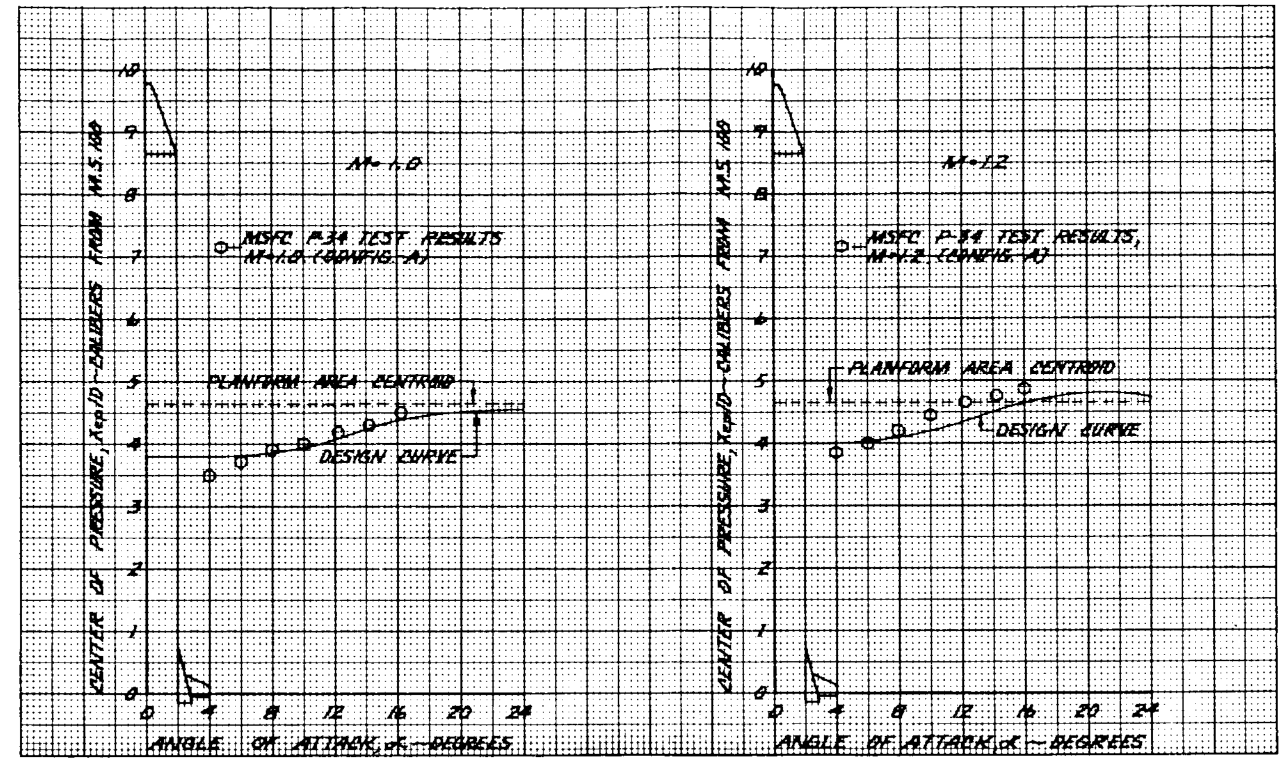

M = 1.0   M = 1.2

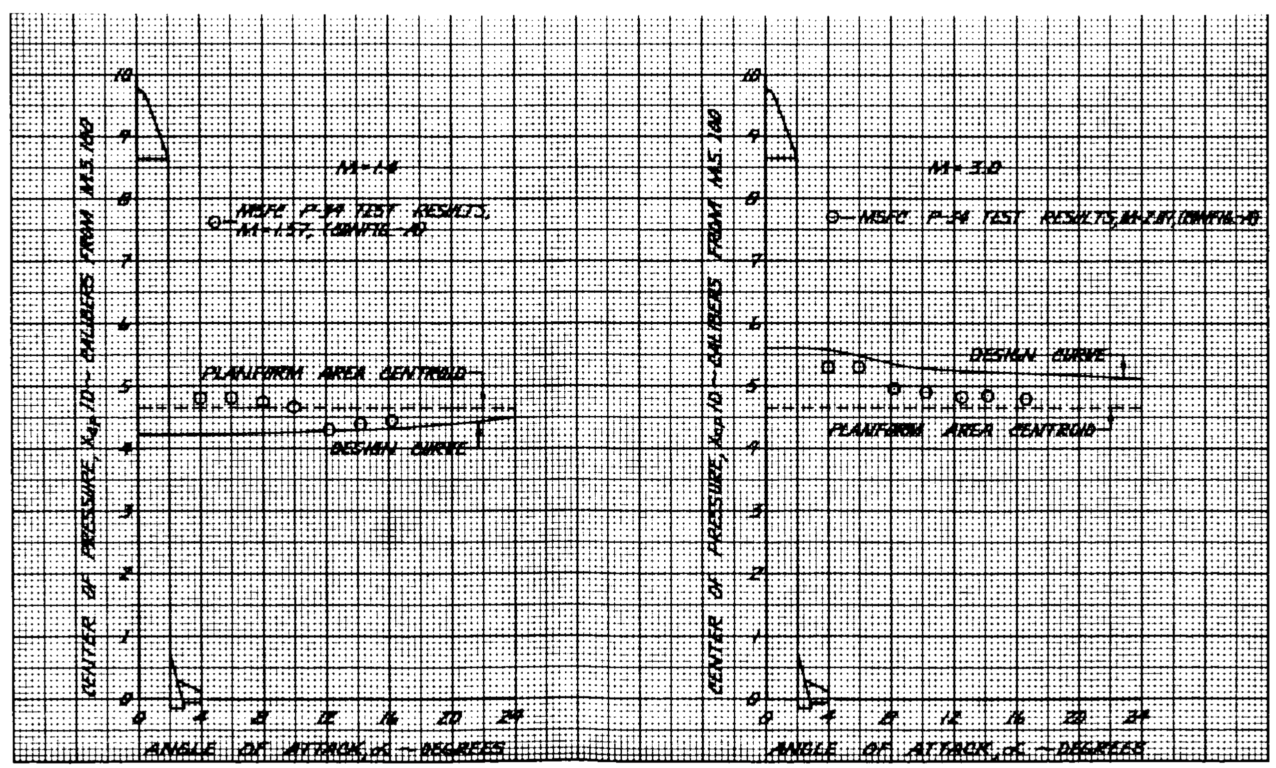

M = 1.4   M = 3.0

Fig. 3-11 RIFT Vehicle Center-of-Pressure versus Angle-of-Attack

NSP 6621

Center-of-pressure variations for the Saturn VN operational vehicle configuration are shown in Fig. 3-12, and theoretical design curves are compared with test results of Refs. 1 and 4. Test results from Ref. 1 were adjusted to account for differences in test-vehicle length as compared with the Saturn VN length; this was necessary for a reasonable basis of comparison. The accuracy here is approximately one-half caliber. Center-of-pressure versus Mach number are presented for both vehicles in Fig. 3-13 for 10- and 20-deg angles-of-attack.

Axial force coefficients, C_A , versus Mach number for angles-of-attack of 0, 10 and 16 deg are presented in Fig. 3-14 for the Saturn VN RIFT and operational vehicle configurations. The values at angle-of-attack were calculated by applying a ratio $(C_A/C_{A_{\alpha=0}})$, obtained from test results of Refs. 3 and 4 to the value of C_A at $\alpha = 0$ deg.

3.3 AERODYNAMICS IN ORBIT

Pitching moment and aerodynamic force coefficients of the S-N stage at three orbital altitudes are presented in this section. The characteristics were calculated at altitudes of 0.422, 0.528, and 1.056 x 10^6 feet at corresponding circular orbital velocities. These results were determined using the free-molecular flow theory described in Ref. 15 (and others) and were calculated to facilitate control force system design. Density values at these altitudes were taken from the 1962 U.S. Standard Atmosphere tables. All calculations utilized a molecular speed ratio (S) of 13, because the free-molecule coefficients are essentially constant above (S) of 13. A thermal accommodation coefficient of 1.0 was assumed, which means that the impacting molecules reach skin temperature before reemission.

Pitching moment versus angle-of-attack for three different center-of-gravity locations and for the three representative altitudes are presented in Fig. 3-15. Cross plots of these figures, shown in Fig. 3-16, are linear versus body station and enable the determination of the body station for zero aerodynamic moment. The total pitching moment consists of a component due to an asymmetric axial force, and a component due to normal force. The component breakdown is shown by

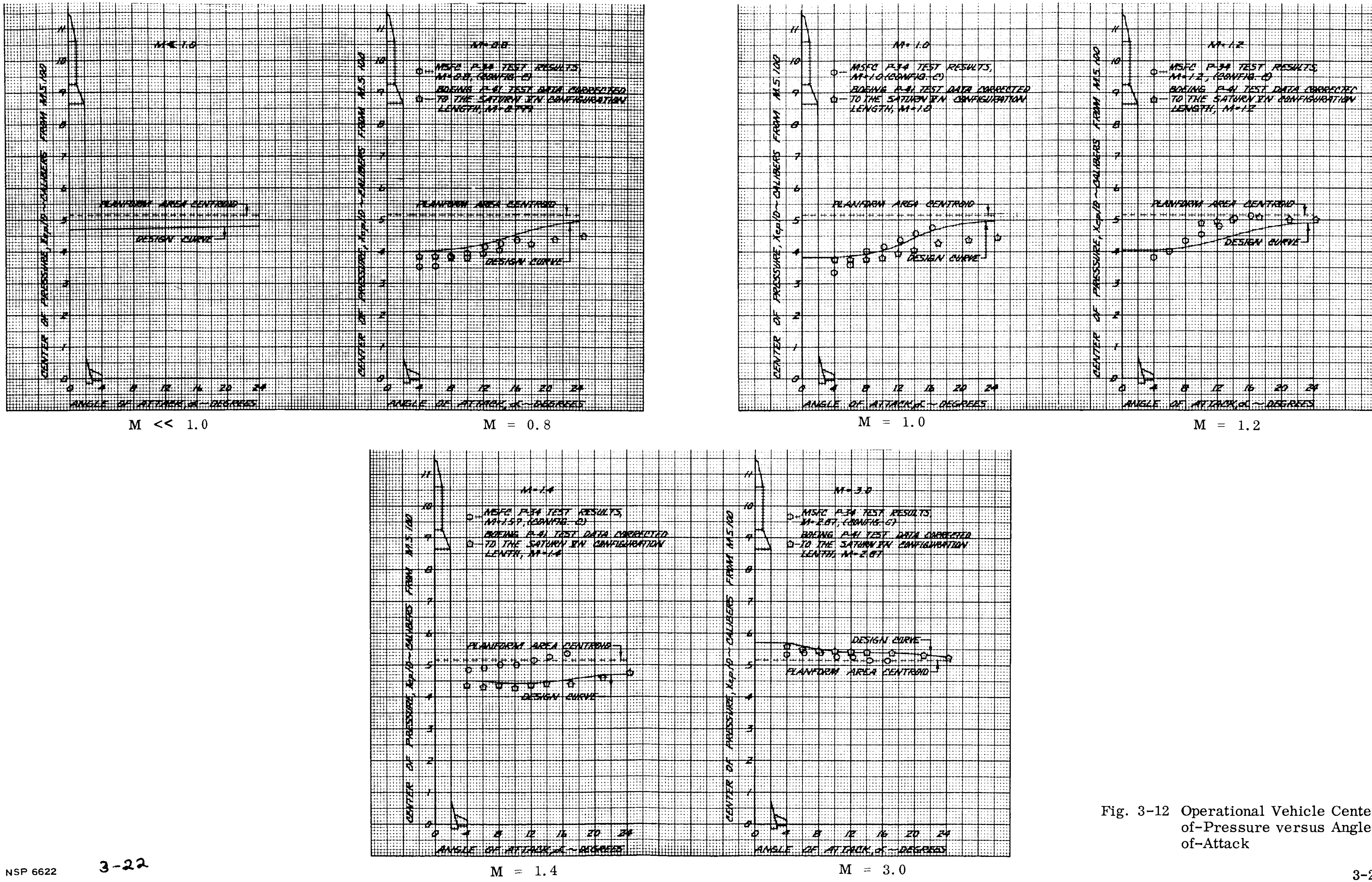

Fig. 3-12 Operational Vehicle Center-of-Pressure versus Angle-of-Attack

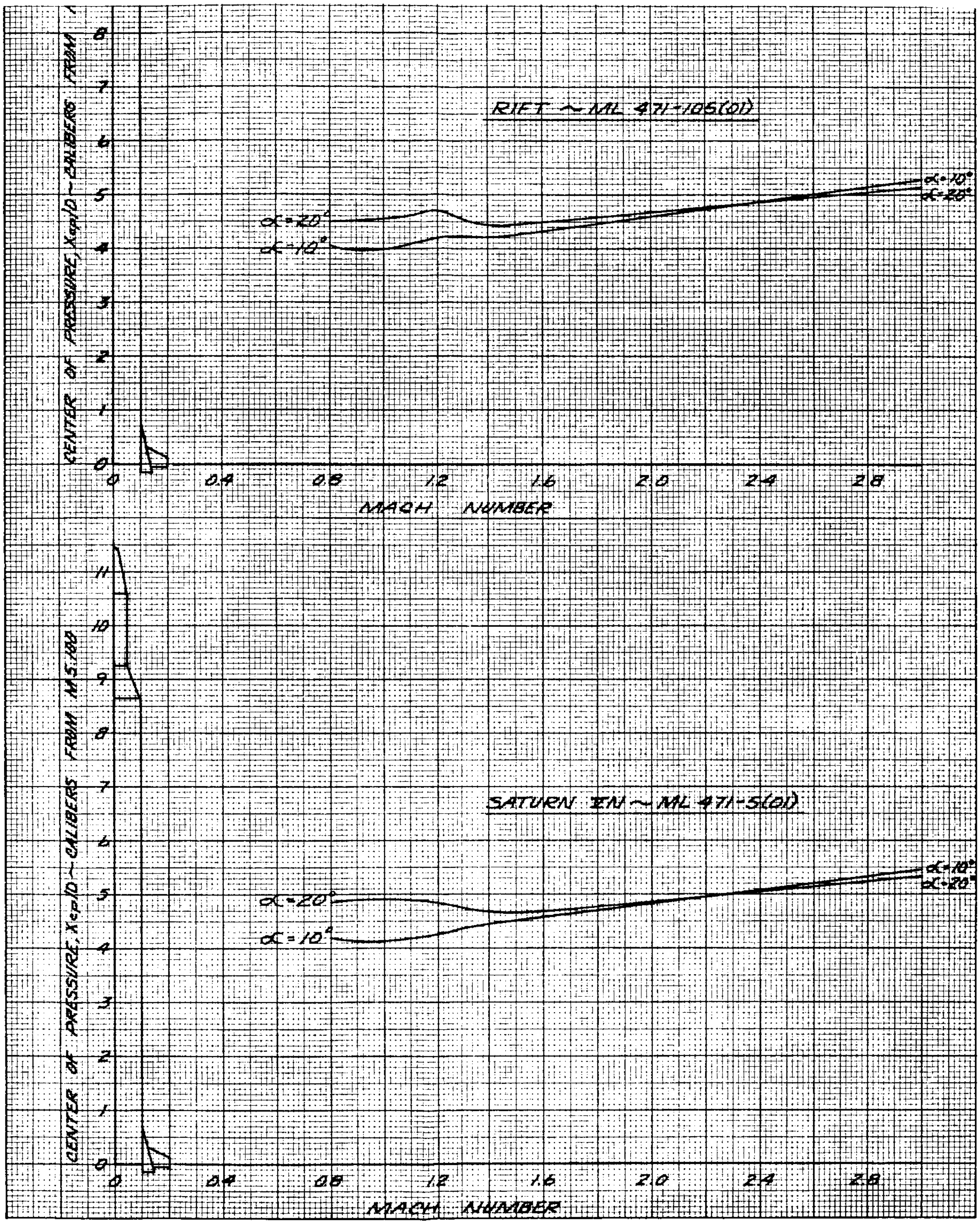

NSP 6623

Fig. 3-13 Saturn VN RIFT and Operational Vehicles Center-of-Pressure versus Mach Number for 10 and 20 Degree Angle-of-Attack

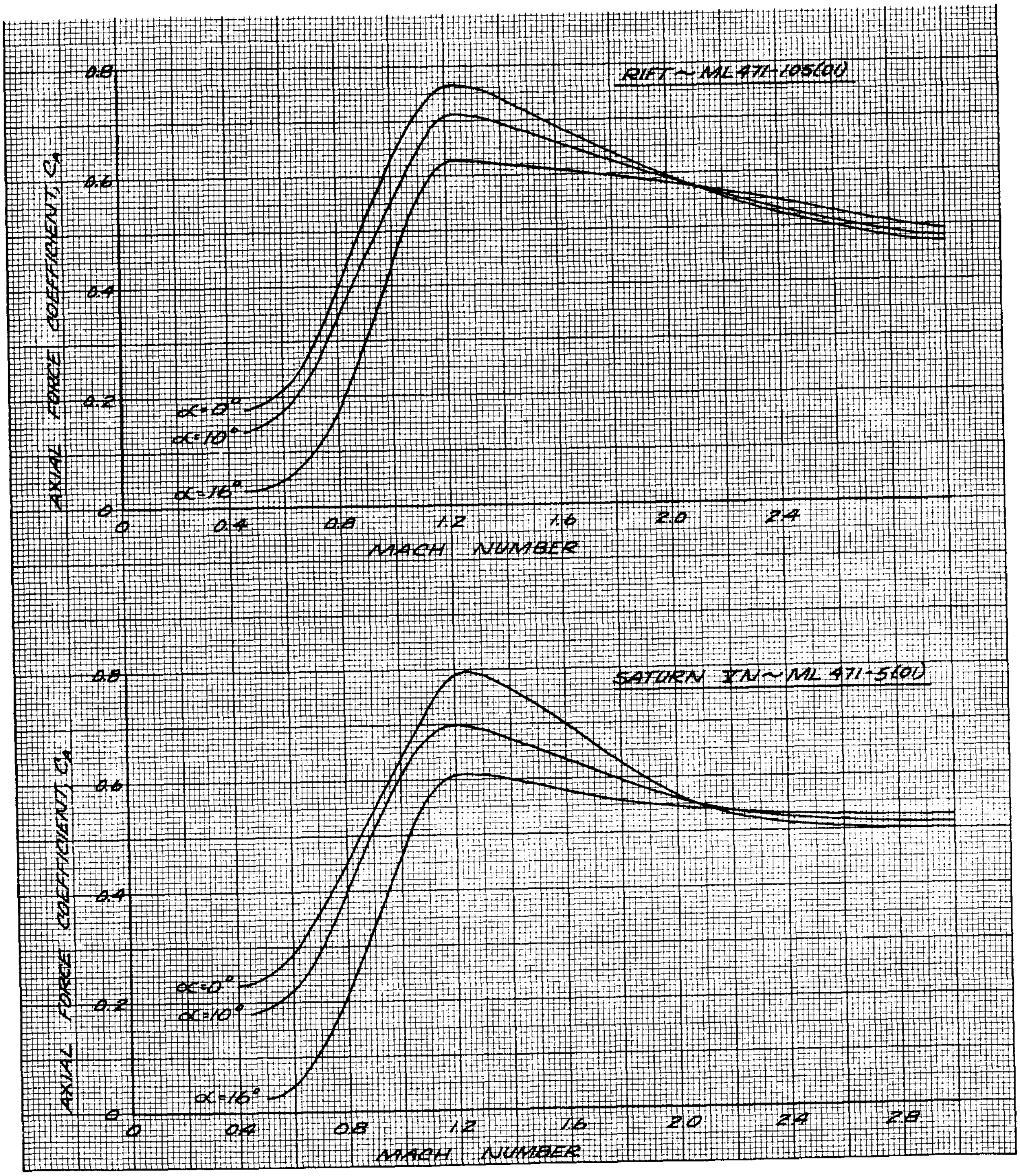

NSP 6624

Fig. 3-14 Saturn VN RIFT and Operational Vehicles Axial Force Coefficient versus Mach Number for 0, 10, and 16 Degree Angle-of-Attack

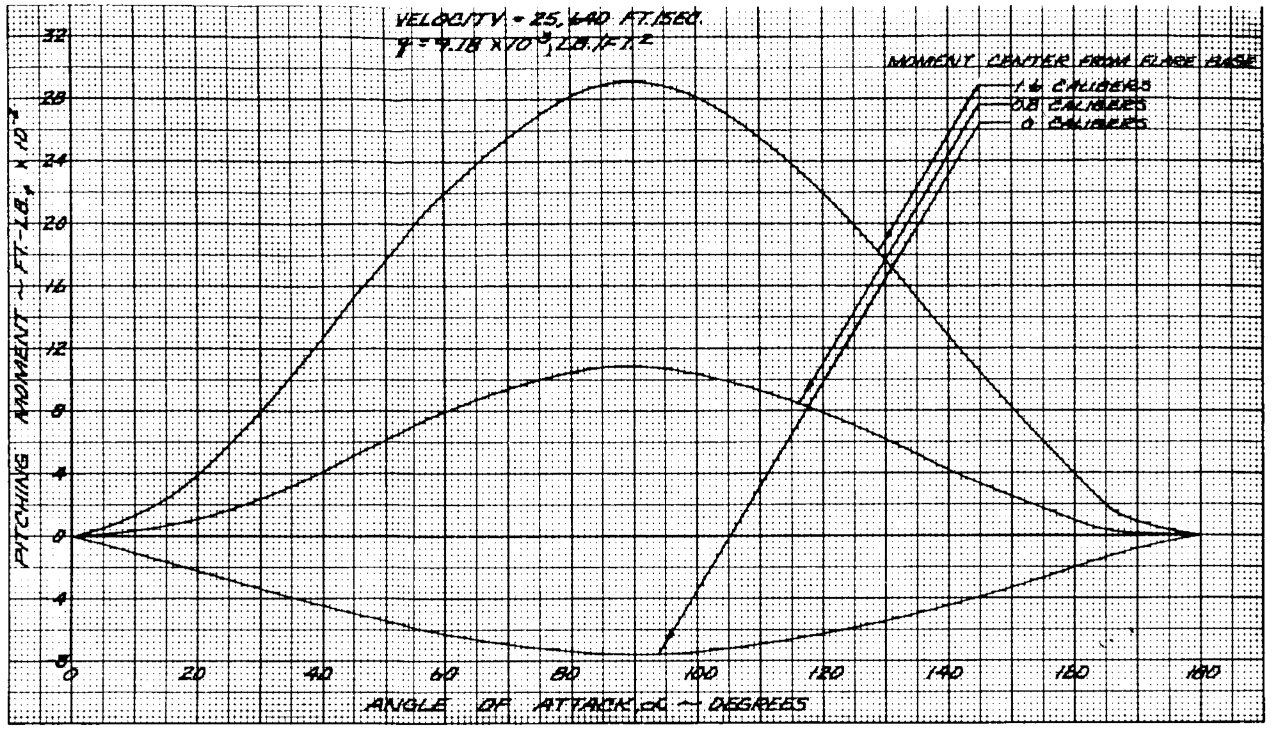

Altitude = 0.422 x 10^6 Ft

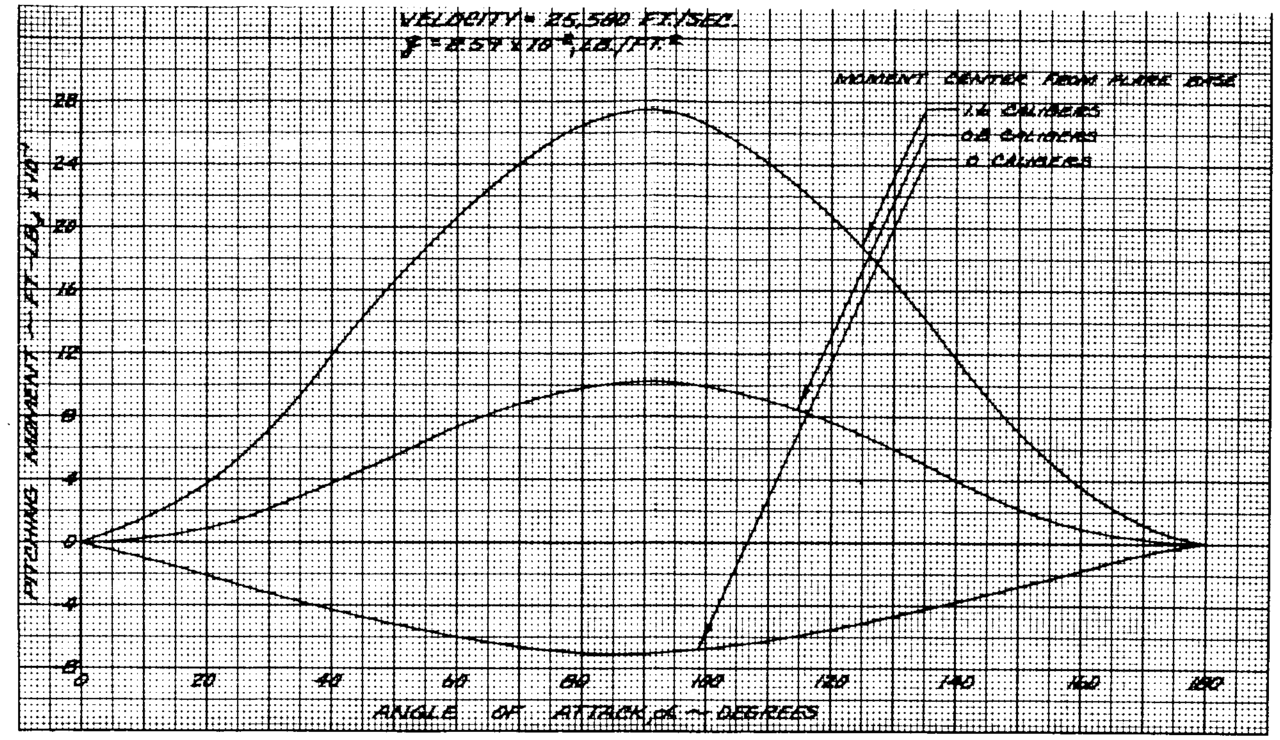

Altitude = 0.528 x 10^6 Ft

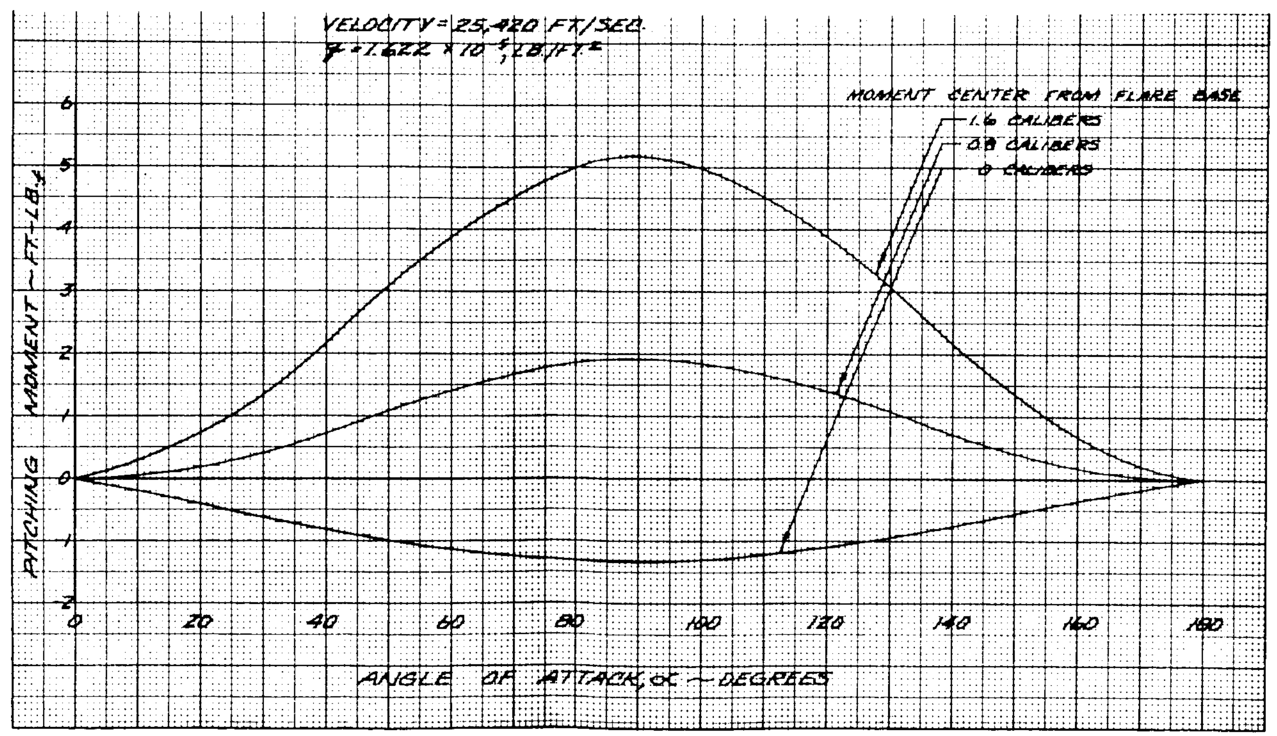

Altitude = 1.056 x 10^6 Ft

NOTES: (1) Thermal Accommodation Coefficient, $\alpha' = 1$
(2) Molecular Speed Ratio (S) = 13

Fig. 3-15 RIFT Vehicle Pitching Moments versus Angle-of-Attack at Orbital Altitudes

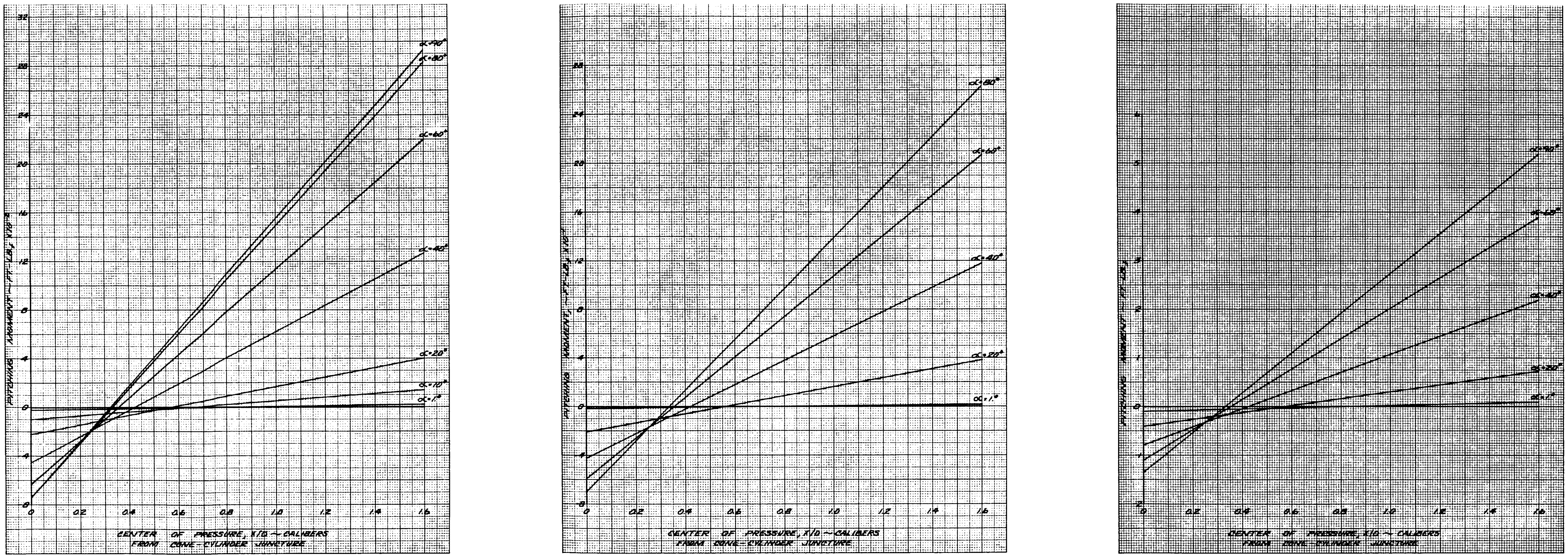

Altitude = 0.422 x 10^6 Ft

Altitude = 0.528 x 10^6 Ft

Altitude = 1.056 x 10^6 Ft

NOTES: Thermal Accommodation Coefficient, $\alpha' = 1$
Molecular Speed Ratio (S) = 13

Fig. 3-16 RIFT Vehicle Pitching Moments versus Center-of-Pressure at Orbital Altitudes

NSP 6626

Fig. 3-17 in the form of moment coefficients, C_m , versus angle-of-attack. The point of application of the normal force component and the body station for zero aerodynamic moment versus angle-of-attack are presented by Fig. 3-18. Free-molecular normal force coefficient is indicated by Fig. 3-19. The axial force coefficient versus angle-of-attack is presented in Fig. 3-20.

3.4 EFFECT OF PAYLOAD LENGTH ON CENTER-OF-PRESSURE

A brief study for determining the effect of changing the payload-envelope length on the center-of-pressure location was conducted. Results determined previously in this report for the Saturn VN RIFT and operation vehicle configurations were utilized in combination with test results from Ref. 2 and correlated test results to give the variation shown in Fig. 3-21. The effect of changing the envelope length from 0.7 caliber (RIFT) to 3.0 calibers is observed to move the total vehicle center-of-pressure forward by only 0.5 caliber at Mach number 1.5. The change at Mach number 1.0 is essentially zero.

3.5 AERODYNAMICS DURING S-N STAGE SEPARATION

Estimates of the normal and axial force coefficients and center-of-pressure have been made for the Saturn VN RIFT and operational vehicles just prior to and directly after S-N stage separation. The results presented here are based upon hypersonic modified Newtonian theory and are intended for use in determining the effects on separation performance should separation occur in a region where dynamic pressure is significant.

Normal force coefficients versus angle-of-attack are presented in Figs. 3-22 and 3-23. These figures also show the component breakdowns for the S-N stage, the trailing booster at a separation distance not in excess of one caliber, and the complete configuration just prior to S-N stage separation. Based upon an assumption of no appreciable change in normal force for separation distances less than 1.0 caliber, the trailing booster has only normal force due to body cross-flow; and contributions due to fins and shrouds for the Saturn VN (RIFT) vehicle. Centers-of-pressure versus angle-of-attack are shown by Figs. 3-24 and 3-25.

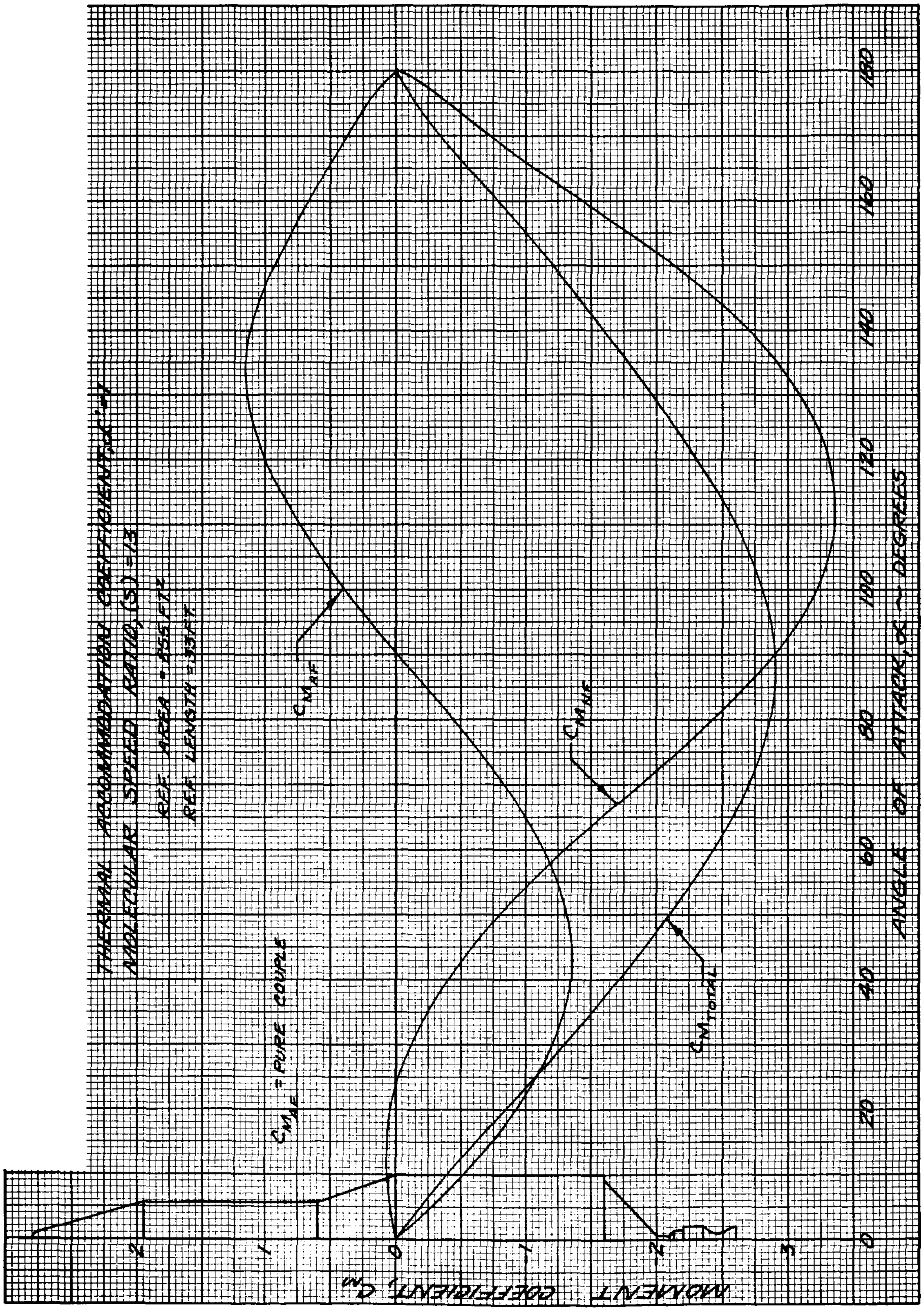

NSP 6627

Fig. 3-17 RIFT Vehicle Moment Coefficient versus Angle-of-Attack at Orbital Altitudes

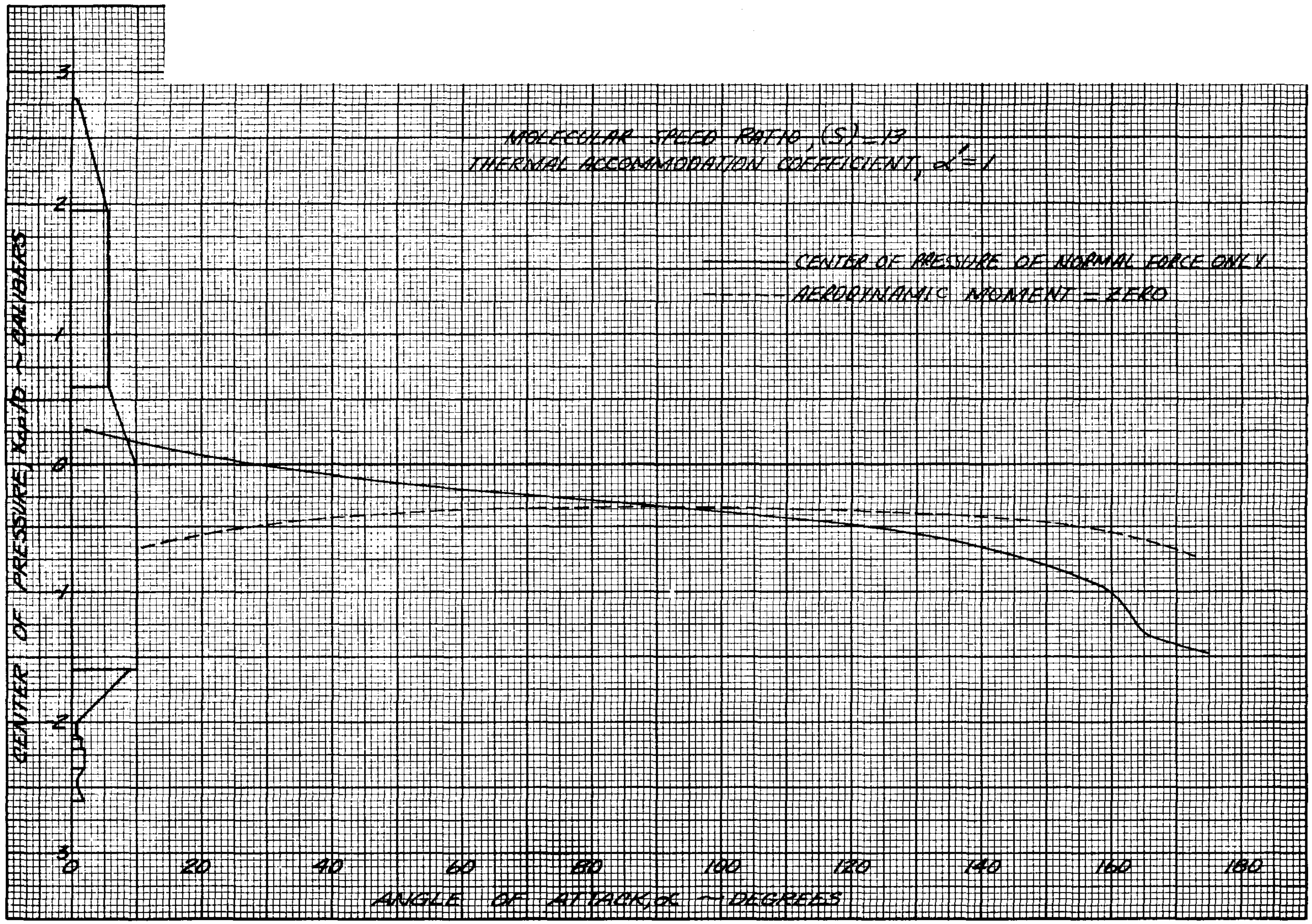

NSP 6628

Fig. 3-18 RIFT Vehicle Center-of-Pressure versus Angle-of-Attack at Orbital Altitudes

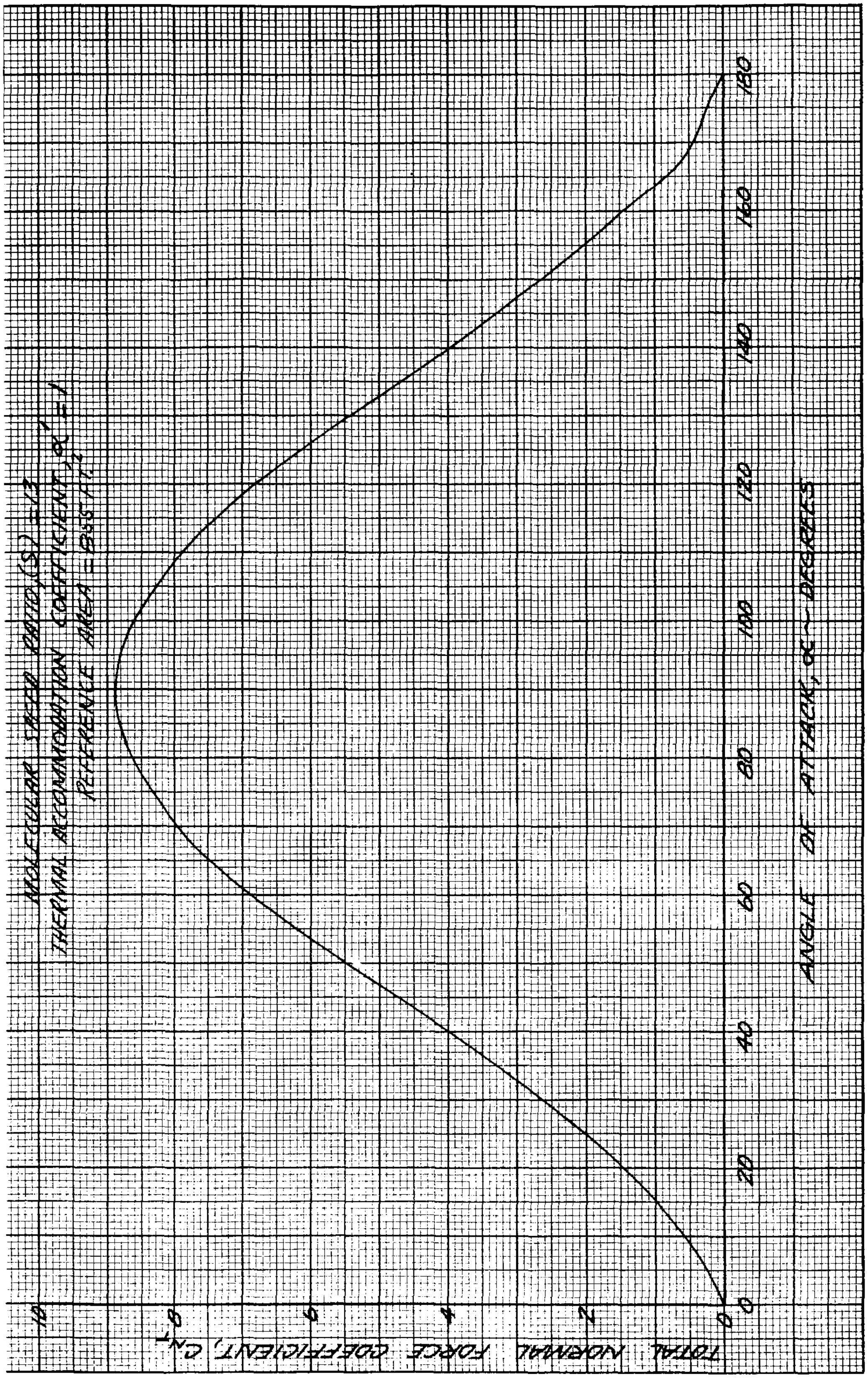

NSP 6629

Fig. 3-19 RIFT Vehicle Normal Force Coefficient versus Angle-of-Attack at Orbital Altitudes

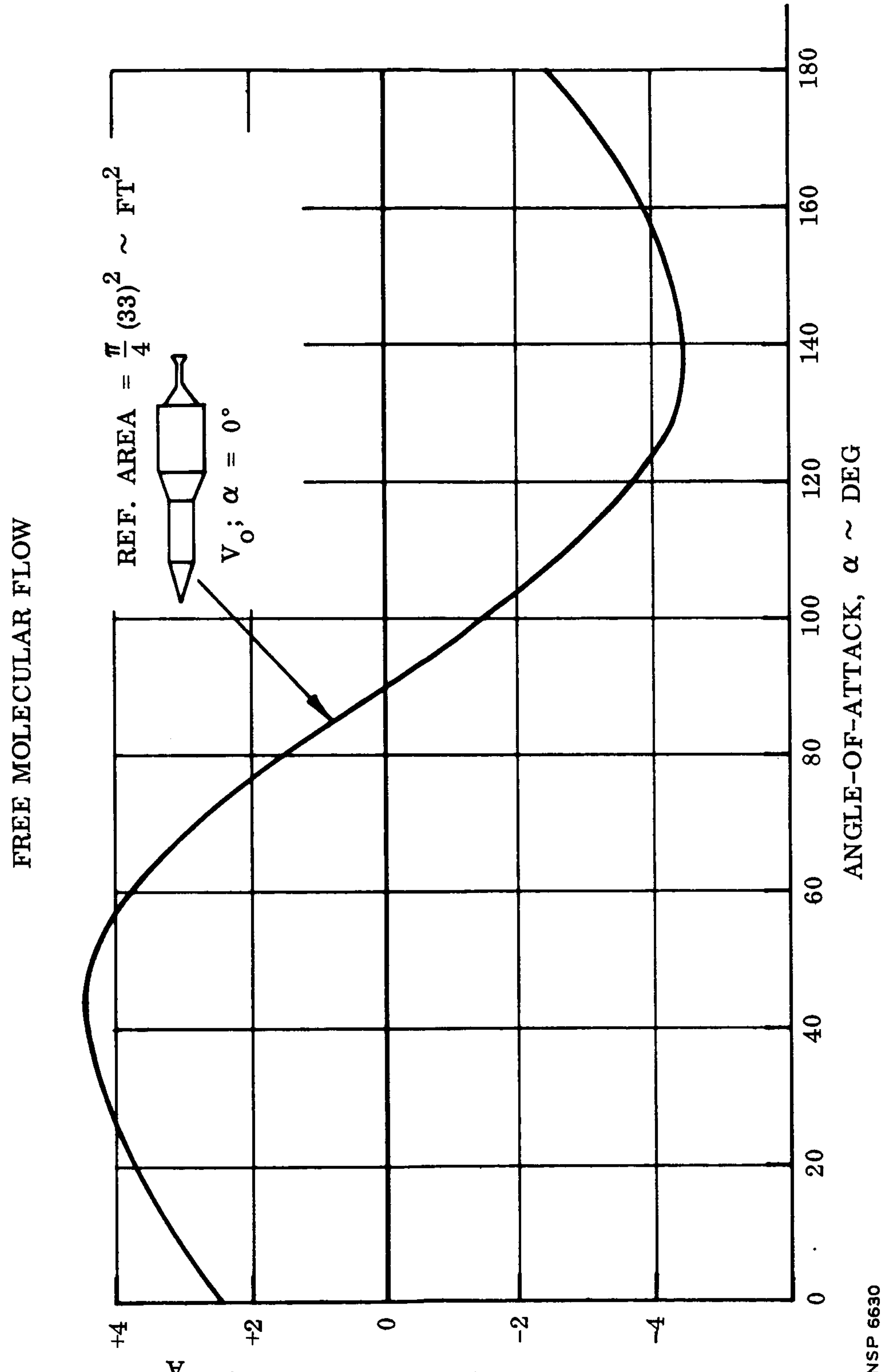

Fig. 3-20 S-N Stage (RIFT) Axial Force Coefficients in Orbiting Flight

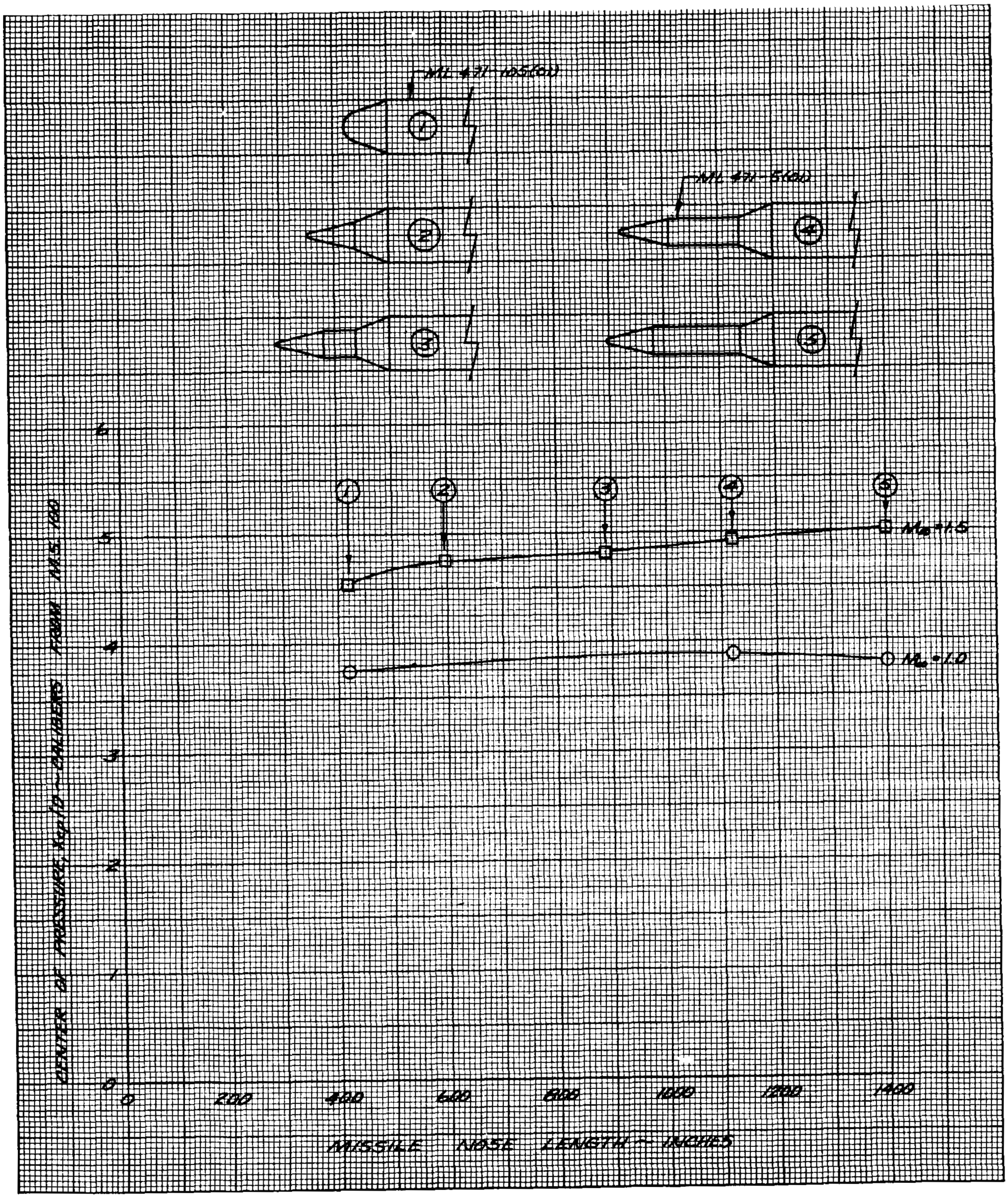

NSP 6631

Fig. 3-21 Effect of Payload-Envelope Length on Center-of-Pressure

HYPERSONIC CONTINUUM FLOW

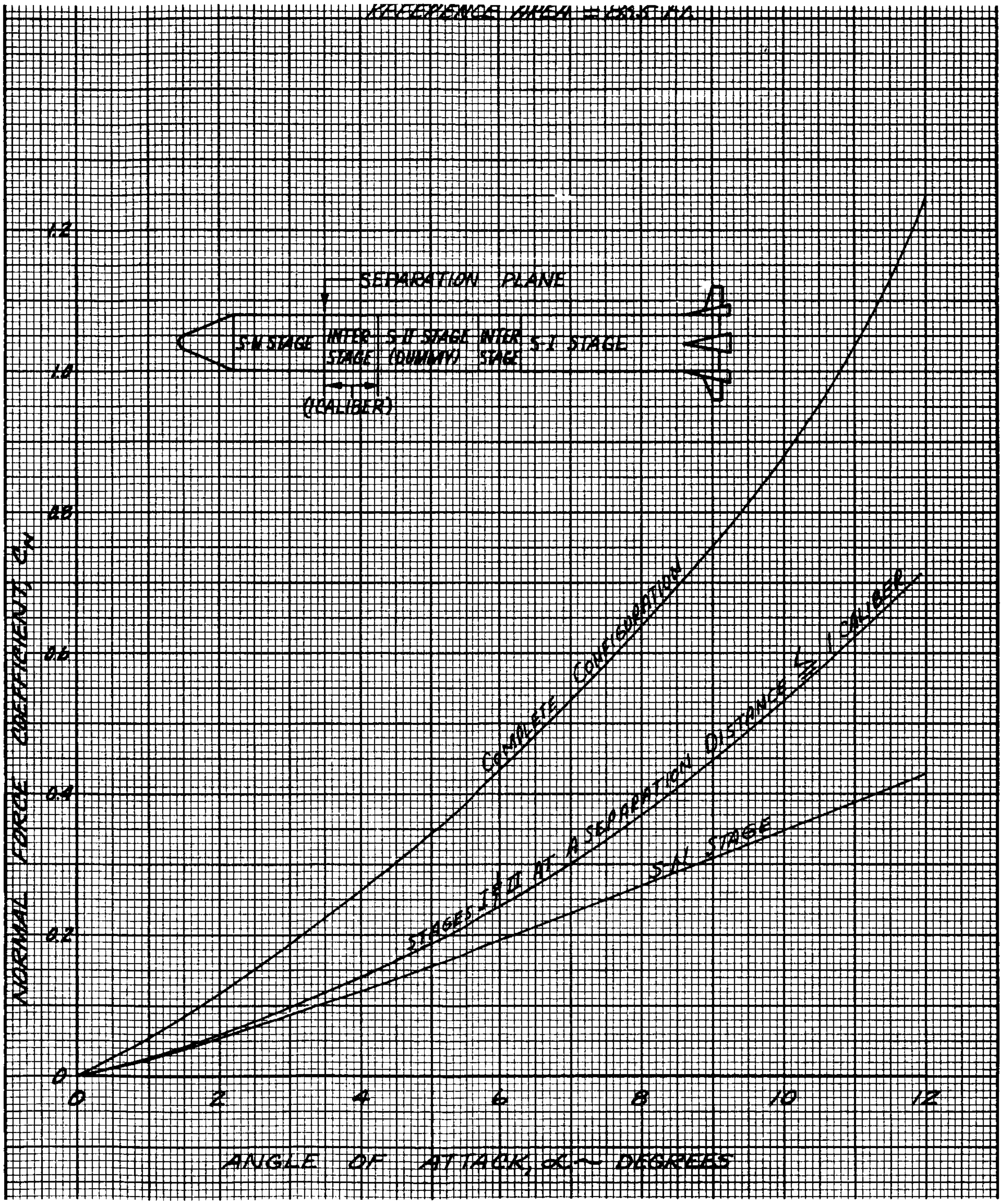

NSP 6632

Fig. 3-22 RIFT Vehicle **Normal** Force Coefficients at Separation versus Angle-of-Attack

HYPERSONIC CONTINUUM FLOW

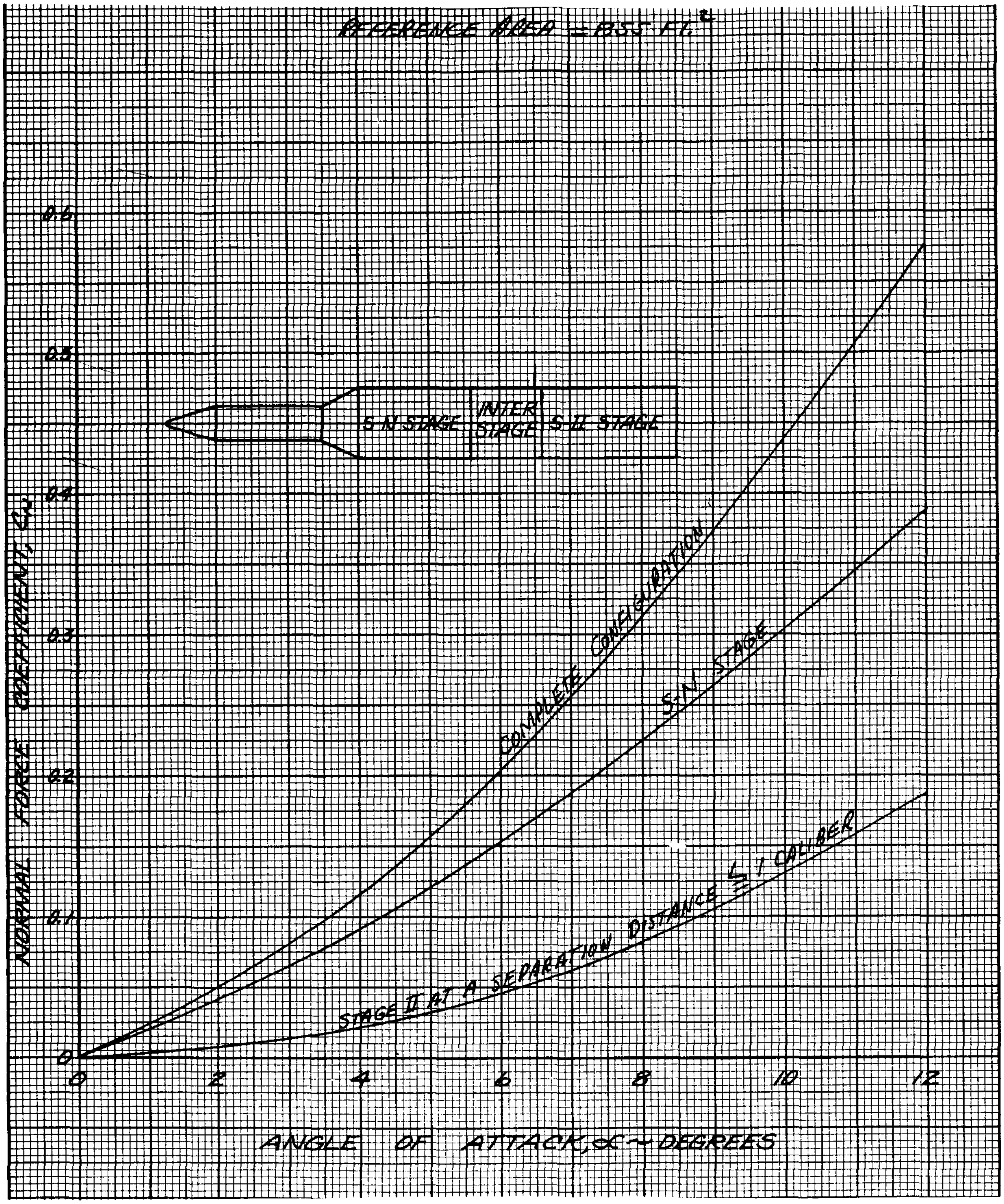

NSP 6633

Fig. 3-23 Operational Vehicle Normal Force Coefficients at Separation Versus Angle-of-Attack

HYPERSONIC CONTINUUM FLOW

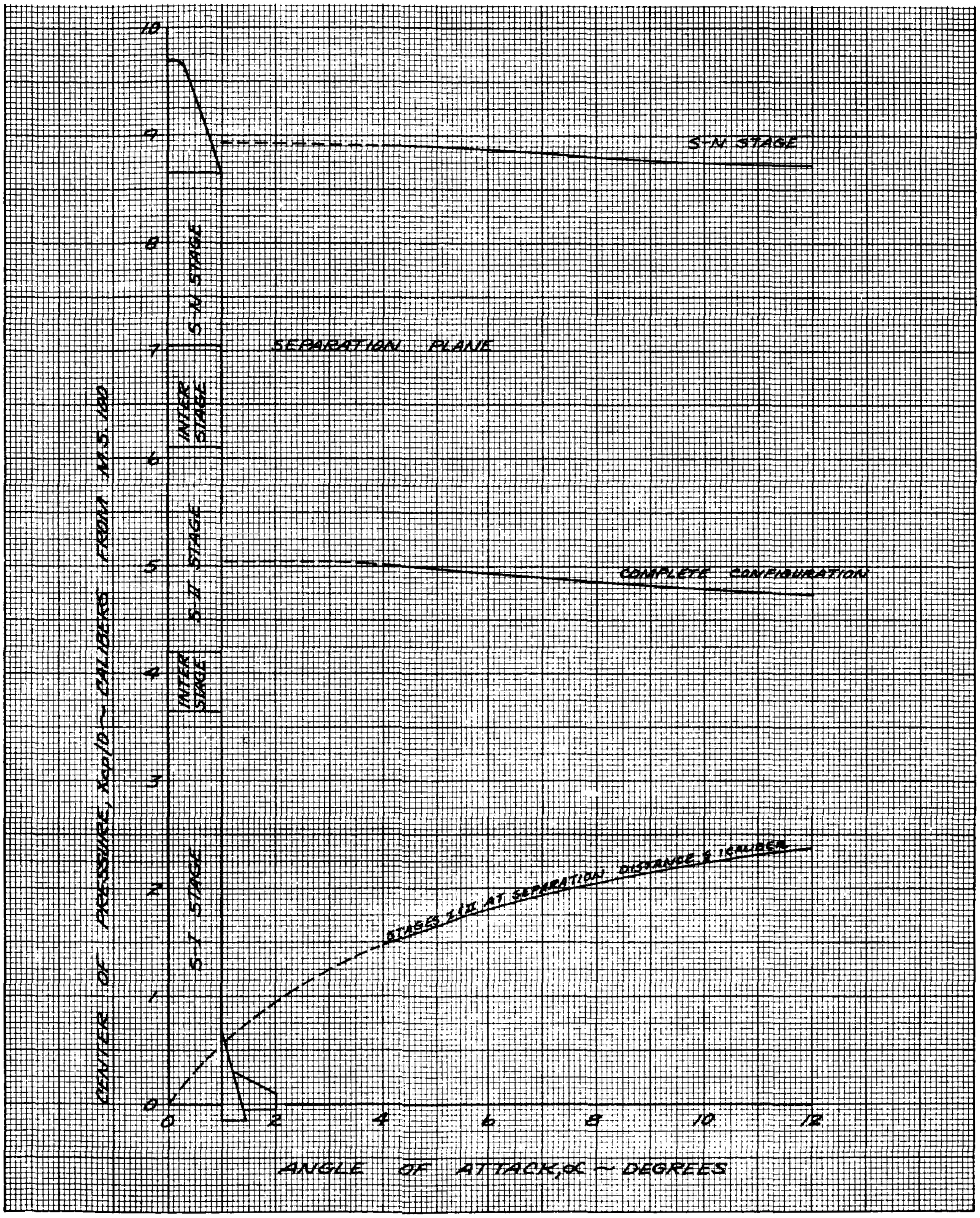

NSP 6634

Fig. 3-24 RIFT Vehicle Center-of-Pressure at Separation versus Angle-of-Attack

HYPERSONIC CONTINUUM FLOW

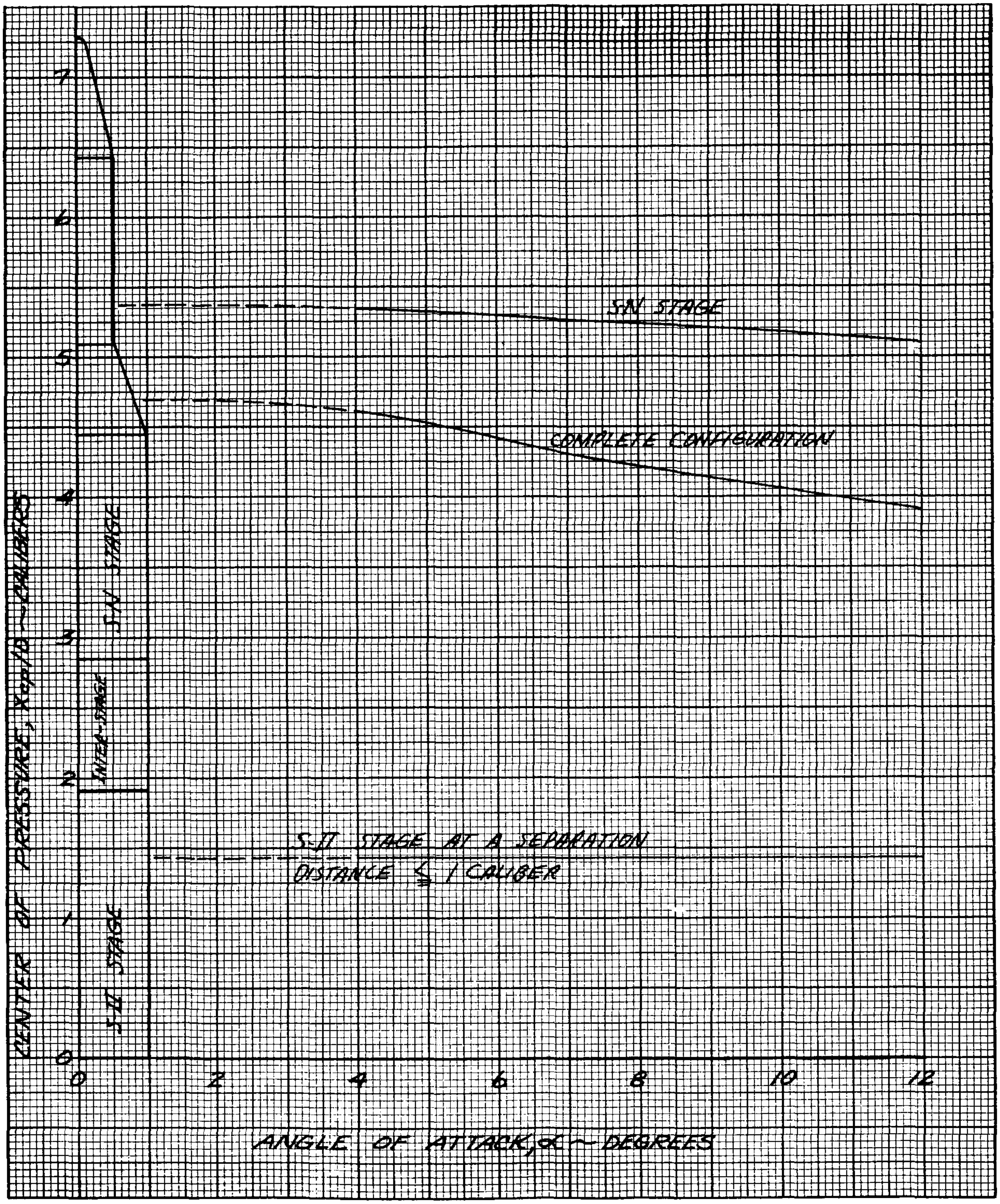

NSP 6635

Fig. 3-25 Operational Vehicle Center-of-Pressure at Separation versus Angle-of-Attack

Axial force coefficients are presented by Figs. 3-26 and 3-27. The axial force for the trailing booster increases sharply with angle-of-attack following separation due to flow impingement on the flat face of the booster. Complete separation of the S-N stage nozzles from the interstage occurs at approximately 1.0 caliber.

3.6 LIFTOFF AERODYNAMICS

Aerodynamic characteristics of the Saturn VN RIFT and operational vehicles for studying liftoff motions are noted in Fig. 3-28. The normal force coefficient and center-of-pressure are presented for Mach numbers $<< 1.0$ and for angles-of-attack from 0 to 90 deg.

Variation of normal force versus angle-of-attack was determined as follows:

(1) From $\alpha = 0$ to 15 deg, normal force curve slopes from Figs. 3-2 and 3-5, Section 3.1 of this report, were utilized.
(2) At $\alpha = 90$ deg, integrations of the launch pad cross-force coefficient distributions were made.
(3) For $\alpha = 15$ to 90 deg, normal force coefficient was estimated according to: $C_N = C_{N_{(90\text{ deg }\alpha)}} \sin^2 \alpha$. (See Ref. 18.)

Centers-of-pressure were obtained as follows:

(1) For zero deg angle-of-attack, the centers-of-pressure were taken from Figs. 3-6 and 3-8, Section 3.1 of this report.
(2) At 90 deg α, the center-of-pressure was located at the planform area centroid.
(3) From $\alpha = 0$ to 90 deg, the viscous cross-force theory of Allen, Ref. 6 was used.

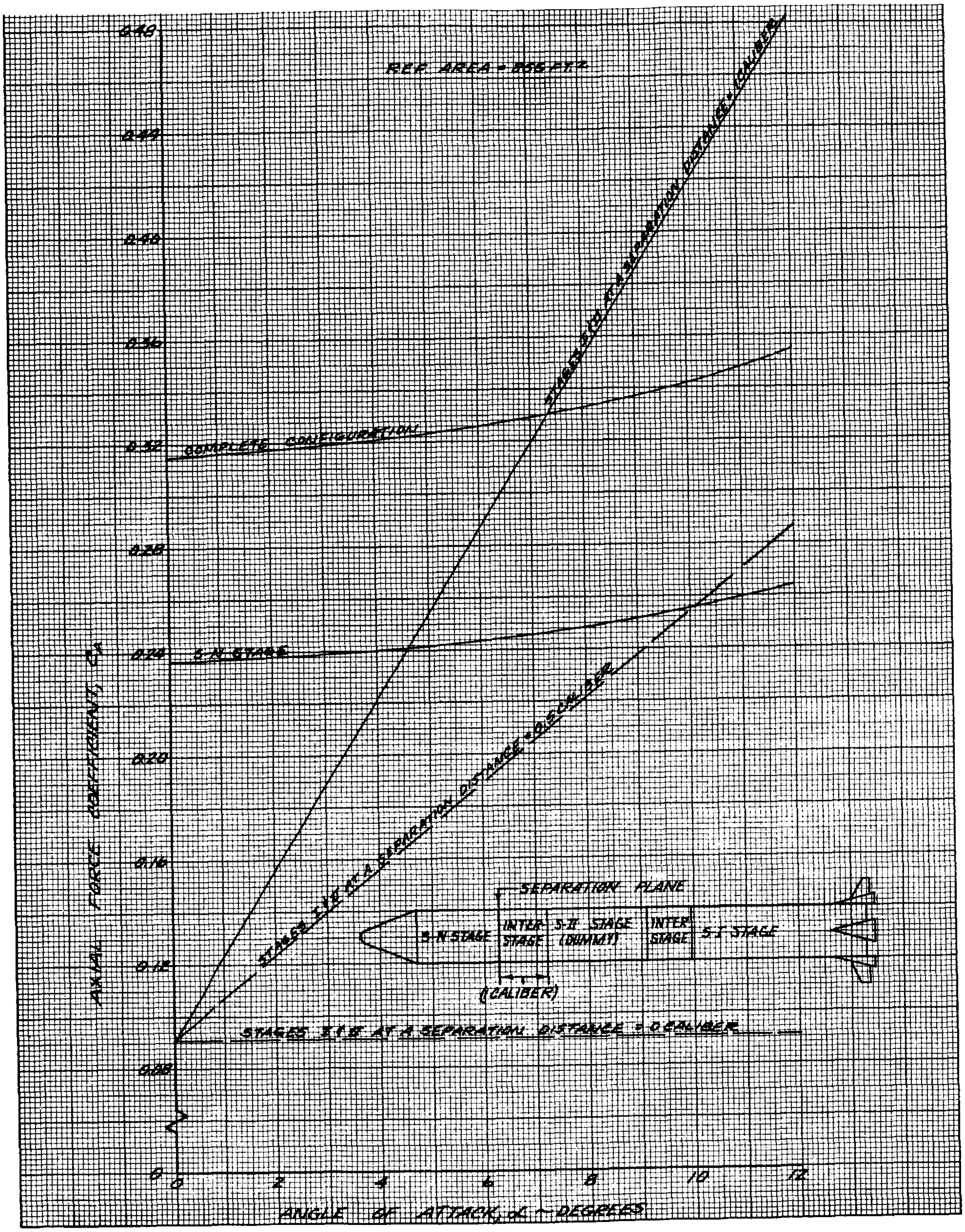

NSP 6636

Fig. 3-26 RIFT Vehicle Axial Force Coefficient at Separation versus Angle-of-Attack

HYPERSONIC CONTINUUM FLOW

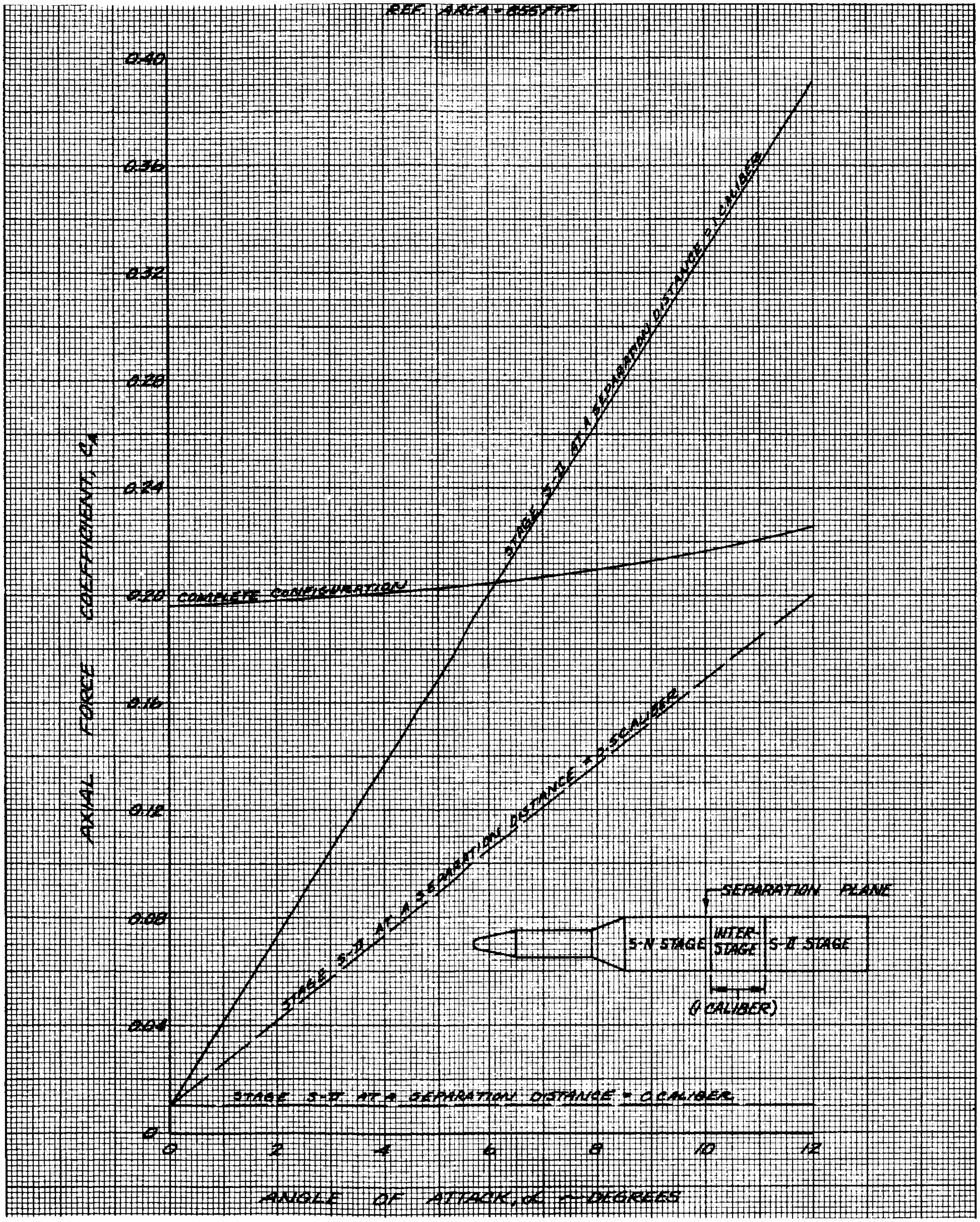

NSP 6637

Fig. 3-27 Operational Vehicle Axial Force Coefficient at Separation versus Angle-of-Attack

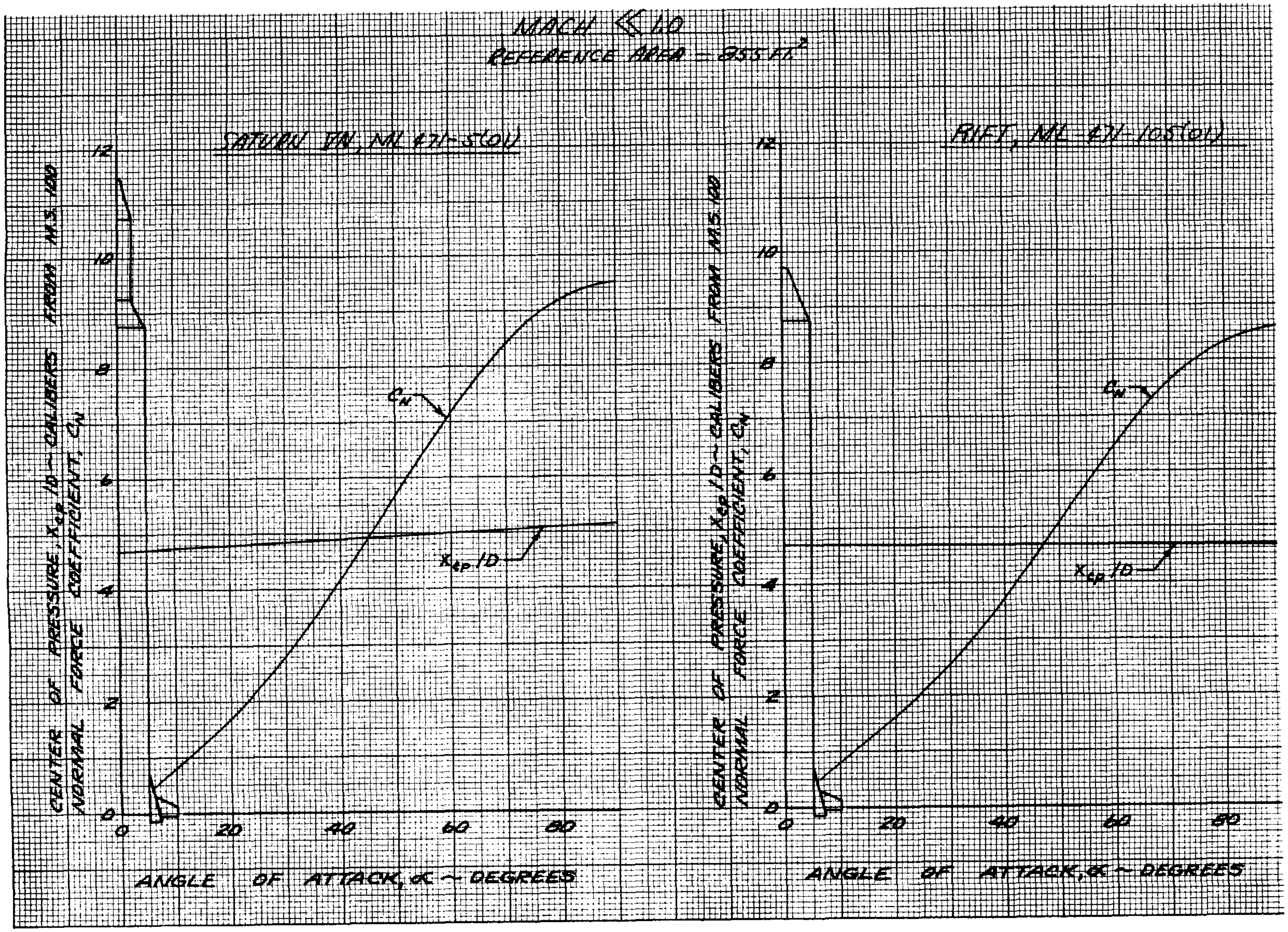

NSP 6638

Fig. 3-28 Saturn VN RIFT and Operational Vehicles Normal Force Coefficient and Center-of-Pressure at Liftoff

3.7 AERODYNAMIC DAMPING

The aerodynamic damping characteristics evaluated thus far have been restricted to the pitch damping derivative, $\frac{\partial C_m}{\partial\left(\frac{\dot{\theta} D}{V}\right)}$ This is the most significant of the damping parameters and is adequate for preliminary design analysis. Past experience in trajectory analysis has shown that the effect of aerodynamic damping on rigid-body dynamics is negligible; it is, however, necessary to establish the magnitude of these damping characteristics. The pitch damping derivative was calculated using a simplified "quasi-steady" method. The basic assumption for this method is that the induced angle-of-attack (due to pitching) acts at the location of the steady-state normal force center-of-pressure. The resulting equation is:

$$\frac{\partial C_m}{\partial\left(\frac{\dot{\theta} D}{V}\right)} = - C_{N_{\alpha_{body}}} \left(\frac{X_{cp_{body}} - X_{MC}}{D}\right)^2 \operatorname{Cos} \alpha_o - C_{N_{\alpha_{tail}}} \left(\frac{X_{cp_{tail}} - X_{MC}}{D}\right)^2 \operatorname{Cos} \alpha_o$$

where

α_o = angle-of-attack at time zero

X_{cp} = vehicle station of center-of-pressure

X_{MC} = vehicle station of moment center

C_{N_α} = $\left(\frac{d\,C_N}{d\,\alpha}\right)$ – normal-force coefficient derivative, 1/radian

D = body diameter

The pitch damping derivatives for the operational and RIFT vehicles are shown in Fig. 3-29.

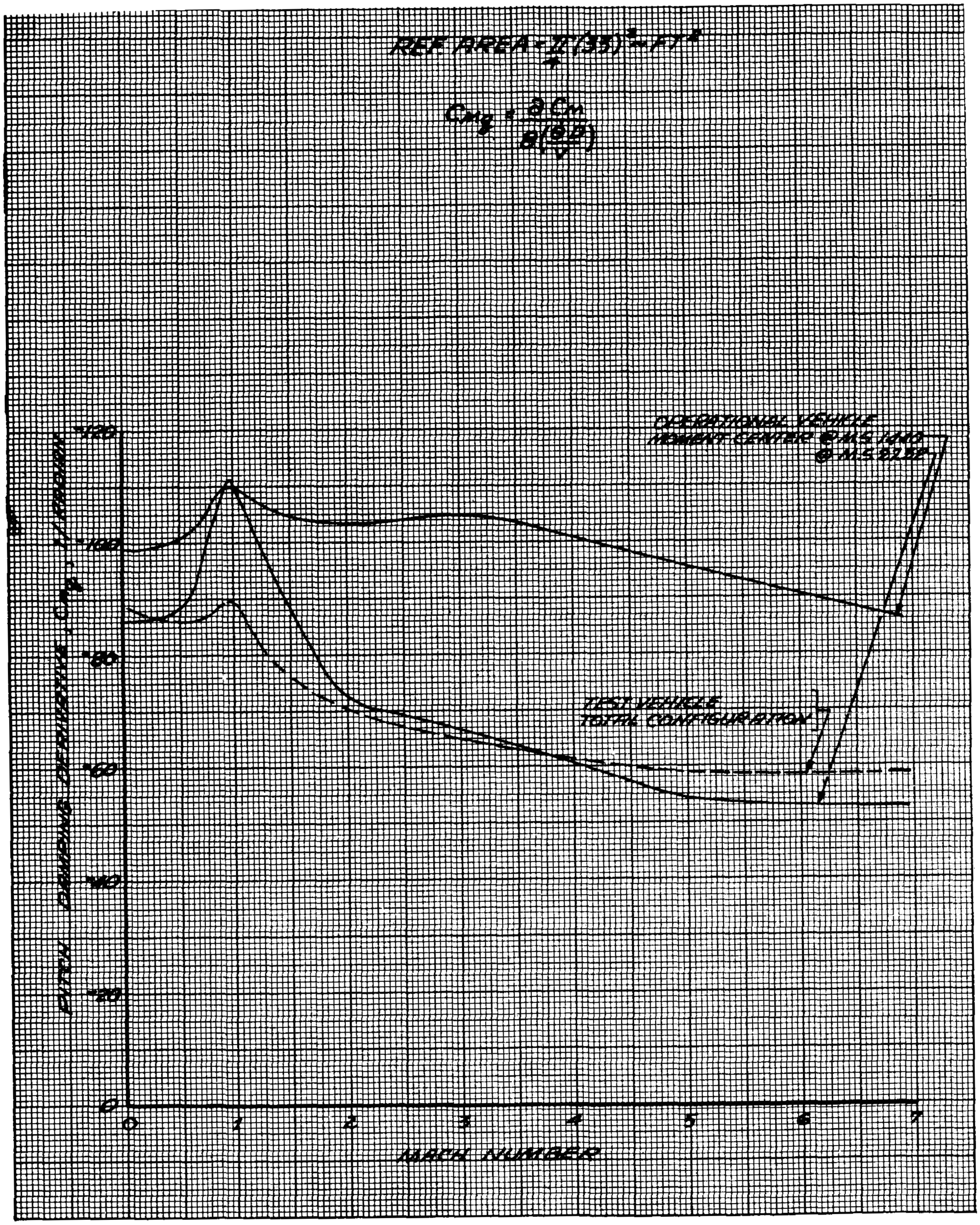

NSP 6639

Fig. 3-29 Saturn VN RIFT and Operational Vehicles
Pitch Damping Derivatives

Section 4
PERFORMANCE AND DRAG

4.1 AXIAL FORCE

Total axial force coefficients at zero zngle-of-attack for the Saturn VN Reactor-In-Flight-Test (RIFT) and operational vehicles are presented in Fig. 4-1. This total force broken into its component parts is shown in Fig. 4-2; the breakdown gives the pressure drag of the forebodies, engine shrouds, and fins; the total skin friction; and the base drag.

Forebody pressure drag of the 15- and 20-deg forecones is based upon correlation of experimental results from Refs. 8, 16, and 4*; test data for a 20-deg blunted cone; cone theory results from Ref. 43, modified Newtonian theory; and design correlation curves. The 20-deg frustrum pressure drag on the Saturn VN vehicle was determined from correlated test results and second-order shock theory. These correlation curves are shown by Fig. 4-3.

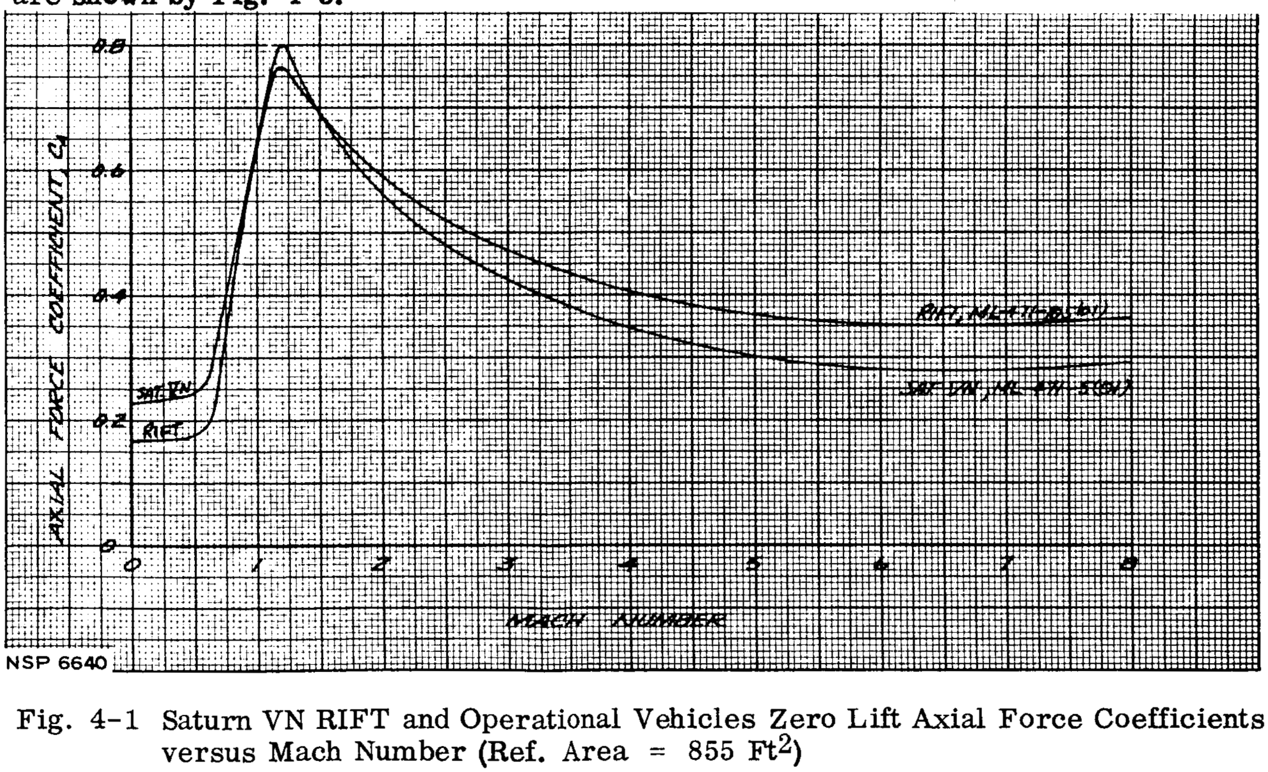

Fig. 4-1 Saturn VN RIFT and Operational Vehicles Zero Lift Axial Force Coefficients versus Mach Number (Ref. Area = 855 Ft^2)

---

*See Section 8 for list of references.

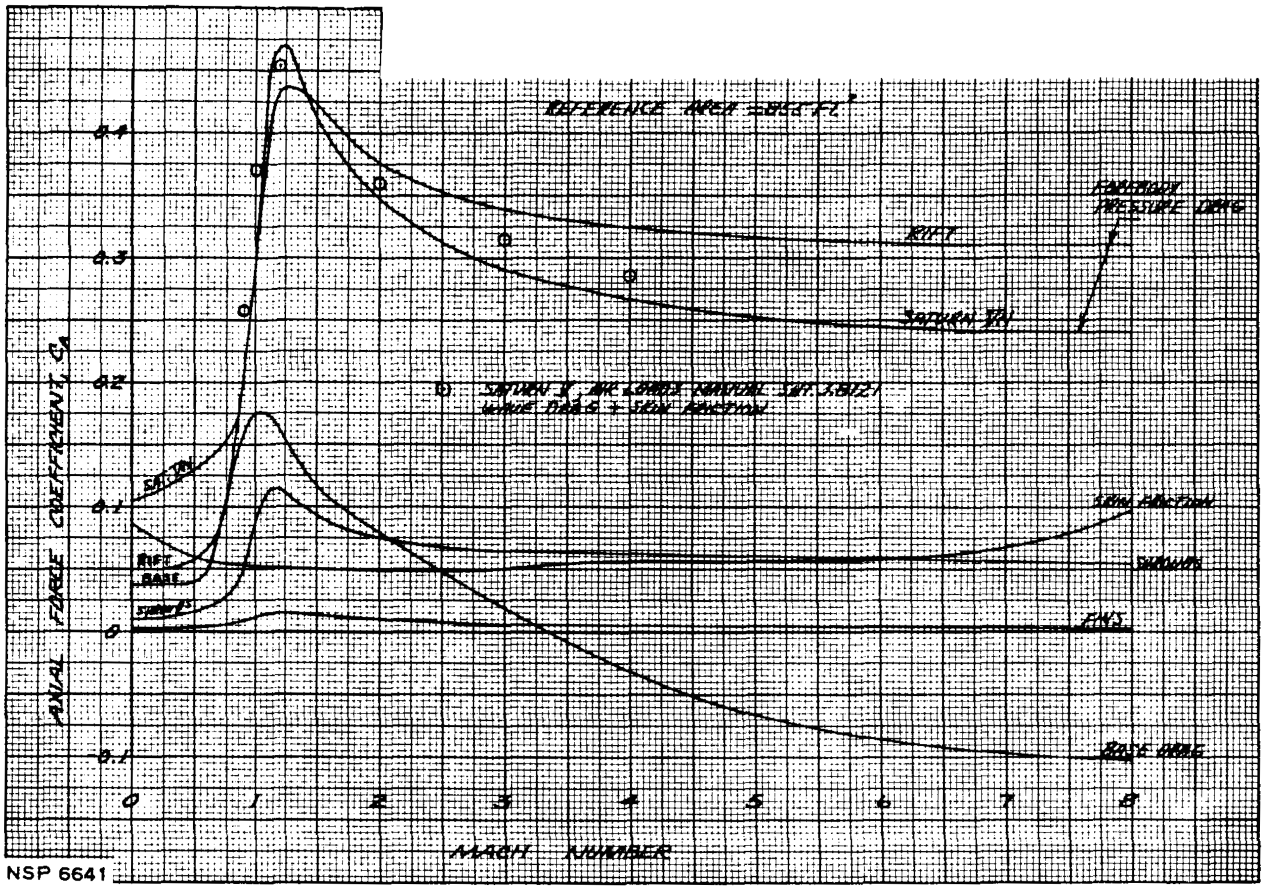

Fig. 4-2 Saturn VN RIFT and Operational Vehicles Axial Force Component Breakdown versus Mach Number

Skin-friction drag was calculated using the method of Schoenherr for which design curves are presented in Ref. 16. For calculating skin friction, the wall temperature was assumed to be 90 percent of the stagnation-point temperature. This method correlated well with the Van Driest method, Ref. 17. For specific trajectories calculated to date, the vehicles will experience flight in the slip and transition regimes. Skin friction in these areas was evaluated according to the method of Mirels, Ref. 18. Due to the similarity of the first-stage trajectories and surface areas of the RIFT and operational vehicles, the same skin-friction values were assumed as applicable for each configuration.

Axial force coefficients for the fins were based upon the theoretical methods of Ref. 12, for supersonic Mach numbers, design correlation curves in the transonic range, and

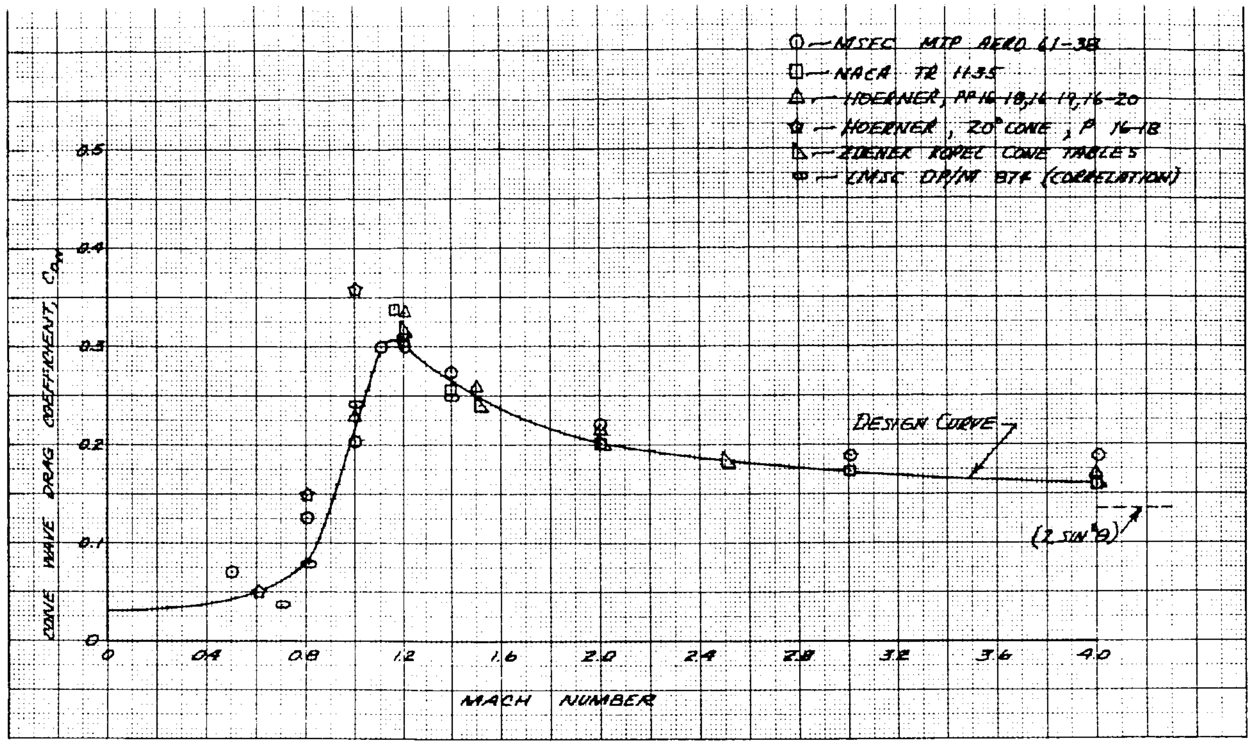

15-Degree Cone (No Base Drag)

Ref. Area = Cone Base

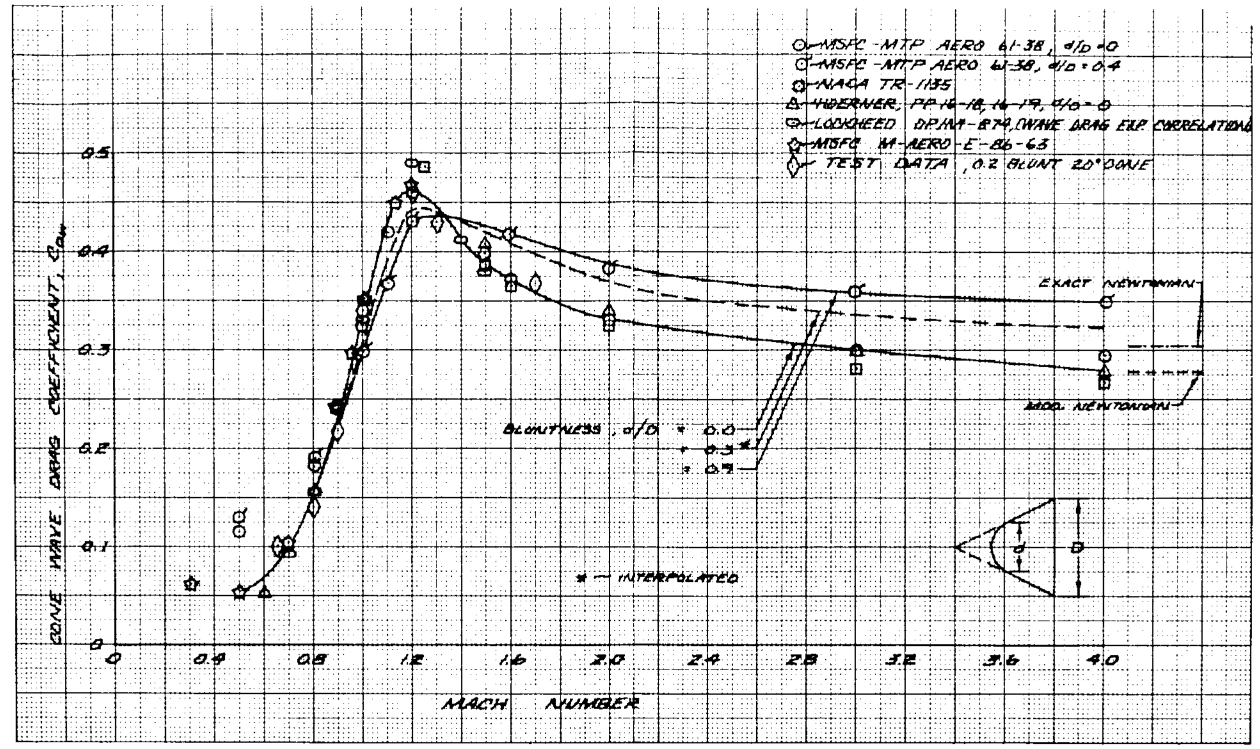

20-Degree Cone (No Base Drag)

Ref. Area = 855 ft^2

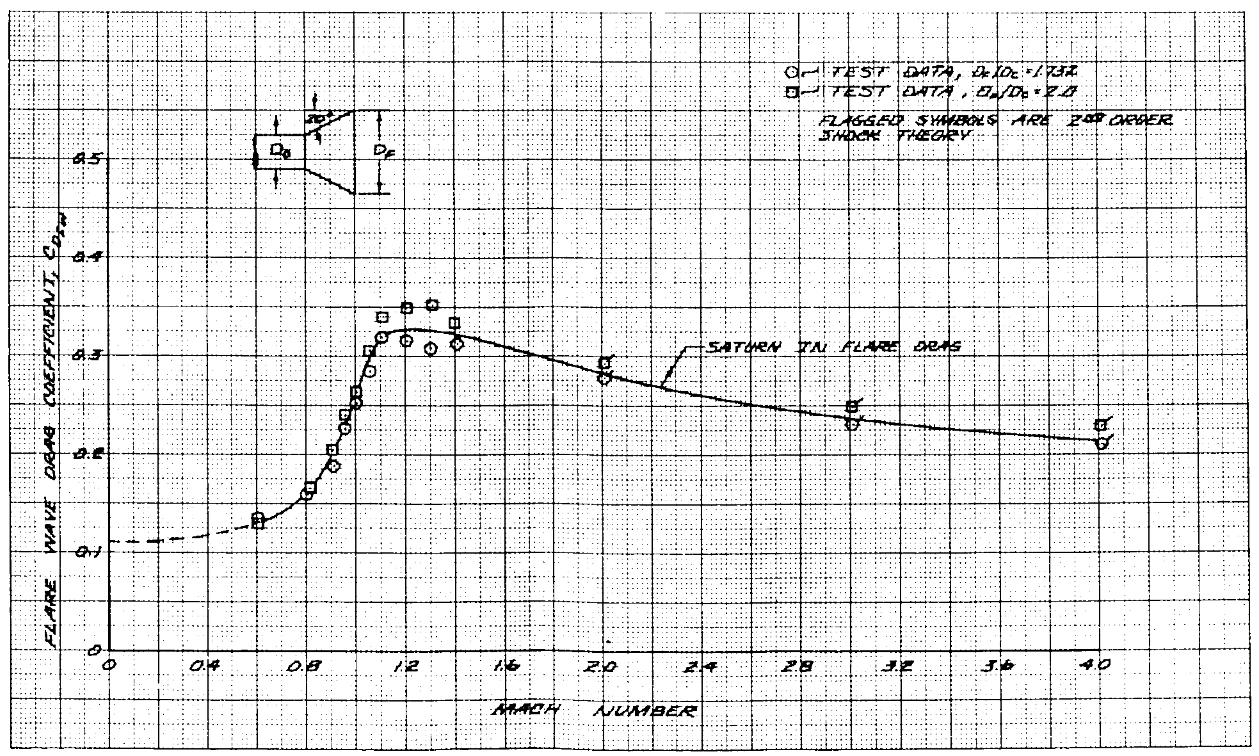

20-Degree Frustrum (Wave Drag)

Ref. Area = $\frac{\pi}{4} D_F^2$

NSP 6642

Fig. 4-3 Forebody Drag Correlation

experimental subsonic data from Ref. 16. The airfoil was assumed to have a 10 percent thickness ratio, a blunt trailing edge, and a double wedge section over 50 percent of the chord.

The base drag characteristics included the effects of aspiration and recirculation of the exhaust gases. A discussion of base drag is presented in Section 4.2.

Effects of protuberances on drag is discussed in Section 4.3. Protuberance drag values are in the order of 10 percent of the basic vehicle drag and are not included in the total drag shown in this section.

4.2 BASE FLOW

At Mach numbers << 1.0, the effect of the engine-exhaust jet is to aspirate the base region which produces a lower base pressure and an increased base drag. This effect then diminishes at transonic speeds. At higher Mach numbers and altitudes, the jet exhaust boundaries of multinozzle configurations intersect with one another and create a recirculation of the flow between the nozzles, directing the flow back toward the base and increasing base pressures.

Base pressure characteristics for the Saturn V have been previously estimated by MSFC and are presented in Ref. 19 with base scoops and in Ref. 2 with scoops removed. These results are included here and are compared with available test results for single and multinozzle configurations.

Average base-pressure coefficients (power on) for the Saturn V vehicle base configuration with and without base scoops are presented in Figs. 4-4 and 4-5. In Fig. 4-4, the pressure coefficients were correlated as a function of Mach number and in Fig. 4-5, as a function of engine-exit-to-ambient pressure ratio. Effect of the jet flow on base pressures is indicated by the position of the power-on data relative to the curve shown for no jet flow. Base-pressure coefficients for no jet flow were derived from numerous correlations of test results.

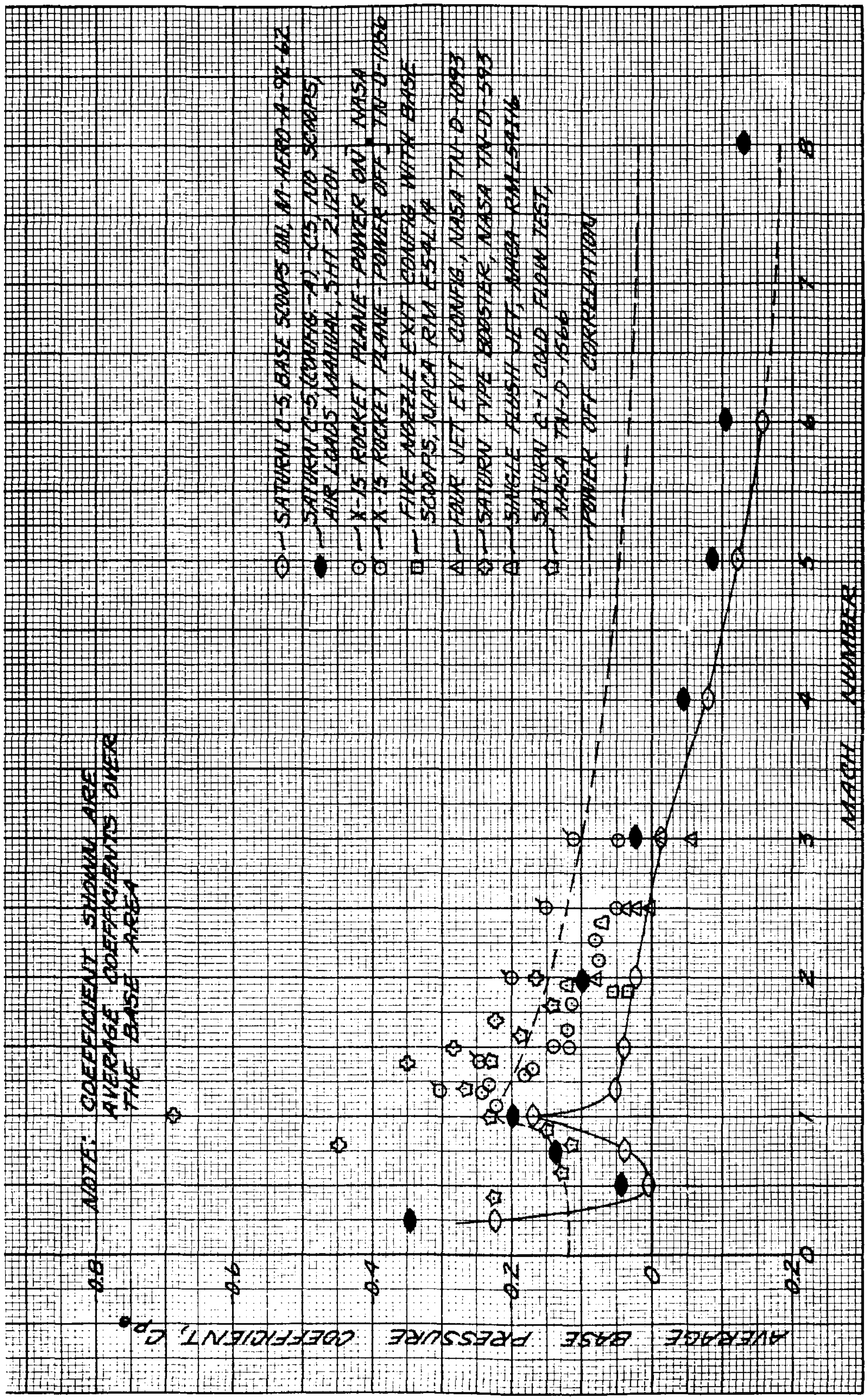

NSP 6643

Fig. 4-4 S-IC Base Pressure Coefficient versus Mach Number Correlation With Power On

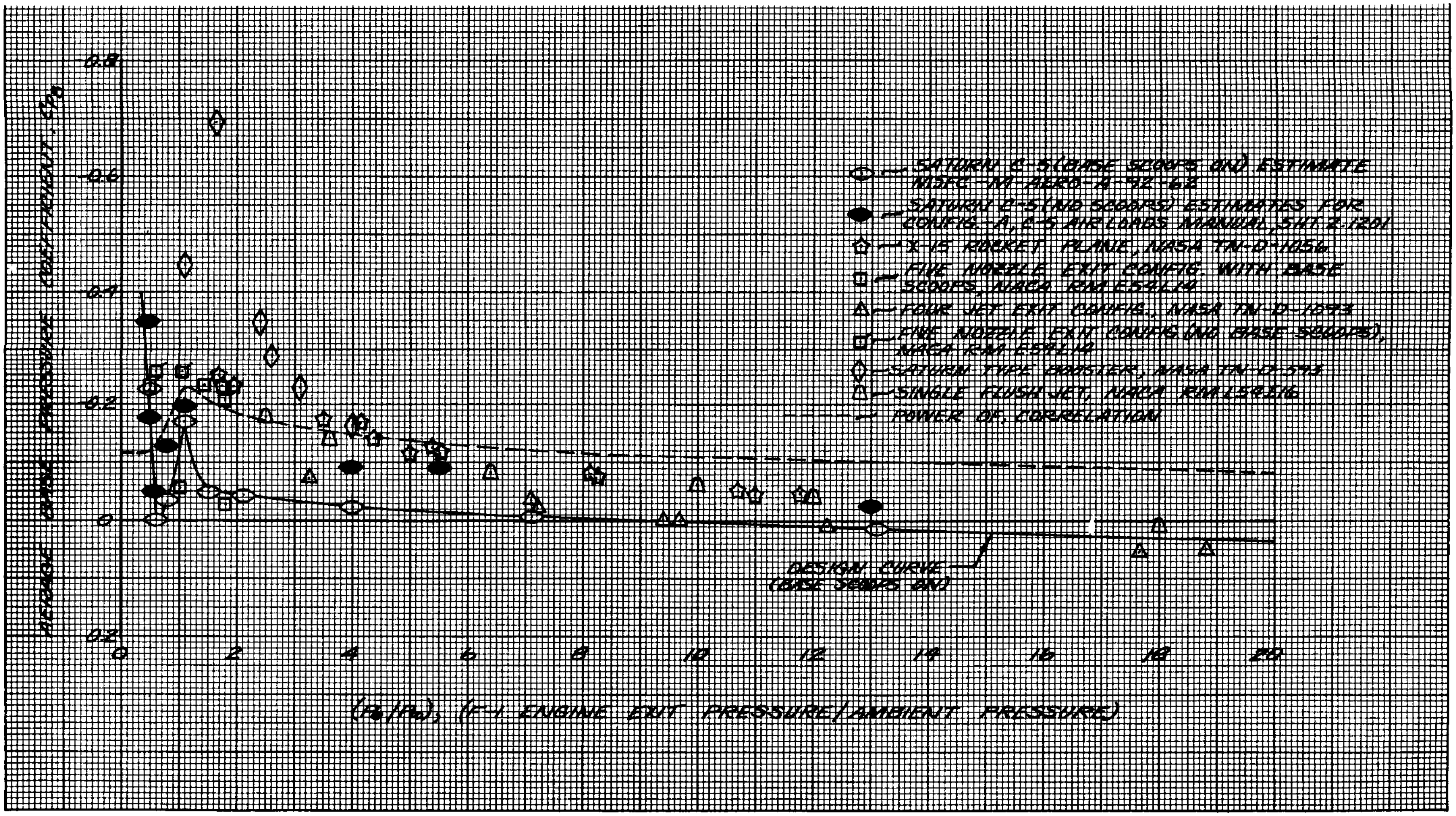

NSP 6644

Fig. 4-5 S-IC Base Pressure Coefficient versus Engine-Exit-to-Ambient Pressure Ratio Correlation With Power On

The effect of adding base scoops is seen to decrease the average (negative) base pressure which reduces base drag. This effect was also noted by the data from Ref. 22 which presents test results of a five-nozzle configuration with and without base scoops. Figure 4-5 indicates that as the pressure ratio, P_e/P_∞, increases to large values (> 20), the effect of Mach number and other variables is decreased and the base pressures can be represented by a single design curve. The preliminary base-pressure curves for the Saturn VN RIFT and operational vehicles are presented in Fig. 4-6; these were taken basically from the results presented in Refs. 2 and 21 and shown by Figs. 4-4 and 4-5. These results will be altered to reflect any further test information as such information becomes available.

4.3 PROTUBERANCES

External protuberances have a number of effects on flow characteristics. The presence of these protuberances alters the local flow field which affects local flow stability, pressures, normal and axial forces, and local heating rates. At high-subsonic and supersonic speeds, unsymmetric-unsteady shocks cause buffeting. More detailed description of these effects is noted in Ref. 21; however, in this section, only effects of protuberances on axial force will be presented.

To provide a basis for drag estimation, a general correlation was made using the data for typical vehicle protuberances from Refs. 22 through 25 and others. This correlation, Fig. 4-7, shows the ratio of protuberance drag to clean-body drag as a function of Mach number. Also shown is the estimated drag of circumferential ring stiffeners on the S-N stage and the S-II stage retrorockets.

Using Fig. 4-7 and the projected frontal areas of the S-N stage protuberances, the stage protuberance drag amounts to approximately 10 percent subsonically and 4 percent supersonically of the clean-vehicle total drag; the drag of protuberances on the first stage are not included in this number.

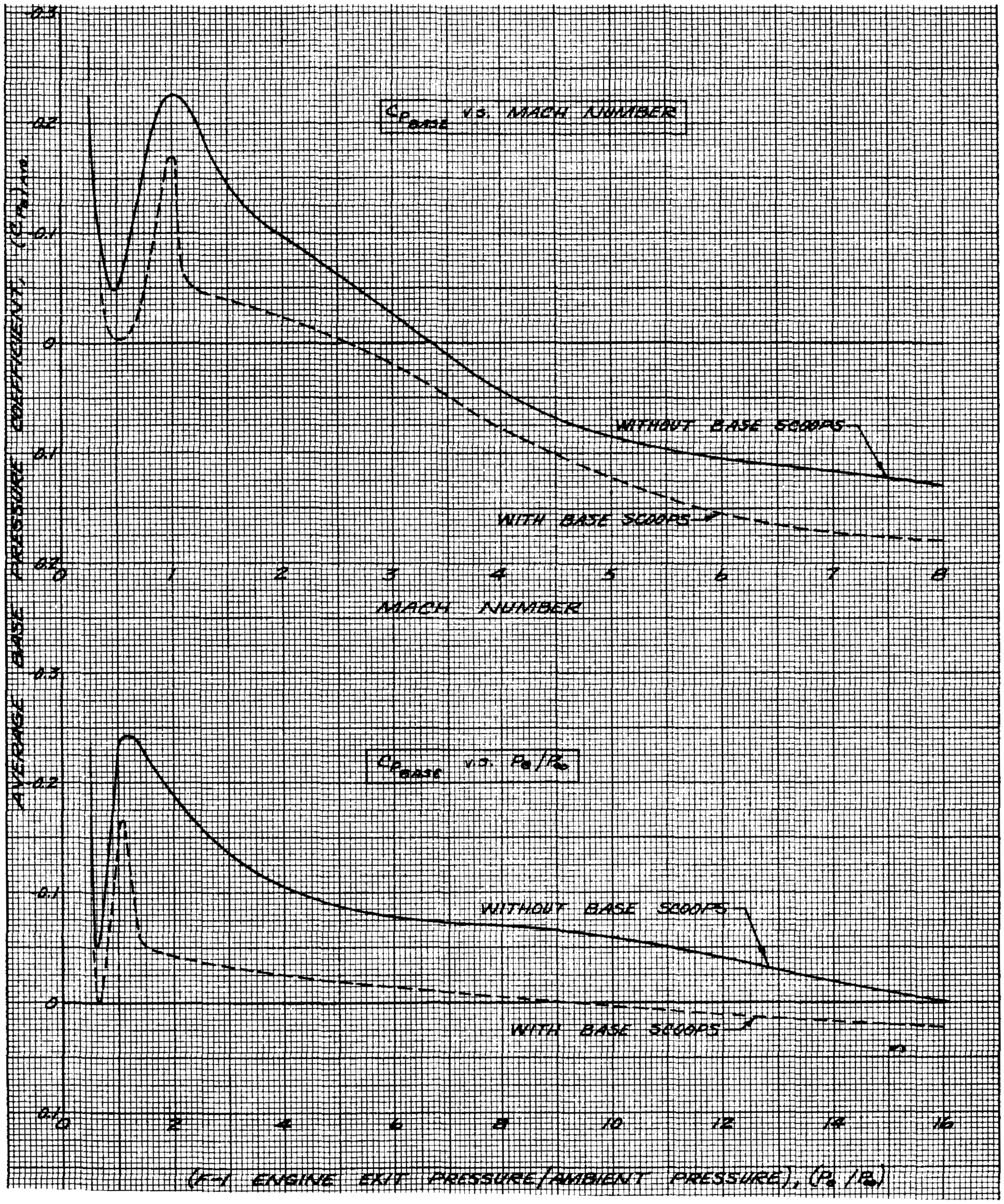

NSP 6645

Fig. 4-6 Preliminary Saturn VN RIFT and Operational Vehicles Base-Pressure Design Coefficients With Power On

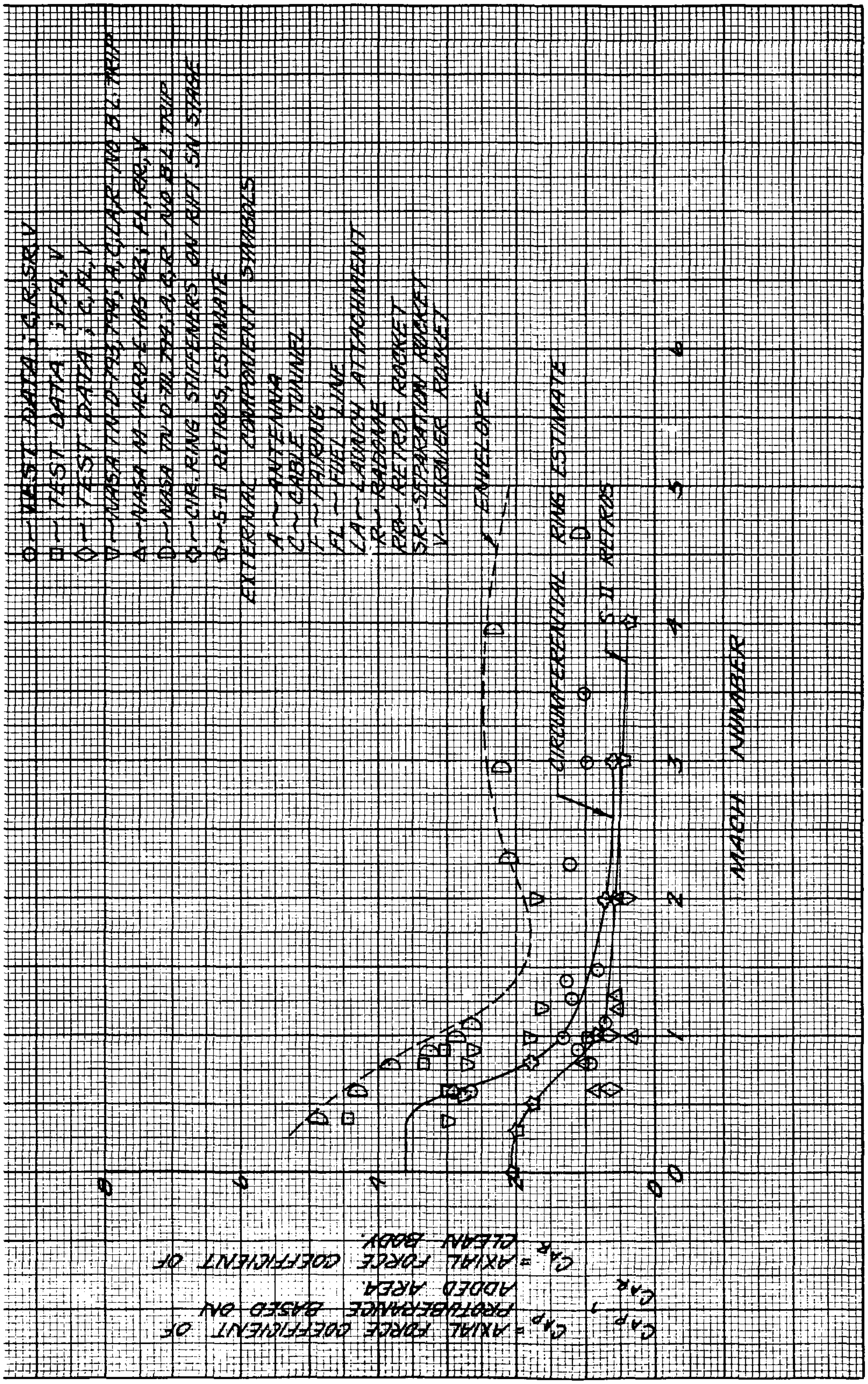

Fig. 4-7 Ratio of Protuberance Drag to Clean-Body Drag Correlation

NSP 6646

Further study and test results are necessary to determine the effect of spacing on the aerodynamic characteristics of circumferential ring stiffeners. If the spacing ratio is greater than 15, the flow may reattach between rings and increase the drag significantly. Proposed RIFT protuberances, including circumferential ring configurations, for test in conjunction with MSFC P73 wind tunnel program were presented in letter LMSC/A304012, RIFT Protuberance Data, dated 14 June 1963.

S-N Stage (RIFT) protuberances are shown in Fig. 4-8. The S-II retrorocket installation upon which protuberance drag is estimated is shown in Fig. 4-9.

4.4 EFFECT OF DRAG ON PAYLOAD

The effect on the payload capability of changing the Saturn VN vehicle drag has been determined. A trade-off factor is required in comparing internal versus external installation of retrorockets, and the evaluation of protuberance effects on flight performance. It is based upon a series of trajectories with optimized attitude computed to a 100-nm park orbit. The drag increases were simulated for the suborbital start mission mode by taking percentage increases in the drag coefficient across the Mach number range.

The payload trade-off factor, while linear with respect to drag changes is a non-linear function of S-II stage propellant loading. The drag trade-off factor for weight to the park orbit is shown in Fig. 4-10 as a function of the S-II propellant load. By presenting the data in terms of gross weight at the park orbit (a more general form than payload), the payload trade-off factor for any mission may be determined by dividing the park-orbit gross-weight trade-off by the mass ratio at park orbit departure. Thus, the change in payload weight may be calculated by

$$\Delta \text{ Payload} = \left(\frac{\partial W_{\odot}}{\partial C_D}\right) \frac{\Delta C_D}{\mu}$$

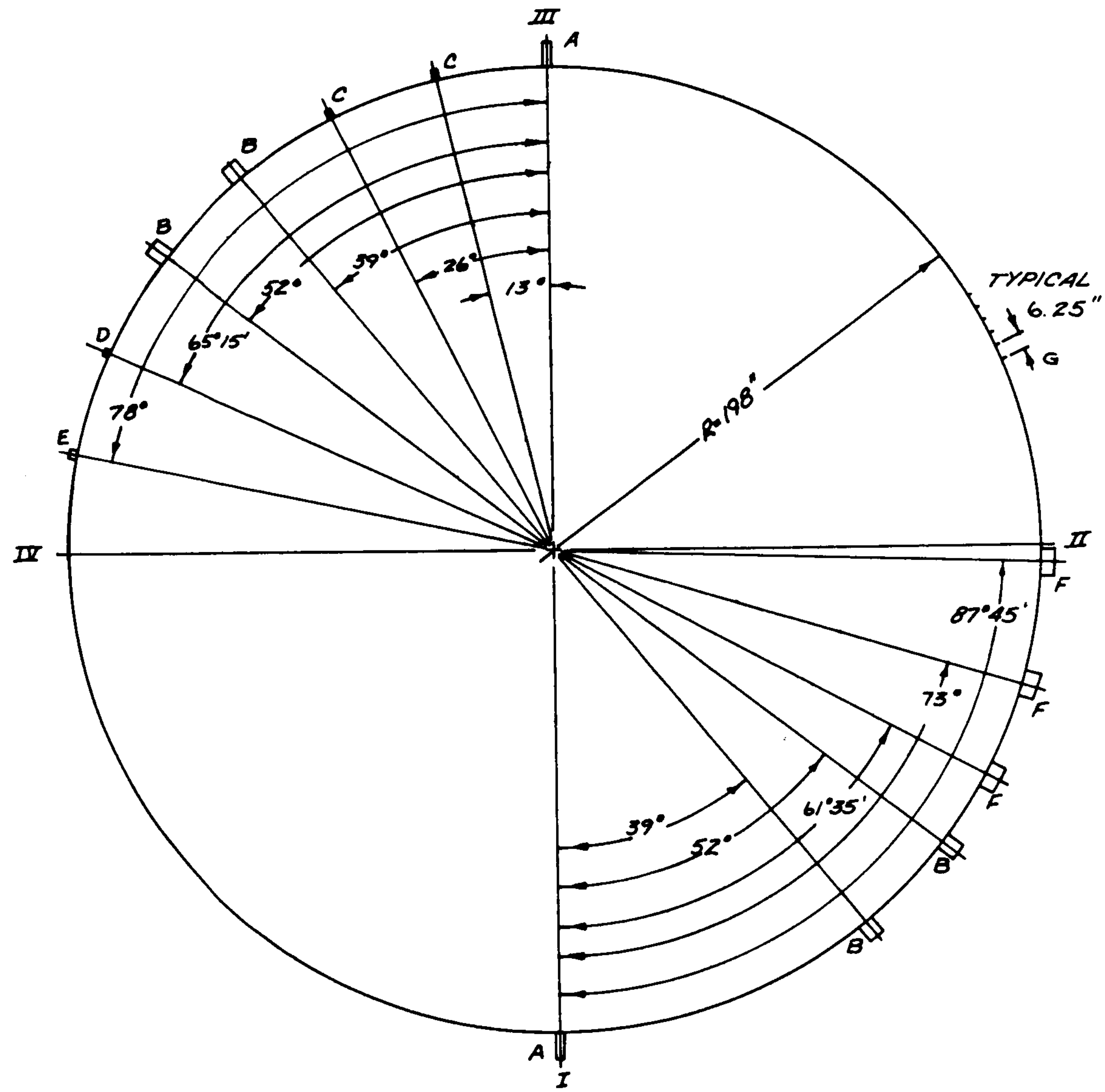

ITEM	LENGTH	WIDTH	HEIGHT	NO. REQD.	
A	27 1/2"	4 3/4"	9 1/2"	2	ANTENNAE
B	42 1/2"	6 7/8"	5 9/16"	4	
C	8 29/32"	3 1/2"	2 13/16"	2	
D	9.1"	3.4"	1.1"	1	
E	16"	4 1/2"	2.2"	1	
F	599"	12"	6"	3	TUNNELS
G	599"	0.1"	1.9"	APPROX. EVERY 6.25"	STIFFENERS

NSP 6647

Fig. 4-8 S-N Stage (RIFT) Proturberances

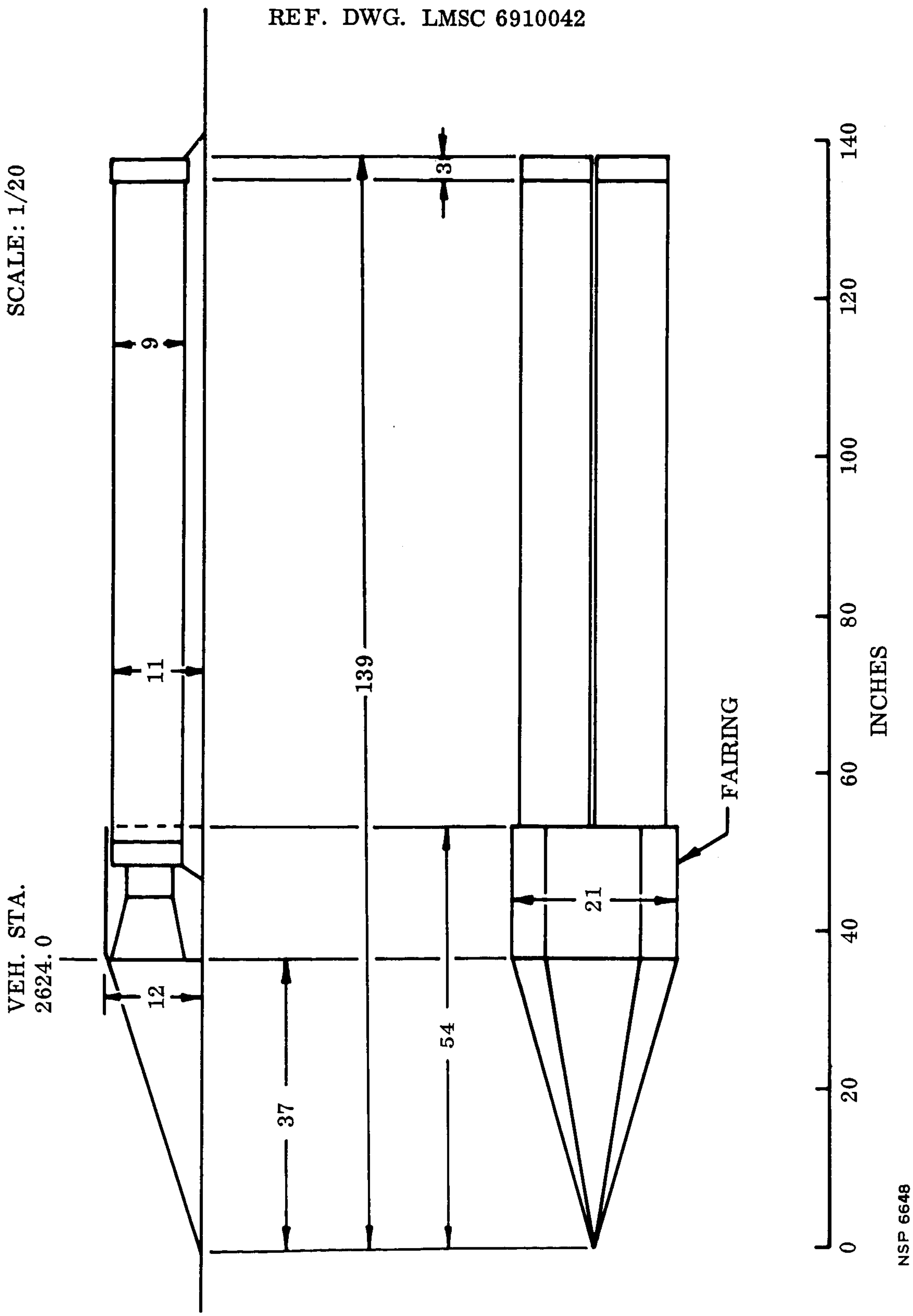

Fig. 4-9 S-N Stage (RIFT) Retrorocket Profile

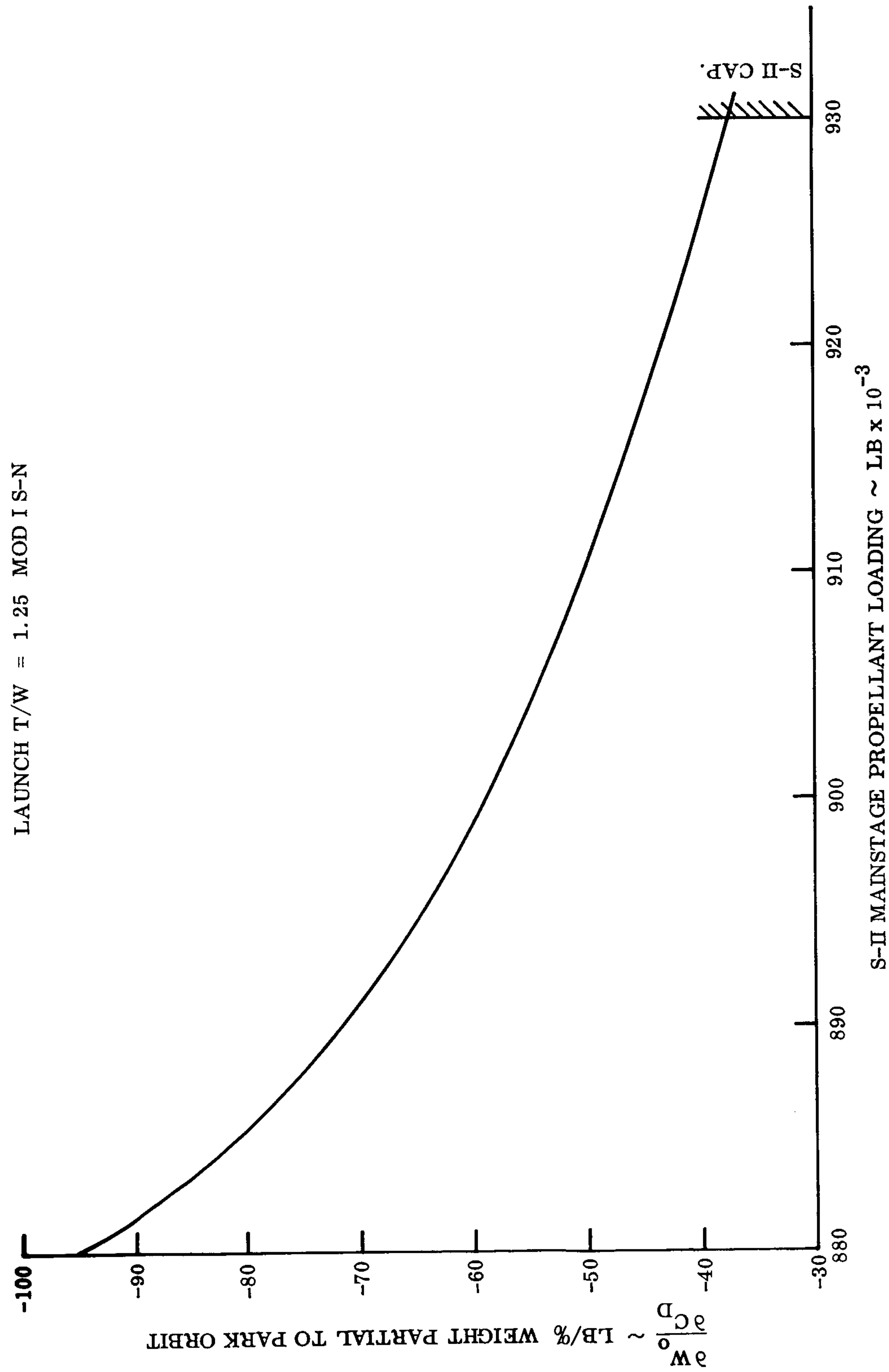

Fig. 4-10 Trade-off Factor for Weight to Park Orbit with Respect to Drag Coefficient

NSP 6649

where:

$\left(\frac{\partial W_{\odot}}{\partial C_D}\right)$ = partial for weight to park orbit

ΔC_D = percent increase of drag coefficient

μ = mass ratio at park-orbit departure

For the 176,000-lb impulse propellant capacity S-N stage using a suborbital start mode, the payload trade-off is -49 lb per percent-increase in drag coefficient for a 72-hour lunar transfer mission. As the mission velocity requirement increases, the payload decrement decreases. For missions where maximum S-II stage propellant capacity is used, the payload trade-off is reduced to -22 lb per percent-increase.

Section 5
AERODYNAMICS FOR STRUCTURAL DESIGN

5.1 NORMAL FORCE AND PRESSURE DISTRIBUTION

Linear normal force and pressure coefficient distributions are presented in this section for Mach numbers 1.2, 1.5, and 2.0. Since the theoretical methods available do not accurately predict solutions at Mach number of 1.2, reliance was placed on experimental data. Normal force coefficient distributions for the Saturn VN Reactor-In-Flight-Test (RIFT) and Saturn VN operational vehicles are shown in Figs. 5-1 and 5-2. These distributions were obtained from data in Refs 26, 27, 1, and 2. Strong emphasis was placed on results from Ref. 27, because these results concern the 20-deg blunted cone-cylinder configuration. At Mach numbers of 1.5 and 2.0 theoretical methods were combined with test results from Refs. 1, 2, and 27 to obtain the distributions.

Pressure coefficient distributions are shown by Figs. 5-3 and 5-4. Due to the greater number of pressure orifices directly aft of the cone-cylinder juncture, emphasis was placed on results of Ref. 27. At Mach number 1.5, the second-order shock method of Syvertson (Ref. 28) provides excellent agreement with experimental data.

5.2 FLUCTUATING PRESSURES

Fluctuating pressures acting on the surfaces of the S-N stage (RIFT) have been estimated for a typical trajectory. These fluctuating pressures are caused by flow separation, rocket-engine noise, normal shock waves, and the turbulent boundary-layer noise. On the launch pad and during the subsonic portion of flight, the engine noise predominates; near Mach number 1.0, normal shock waves occur to produce large pressure fluctuations over a short time duration, and the turbulent boundary-layer noise predominates, with lesser pressures, in the supersonic speed range. Fluctuating pressures affect panel fatigue life, especially when the characteristic frequencies of the pressures and panel coincide.

Figure 5-5 shows the overall or total root-mean-squared (r.m.s.) fluctuating pressure acting on the cylindrical surface of the S-N stage during a typical trajectory. This is a summation of maximum r.m.s. pressures oscillating at all frequencies and originating from engine noise, unsteady normal shocks, and the turbulent boundary layer. These values are to be superimposed upon the steady-state pressure distribution. Figures 5-6 through 5-9 present the oscillation frequencies and associated r.m.s. pressures generated by each source (frequency distributions or power spectrums). Figure 5-5 shows that engine noise is predominant over the initial 42 sec of flight time with the spectrum of Fig. 5-6 applicable. From about 42 to 50 sec, boundary layer and engine noise are both significant, and the distribution shown in Fig. 5-7 applies. In the flight region where the missile is affected by the normal shock (50 to 58 sec), the spectrum of Fig. 5-8 may be used for frequencies below 550 cps and that of Fig. 5-9 for higher frequencies. Above Mach number 1.0 (59 sec), pressure fluctuations caused by the boundary layer are predominant, and spectrums from Fig. 5-9 should be used.

The form of the functions used in the spectrum should be noted; the pressure is given as r.m.s. pressure squared/one-cycle frequency bandwidth, i.e., the value of the function at any frequency represents the square of the r.m.s. pressure acting at the specified frequency. If the combined r.m.s. pressure-level acting in a range (or band) of frequencies is desired, an integration between the limiting frequencies is performed to give the square of the desired answer. The pressure levels in Fig. 5-5 may be obtained from an integration over the entire frequency range. The logarithmic scale of frequency should be treated carefully; the pressure levels appear quite low at the individual frequencies above 1,000 cps, but note that the high-frequency scale is compressed, and these low pressures act over a very large frequency range (9,000 cps or more, i.e., $P^2_{rms} \approx (P^2_{ave/cps}) (\Delta f)$. An illustrative example appears in Fig. 5-7 where the overall pressures (integrated area) associated with the two dotted curves are equal. These results would be more obvious if a linear scale were used, but space limitations make this approach impractical.

The engine spectrum is shown in Fig. 5-6 for static firing conditions. Estimates indicate that this distribution may be used for all the overall pressure conditions shown in

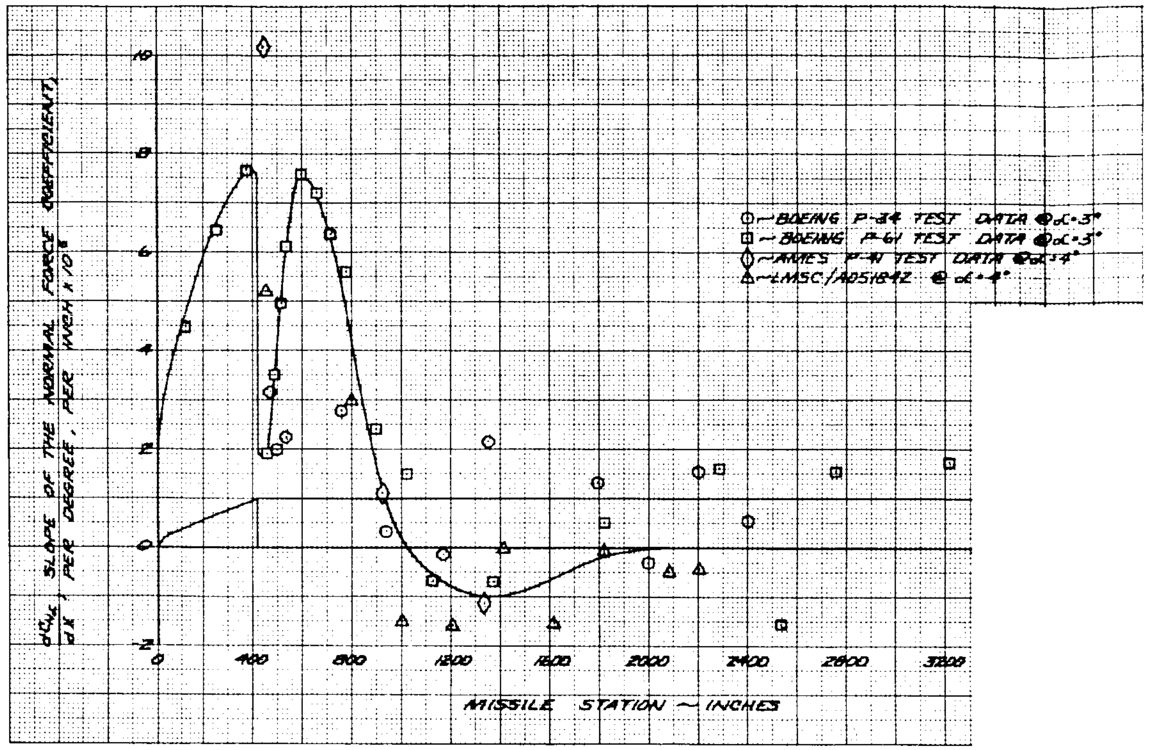

Mach Number = 1.2

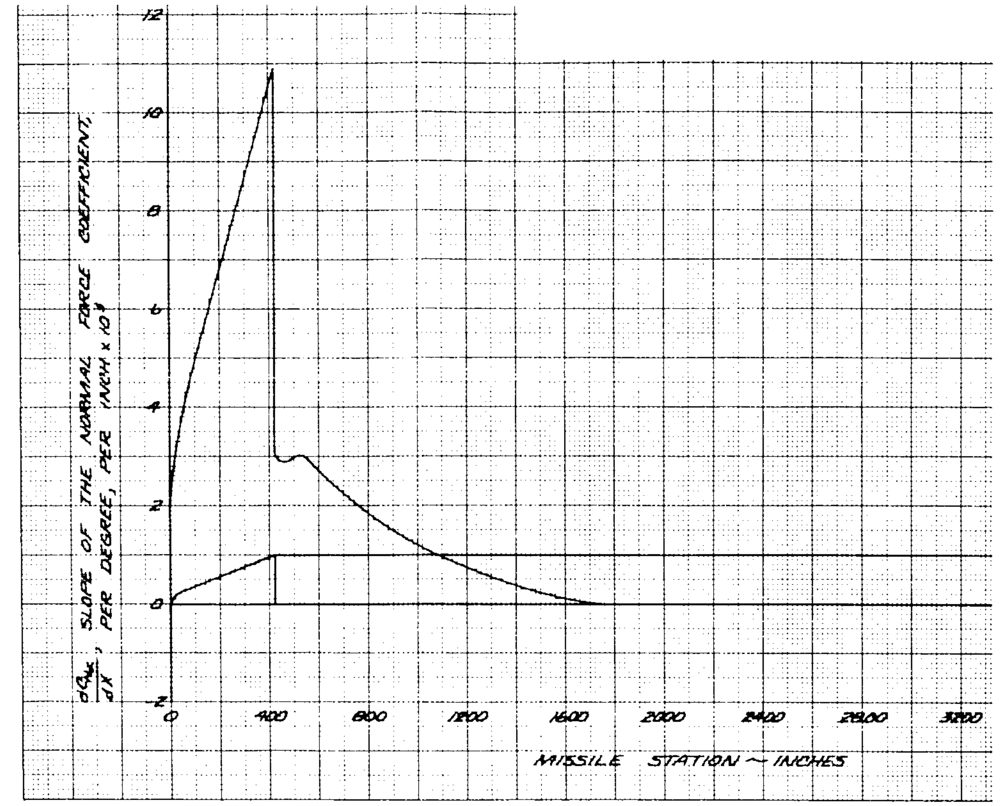

Mach Number = 1.5

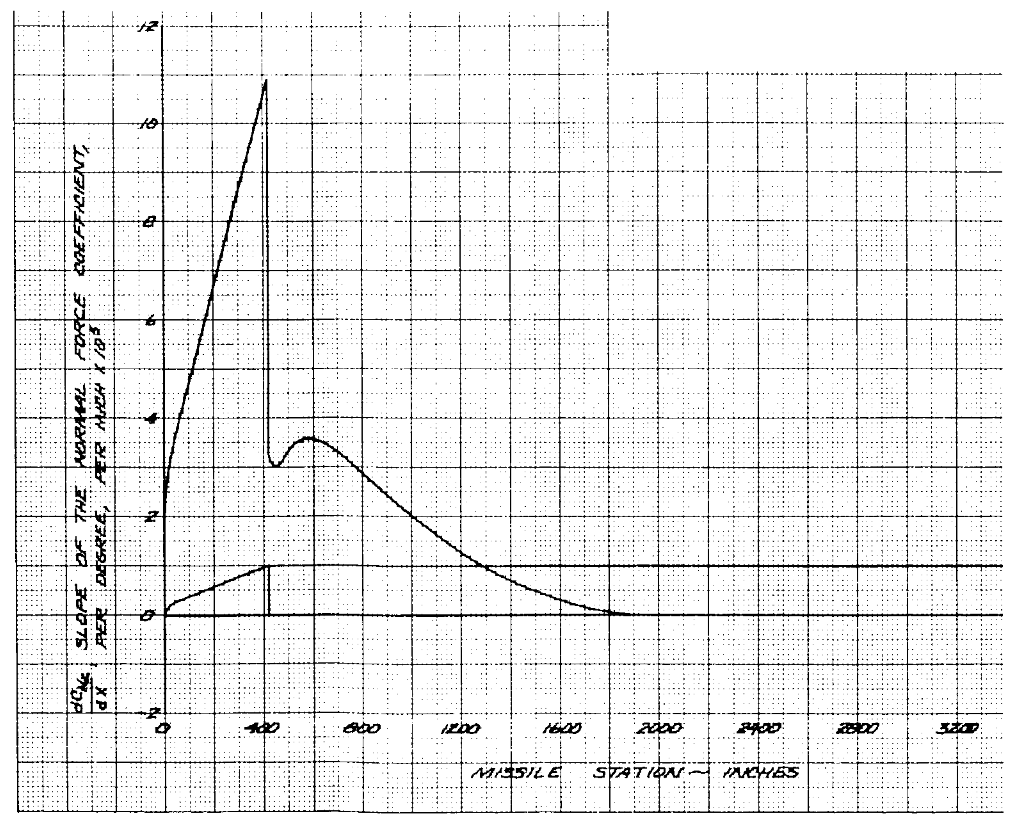

Mach Number = 2.0

NOTES: Ref. Area = 855 Ft^2
α = 0 Deg

Fig. 5-1 RIFT Vehicle Normal Force Coefficient Distributions

NSP 6650

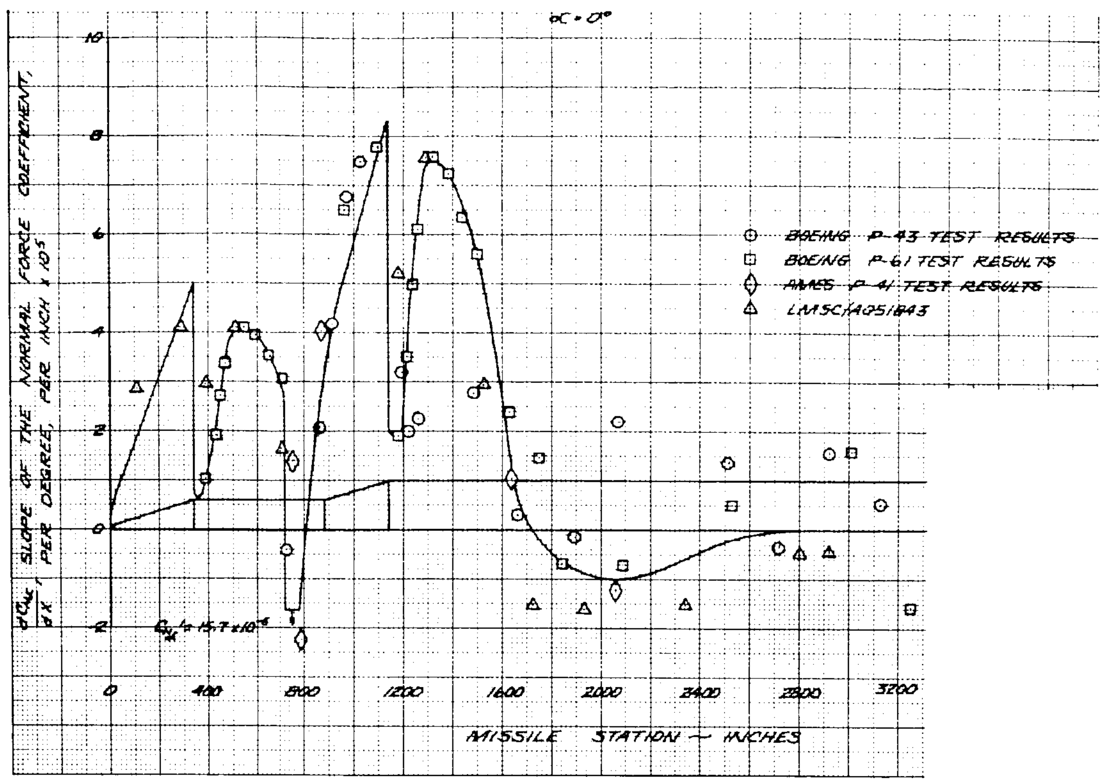

Mach Number = 1.2

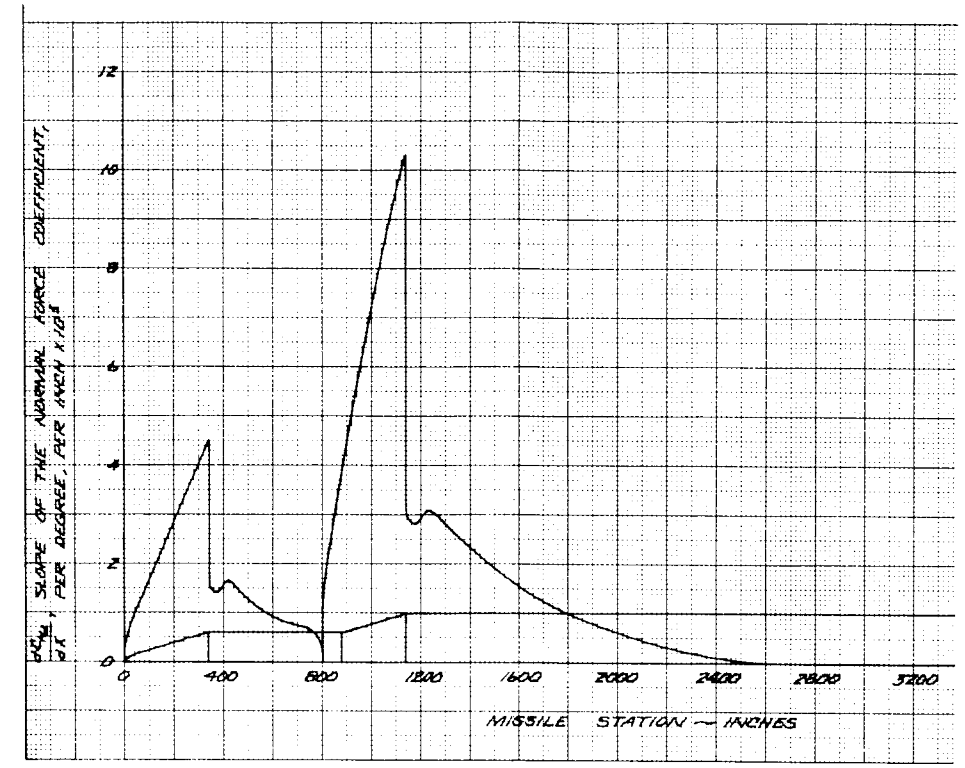

Mach Number = 1.5

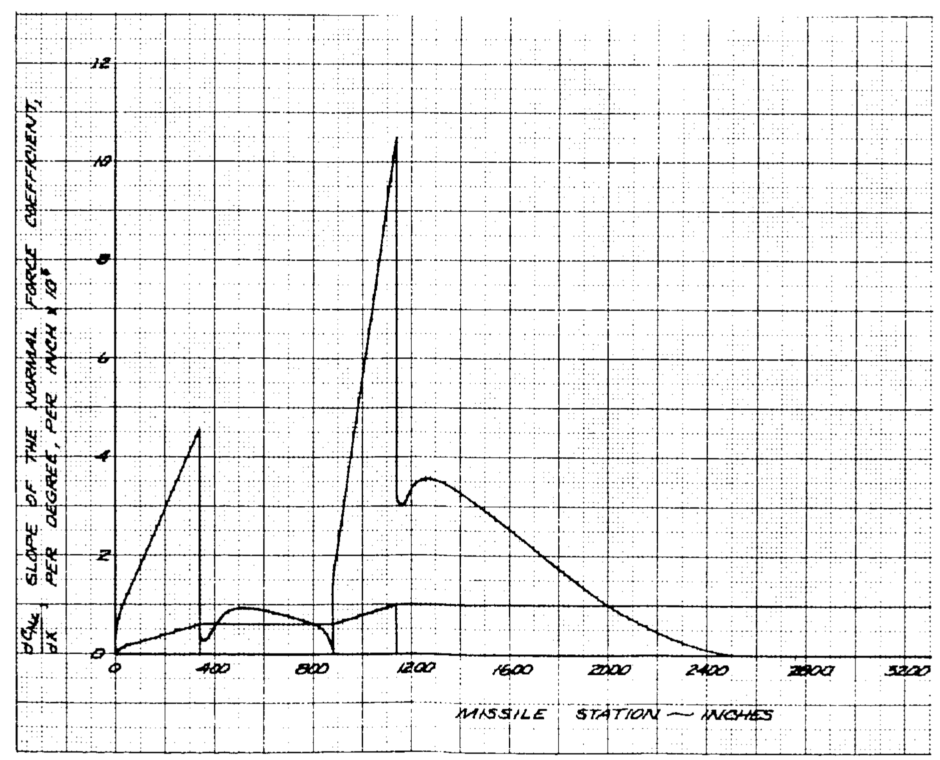

Mach Number = 2.0

NOTES: Ref. Area = 855 Ft^2
α = 0 Deg

NSP 6651

Fig. 5-2 Operational Vehicle Normal Force Coefficient Distributions

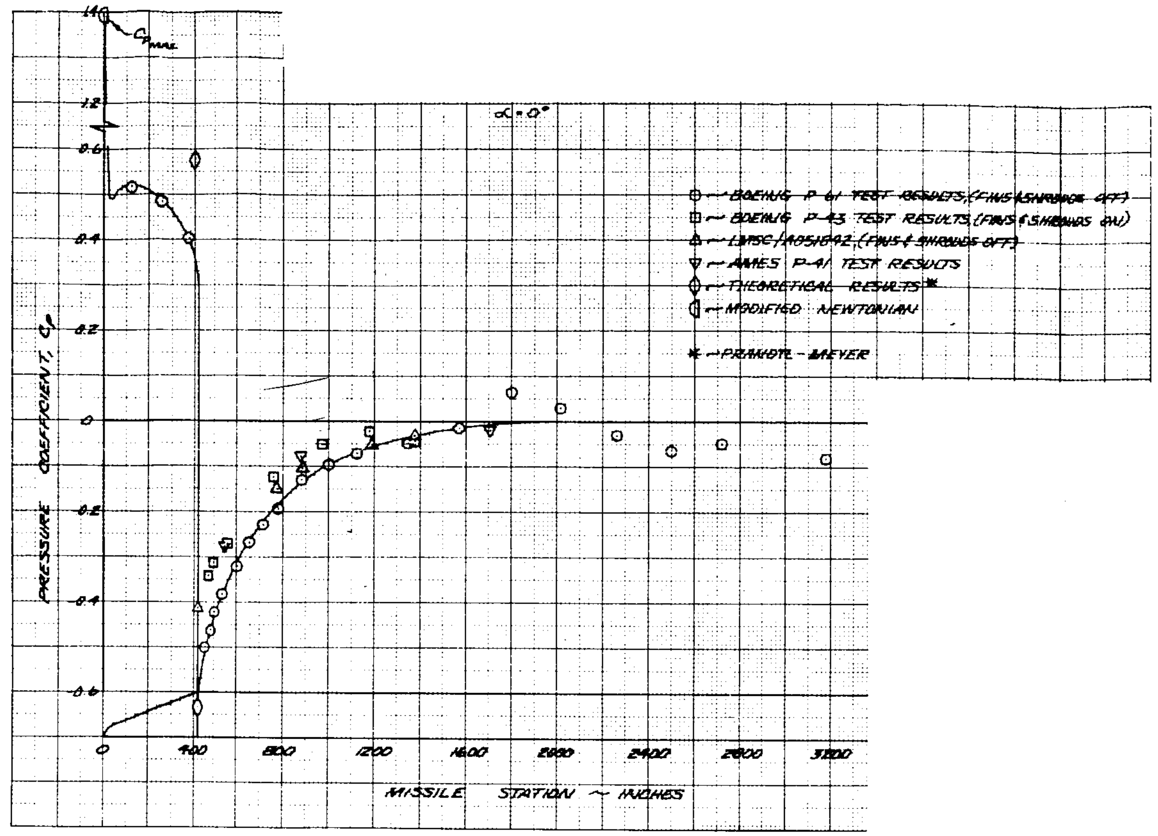

Mach Number = 1.2

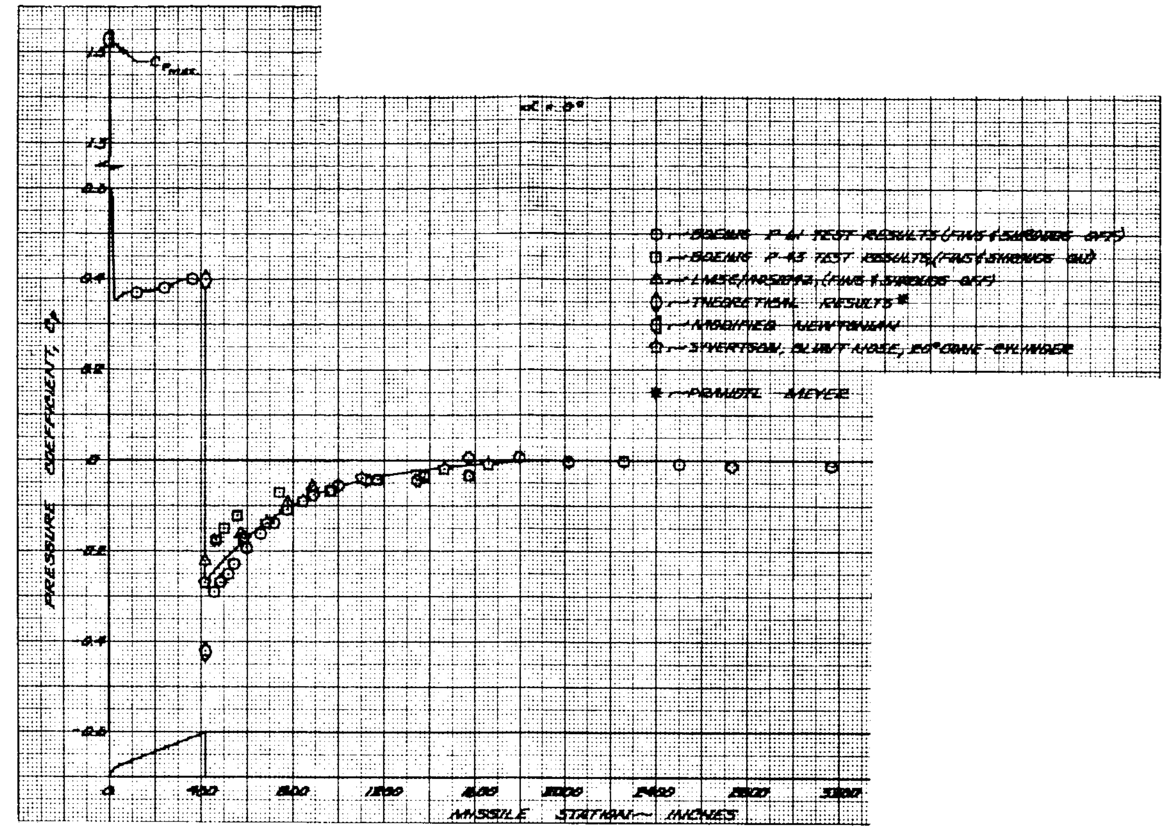

Mach Number = 1.5

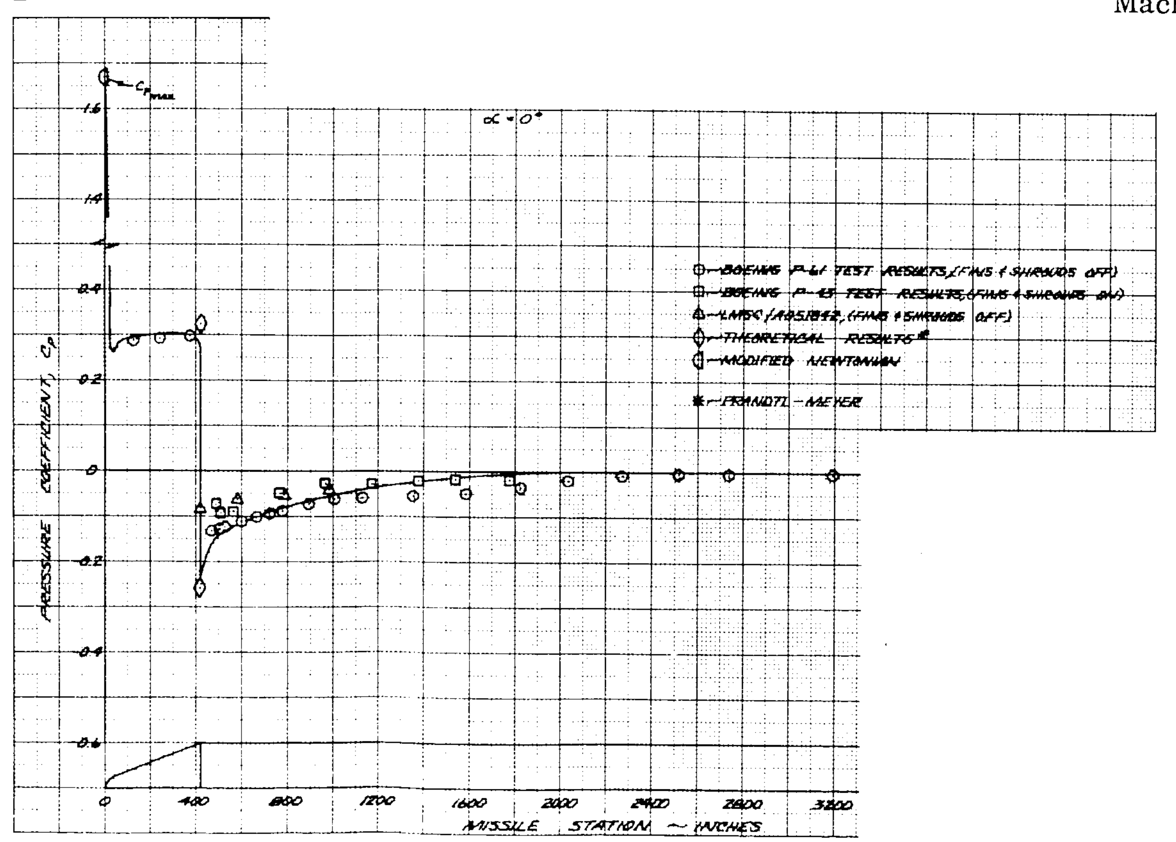

Mach Number = 2.0

NSP 6652

Fig. 5-3 RIFT Vehicle Pressure Coefficient Distributions

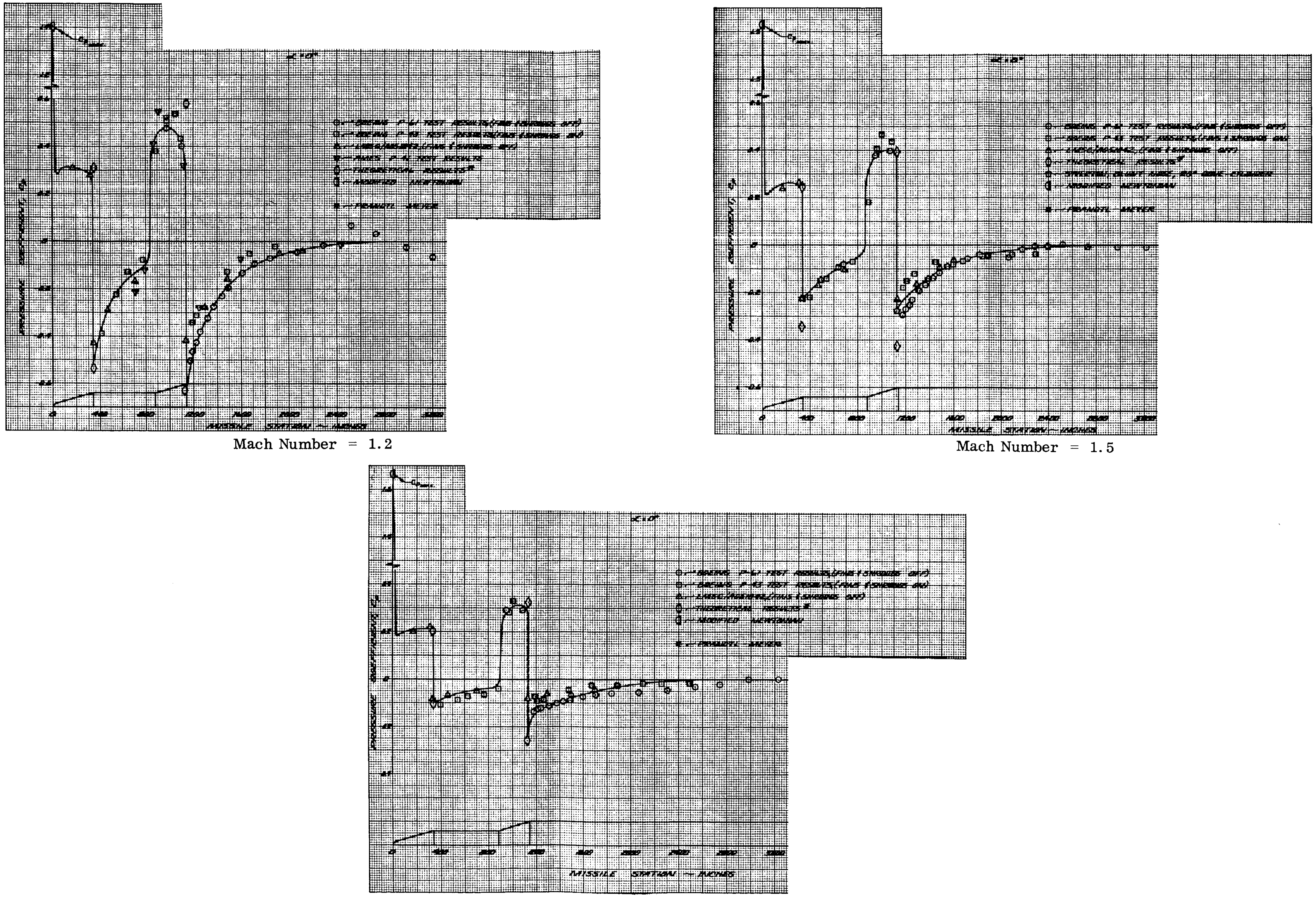

Mach Number = 1.2

Mach Number = 1.5

Mach Number = 2.0

6653

Fig. 5-4 Operational Vehicle Pressure Coefficient Distributions

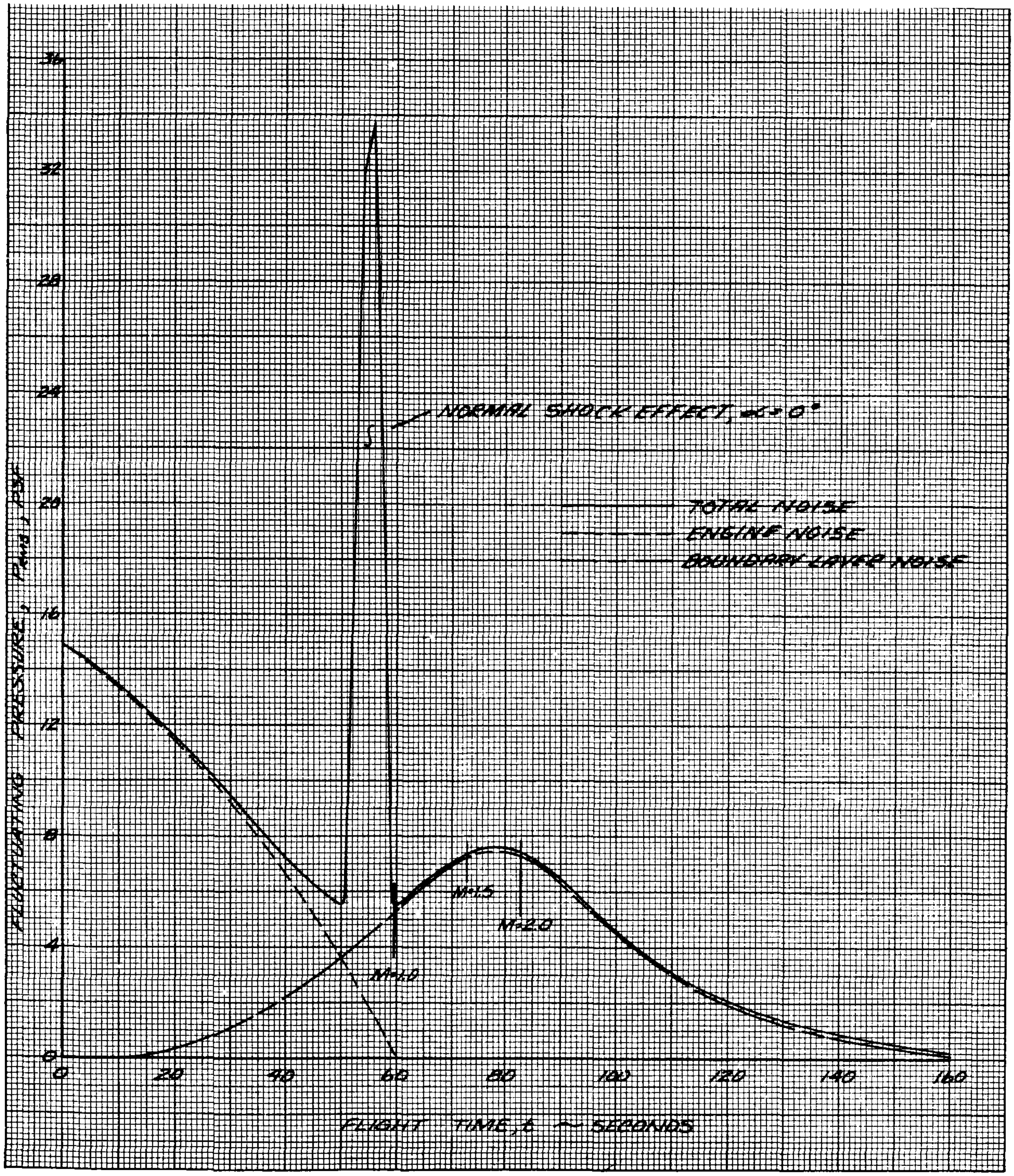

NSP 6654

Fig. 5-5 S-N Stage (RIFT) Fluctuating Pressure versus Flight Time

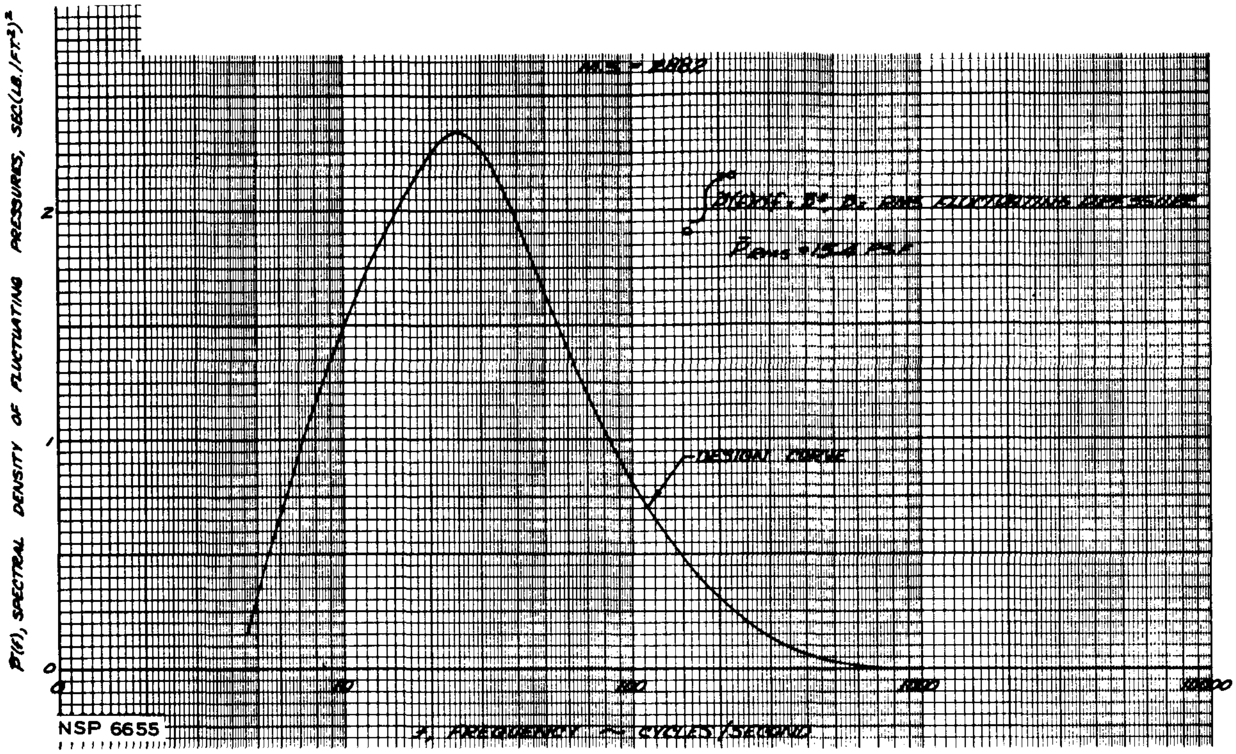

Fig. 5-6 Fluctuating Pressure Spectrum on S-N Stage (RIFT) Under Static S-IC Firing

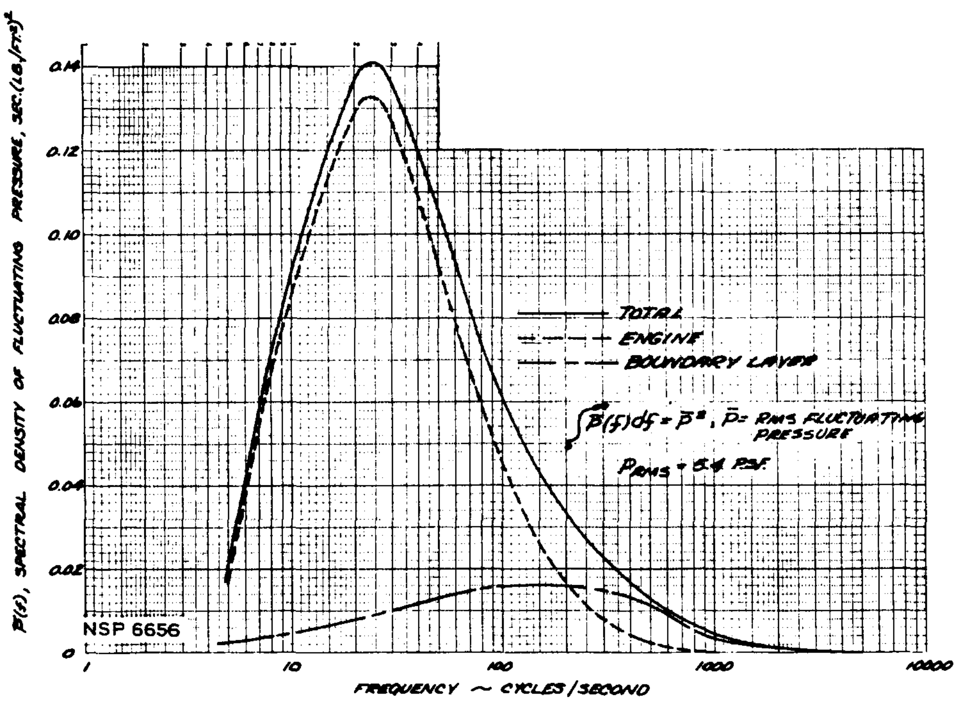

Fig. 5-7 Fluctuating Pressure Spectrum on Aft Section ot S-N Stage (RIFT) at Flight Time of 49.5 Seconds

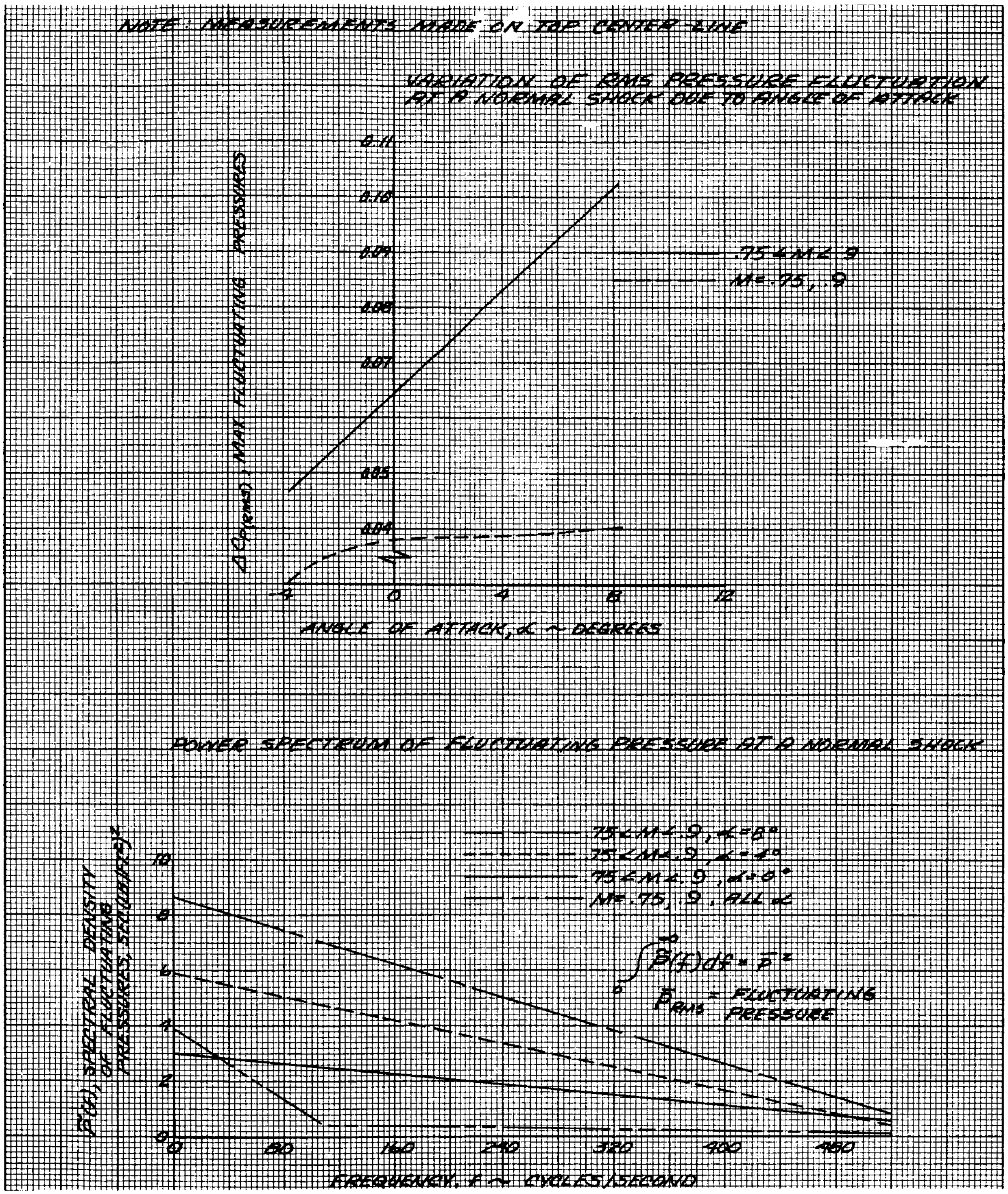

NSP 6657

Fig. 5-8 Fluctuating Pressures Due to Normal Shocks

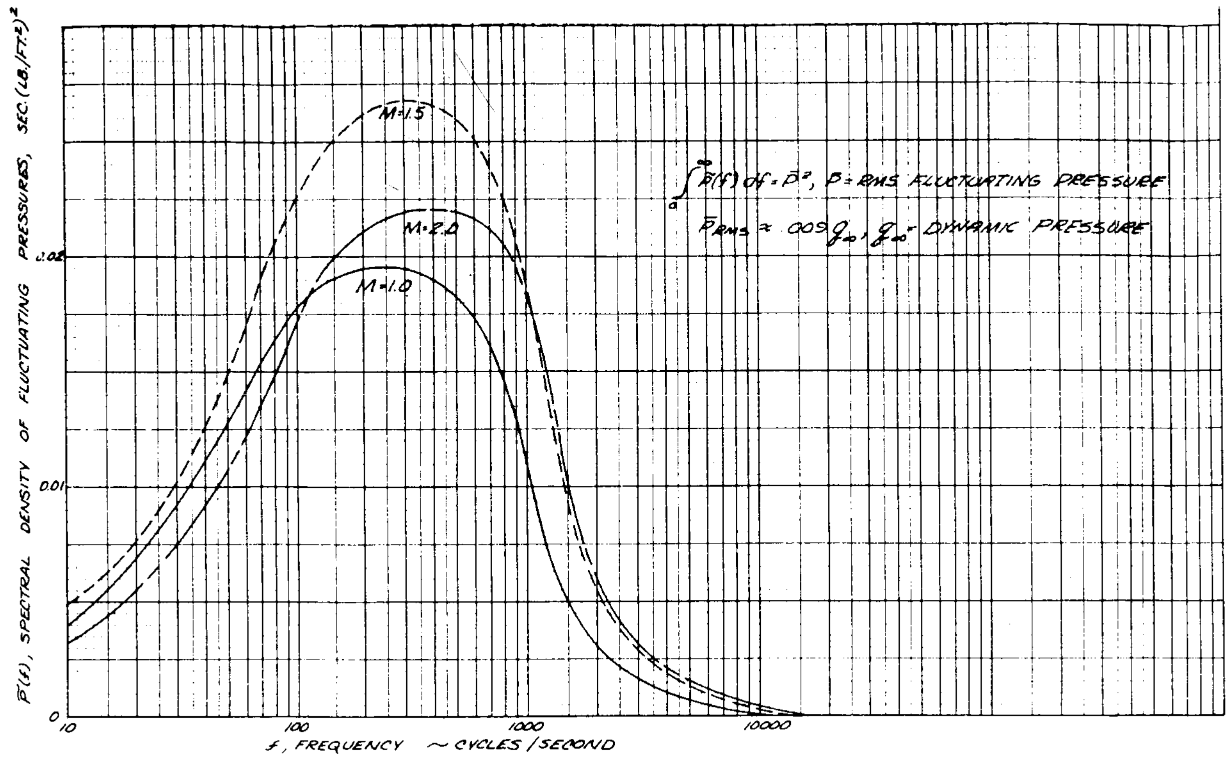

Distance Downstream of Frustrum-Cylinder Joint = 0 In.

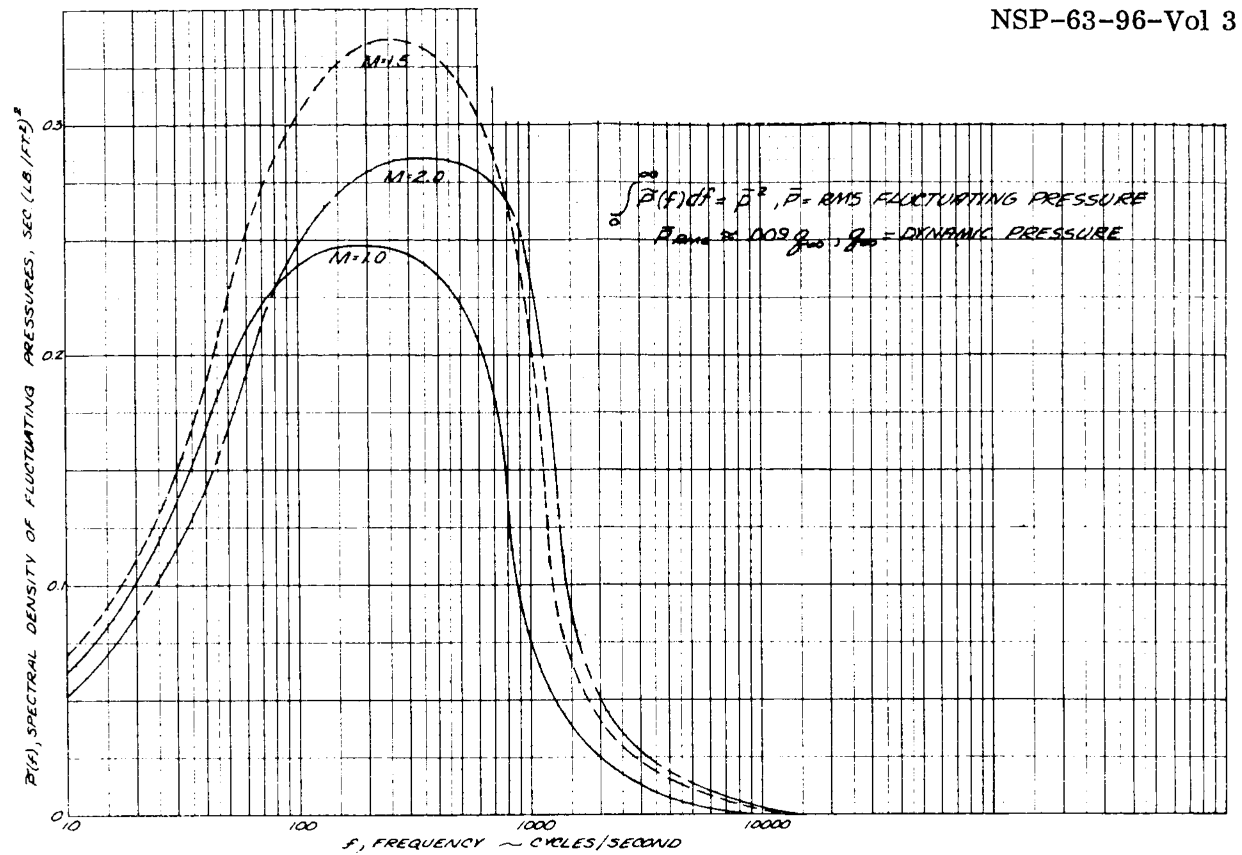

Distance Downstream of Frustrum-Cylinder Joint = 300 In.

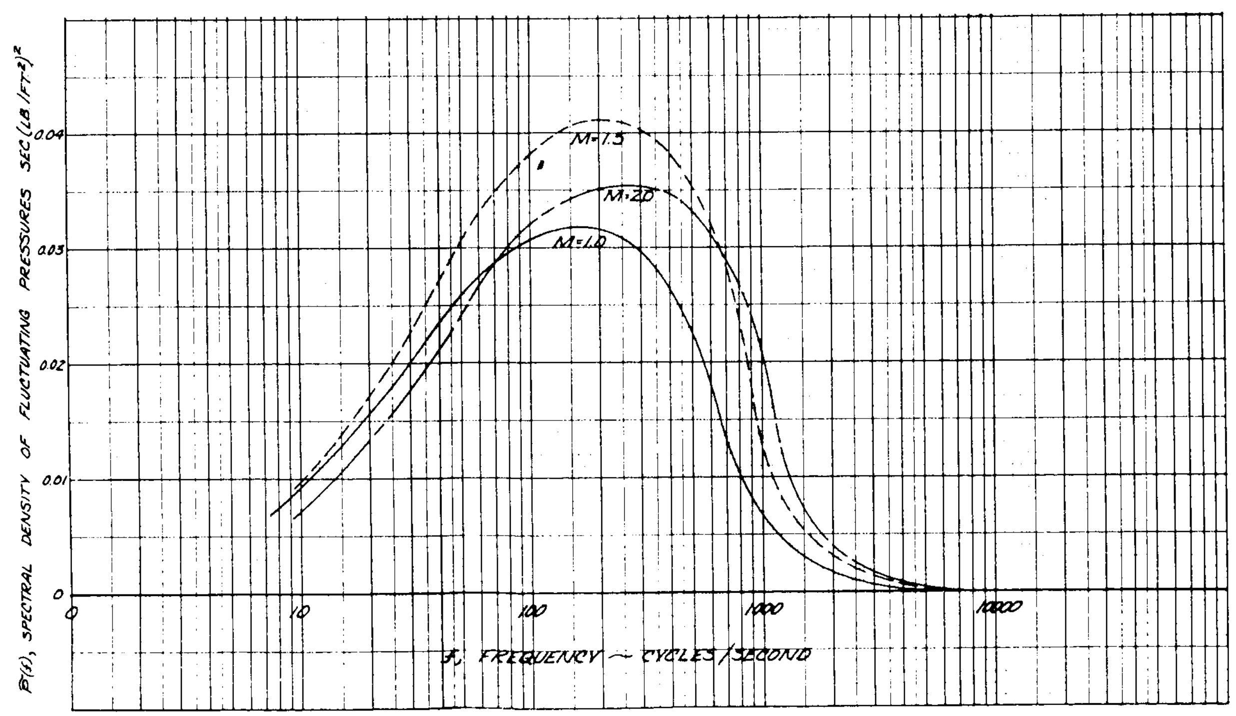

Distance Downstream of Frustrum-Cylinder Joint = 600 In.

NSP 6658

Fig. 5-9 Turbulent Boundary Layer Fluctuating Pressure Spectrum on S-N Stage (RIFT)

Fig. 5-5 (up to 42 sec) by proper scaling. To find the pressure acting at a frequency or in a band in this time range, form the ratio of the squares of the overall pressure (Fig. 5-5) to the pressure at static firing, $(15.4)^2$, and multiply this scaling factor times the square of the pressure level obtained at the desired frequency from Fig. 5-6. The same procedure may be used with Figs. 5-7 and 5-9. In Fig. 5-9, three body stations and Mach numbers are shown; the combination of parameters nearest to the point-of-interest should be the basis for scaling. Pressure levels from two sources at the same frequency may be combined by adding the squares of the r.m.s. pressures shown in the individual spectrums.

The engine spectrum is shown for the worst condition which occurs at the aft skirt; the pressure fluctuations travel along the missile at a velocity equal to the difference between the speed of sound and speed of flight, while the pressure magnitude decreases with the distance squared. The normal shock fluctuations are estimated to act over about 5 longitudinal inches and move aft as the Mach number increases from 0.75 to 0.95. Since this movement cannot be predicted, any point on the skin may be subject to the worst condition noted in Fig. 5-8 for a short time period. Discrete boundary-layer fluctuations move from front to rear at $\approx$ 0.8 times the missile velocity. Individual fluctuations lose their identity in about 4 to 8 feet. Figure 5-9 shows that pressures become relatively larger in the low-frequency ranges as the distance from the nose increases.

For a preliminary estimate, the list of cyclic pressure sources is reduced to the engine noise, oscillating normal shocks, and boundary-layer turbulence. The cyclic pressure level and frequency spectrum in Fig. 5-5 and 5-6 were estimated from an empirical relation for pressure levels in frequency bandwidths at the missile surface (Ref. 29). These values were compared to data for pressures at the nose of the Atlas (Refs. 30 and 31), estimates for the Saturn C-V (Ref. 32), and two experimental correlations (Fig. 70 of Ref. 33).

Sound pressure level at the S-N stage under static firings is given in Fig. 5-10. In all cases, the estimated r.m.s. pressure fluctuations at the aft-end of the S-N stage skirt

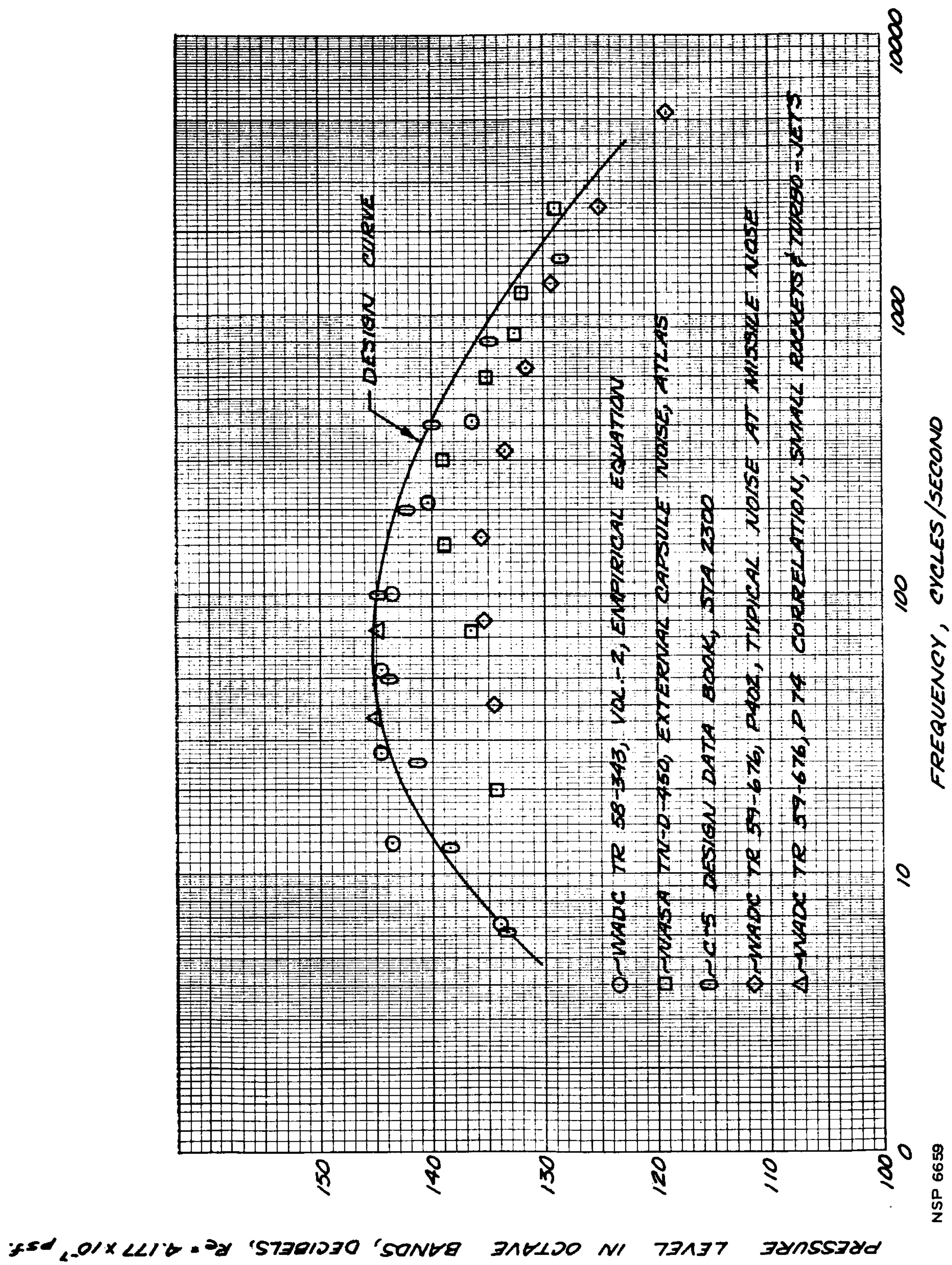

NSP 6659

Fig. 5-10 Sound Pressure Level Spectrum at the S-N Stage (RIFT) Under Static S-IC Firing were approximately 1 to 2 psf higher than referenced information. Data from Atlas and C-1 tests should be applicable on a scaling basis, since the ratios of thrust to the square of the distance to the point-of-interest are similar in magnitude to the configuration. The frequency distribution of pressures given by the empirical equation was modified slightly to provide agreement with peak frequency of the referenced information (Fig. 5-10). This curve was replotted to more useful form in Fig. 5-6. As the vehicle accelerates, the overall pressure-level drops off as a function of $(1-M)^2$ (Refs. 29, 31, and 33), while the spectrum maintains the same shape (Refs. 38 and 39).

Test data are the basis for the rough estimate of the magnitude and frequency distribution of the fluctuating pressures shown for the normal shock phenomena in Figs. 5-5 and 5-8. Note that the data of Fig. 5-8 is rather sketchy; however, no other experimental evidence has been found to support or refute the results.

Pressure fluctuations are characteristic of the turbulent-boundary layer. The literature (Refs. 29, 30, 33, 34, 35, and 36) indicates that the overall rms pressure fluctuation is proportional to the free stream dynamic pressure ($P_{rms} = K q_{\infty}$). Measured values of the constant of proportionality (K) generally fall between 0.0045 and 0.02 with 0.006 being most common (Refs. 35 and 36). In Ref. 35 an extensive literature review was made in an attempt to correlate the frequency distribution associated with boundary-layer fluctuations; these results are shown in Fig. 5-11 along with the data for four individual tests (Refs. 34 and 37). The parameters in the correlation indicated a dependence upon the boundary-layer displacement thickness, free-stream velocity, and dynamic pressure. The suggested design curve shown in Fig. 5-11 was selected to envelop the data points for tests conducted in air. This curve has been replotted in Fig. 5-9 for three body stations and three Mach numbers which bracket the expected maximum dynamic-pressure conditions. (The boundary-layer thickness estimated for a 1/7 power law velocity profile was used to reduce the correlated data.) The predominant trend in the spectrums was the movement of the peak pressure to lower frequencies as distance from the nose increased; the overall pressure (integrated area) remained the same. The level of the r.m.s. pressure fluctuation shown in Fig. 5-5

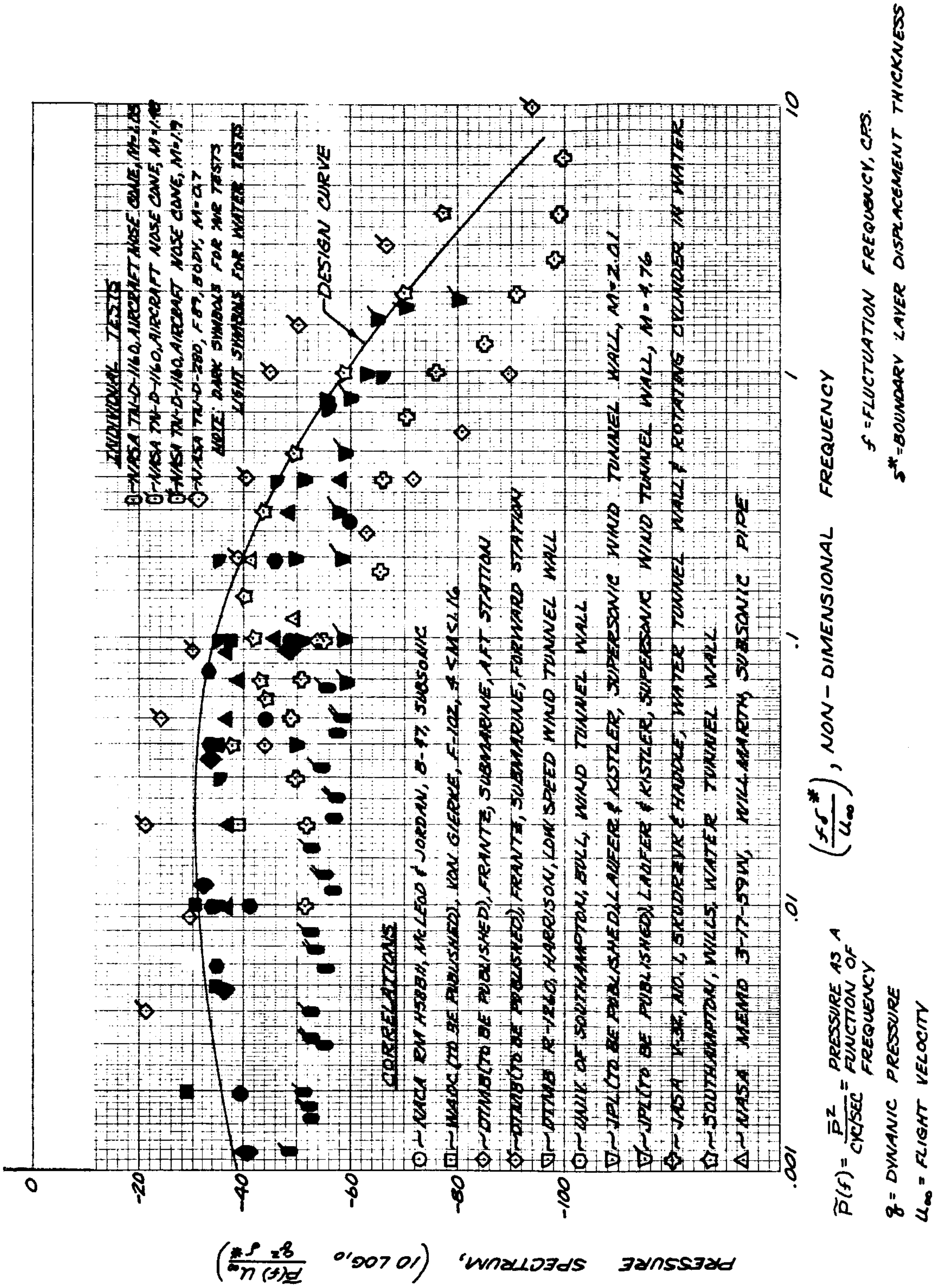

Fig. 5-11 Turbulent Boundary Layer Fluctuating Pressure Correlation

NSP 6660

was obtained by integrating under these curves to establish the empirical proportionality constant of 0.009 in the relation between cyclic pressures and dynamic pressures, $P_{rms} = 0.009\ q_{\infty}$.

5.3 LAUNCH PAD FORCES

Launch pad steady-state drag characteristics are given in Fig. 5-12. Shown in this figure are the distributed cross-force (drag) coefficients, C_{D_c}, for the Saturn VN RIFT and operational vehicles. The integrated drag coefficient value corresponds to test results which measured pad loads on a dynamically scaled model of a large missile at Reynolds numbers per foot up to 7 million. In addition to the steady-state forces, oscillations of the missile in the drag direction may increase the forces by as much as 15 percent (according to Ref. 38).

Transverse forces causing missile oscillations in a plane normal to the velocity vector are random in nature for the Reynolds number range to be experienced by the RIFT vehicle. These transverse forces are of the order-of-magnitude of the steady-state drag forces. A method has been selected for future preliminary estimation of these forces. Accurate determination of these forces then is only possible through testing of dynamically scaled models. Experiments conducted thus far have shown that the transverse forces are extremely sensitive to any external protuberances as well as missile nose contours.

5.4 STAGE VENTING

Preliminary calculations have been made to determine a venting-orifice size on the 20-deg nose fairing. The specific intention of this study was to determine the venting which would alleviate the imposed aerodynamic forces on the structure throughout the first-stage flight and reduce structural weight. The criterion established was that the orifices must provide a pressure differential $(P_{inside} - P_{outside})$ of 2 psid for the entire first-stage flight period. For the study, a conical volume of 27,622 cu ft was used along with a typical operational vehicle trajectory. The resultant total orifice area estimated from this study was 1.6 sq ft. This total area may be distributed around the periphery into a number of smaller orifices (totaling 1.6 sq ft).

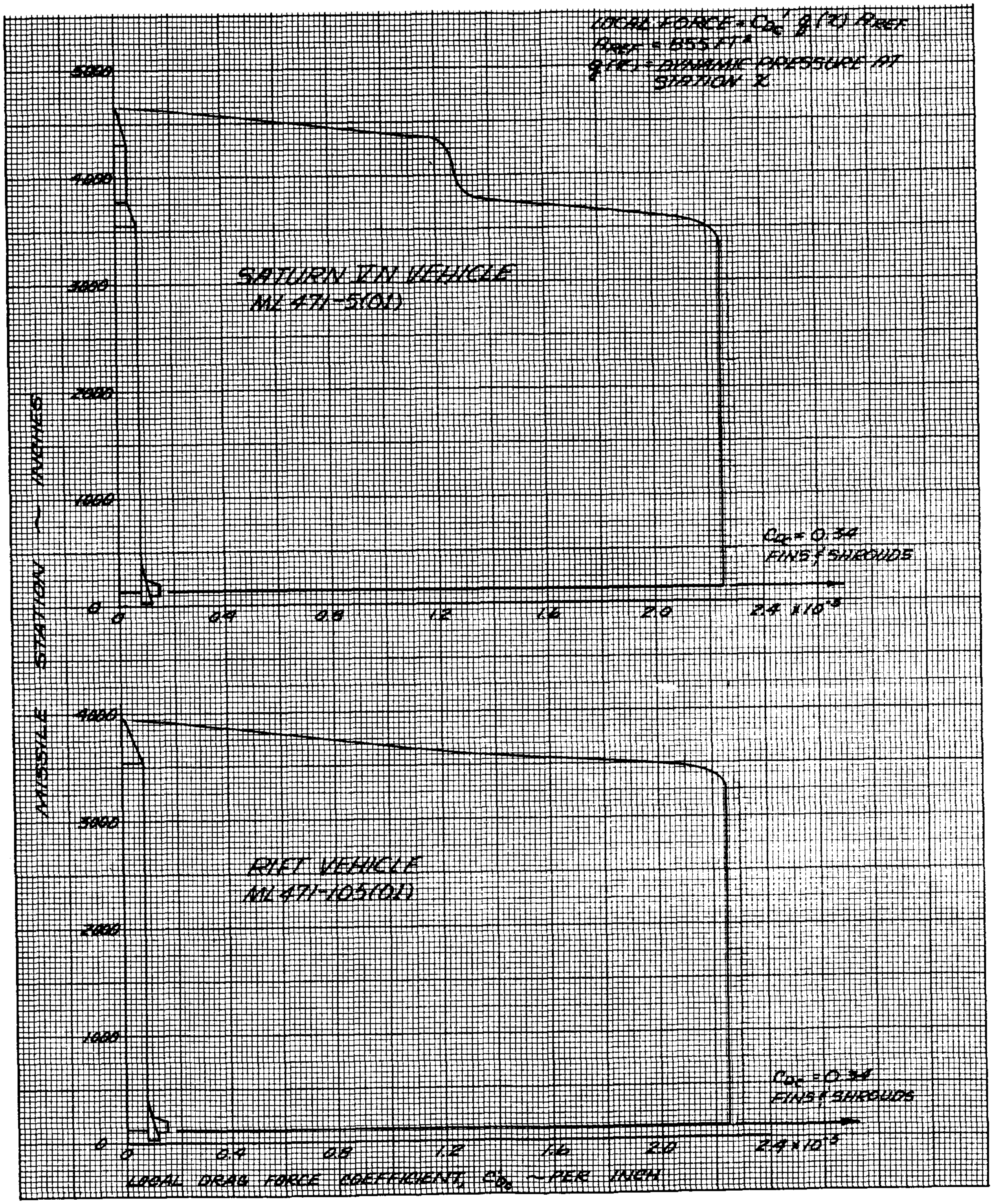

NSP 6661

Fig. 5-12 Saturn VN RIFT and Operational Vehicles Launch Pad Steady-State Drag Coefficient Distributions

Estimates of internal pressure histories were based upon compressible isentropic expressions for orifice flow with heat transfer, as programmed for the IBM 7090 computer. External surface pressures were determined from S-N stage wind-tunnel tests P61. Future studies may be required to determine interstage venting requirements and requirements for venting undesirable boiloff products. Time history of the internal and external venting pressures for this study are presented in Fig. 5-13.

5.5 FLEXIBLE-BODY LIFT DISTRIBUTIONS

Present rough order-of-magnitude analyses of the aerodynamic forces acting on an elastic missile utilize a "quasi-static" approach to determine the lift distribution. This method assumes basically that at any given instant-of-time the body is bending in one of the structural modes. The local incremental lift due to bending is then taken as the product of the rigid-body normal-force coefficient slope/in. times the body deflection angle. That is:

$$\Delta C_{N_{Local}} = C_{N_\alpha}{}' (x)\, \alpha_i$$

where:

$C_{N_\alpha}{}'$ = the rigid-body normal-force coefficient slope per unit length

α_i = $(\partial \delta / \partial x)$ — tangent of body-deflection angle

δ = instantaneous body deflection at station X

This is a simple approach, however, and does not account for aerodynamic damping caused by the body pitching motion and elastic bending motions.

A preliminary study has been initiated to determine the magnitude of these extraneous effects as well as the effects of wind shear and gust environments on the lift distributions. Results are not yet available for publication. The method of approach is based upon the crossflow momentum method as described by Bisplinghoff ("Aeroelasticity"), with added terms to account for body flexibility.

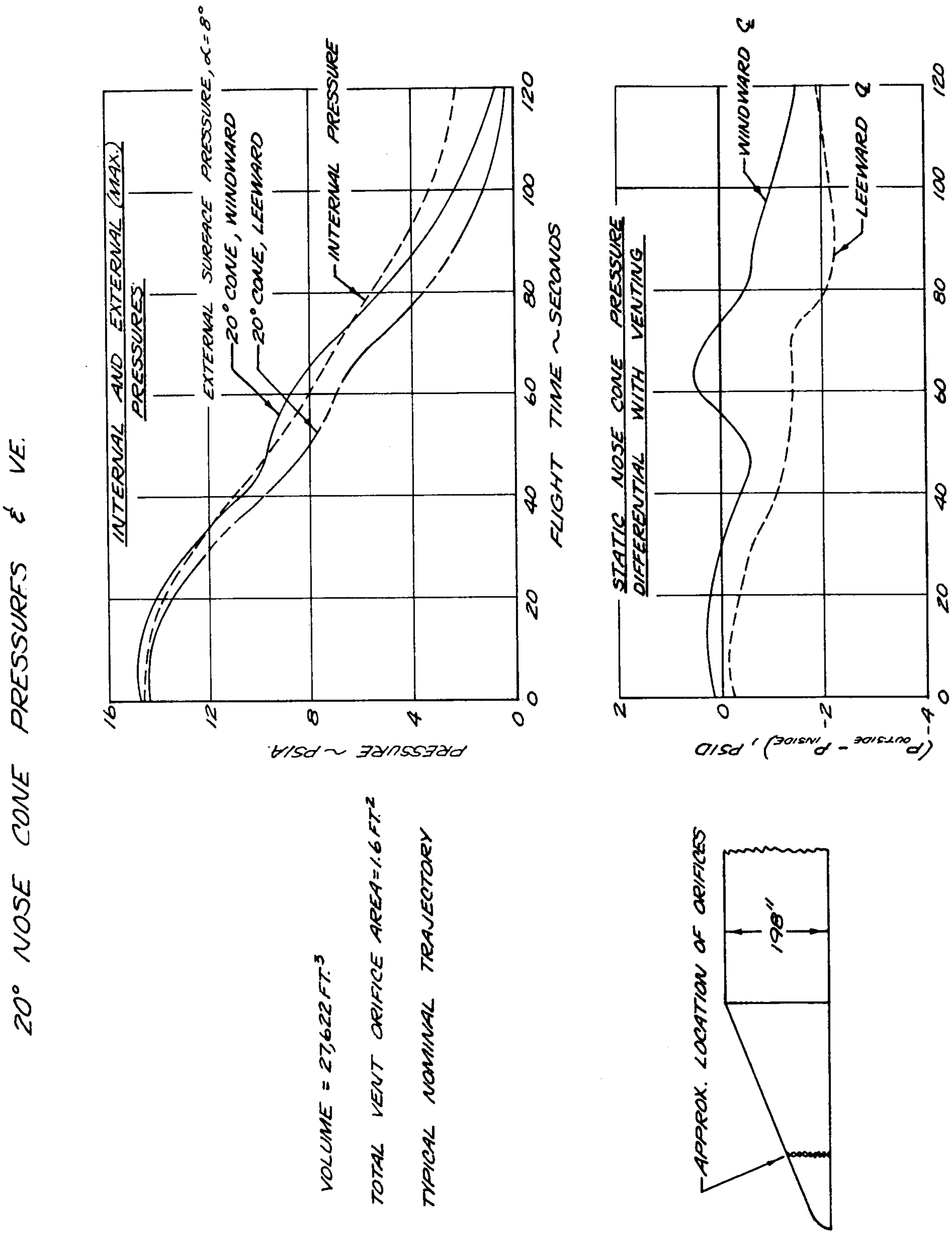

NSP 6662

Fig. 5-13 S-N Stage (RIFT) 20-Degree Nose Fairing Pressures and Venting

Section 6
AERODYNAMICS FOR GROUND TRANSPORTERS

6.1 OVERLAND STAGE TRANSPORTER

Transportation of the S-N stage (Reactor-In-Flight-Test – RIFT) to the test facility will be by a specially designed truck-trailer which will travel overland for a large portion of the trip. The stage will be in a horizontal position and will be subjected to local ground wind environment. Because of the tremendous size of the stage (tank), a cross wind may impose significant drag and lift overturning moments. Preliminary steady-state lift and drag characteristics of the S-N stage have been calculated and are presented in this section.

Since skin friction and pressure drag are predominantly functions of Reynolds numbers (when Mach number $\approx$ 0), the Reynolds number (based on a 33-ft-diameter reference length) versus wind speed are presented in Fig. 6-1. Note that for speeds in excess of four mph, turbulent-flow characteristics exist on the stage. Skin-friction drag was calculated using the method of Schoenherr (design curves in Ref. 16).*

A cross-force (drag) coefficient of 0.7 (based on area = length x diameter) is realistic for Reynolds numbers of 10^7 order-of-magnitude. A launch-pad wind tunnel test of a dynamically scaled large missile has measured a steady-state drag coefficient of 0.5 (based on planform area) at Reynolds numbers of 7×10^6. In Ref. 16 (Fig. 12, p 3-9), a drag coefficient of 0.5 is shown at a Reynolds number of 10^7 for an end plated cylinder. Experiments by Roshko on a cylinder (Ref. 39) produced a value of 0.7 at Reynolds number of 10^7. In discussion with the MSFC analytical aerodynamics group, a value of 0.7 was considered reasonable to include effects of roughness. Utilizing an assumed ground proximity factor of 2.0 (as per Ref. 40), the tank drag coefficient is:

$$C_{D_c} = 0.7 \times 2.0 = 1.4 \text{ (based on planform area)}$$

*See Section 8 for list of references.

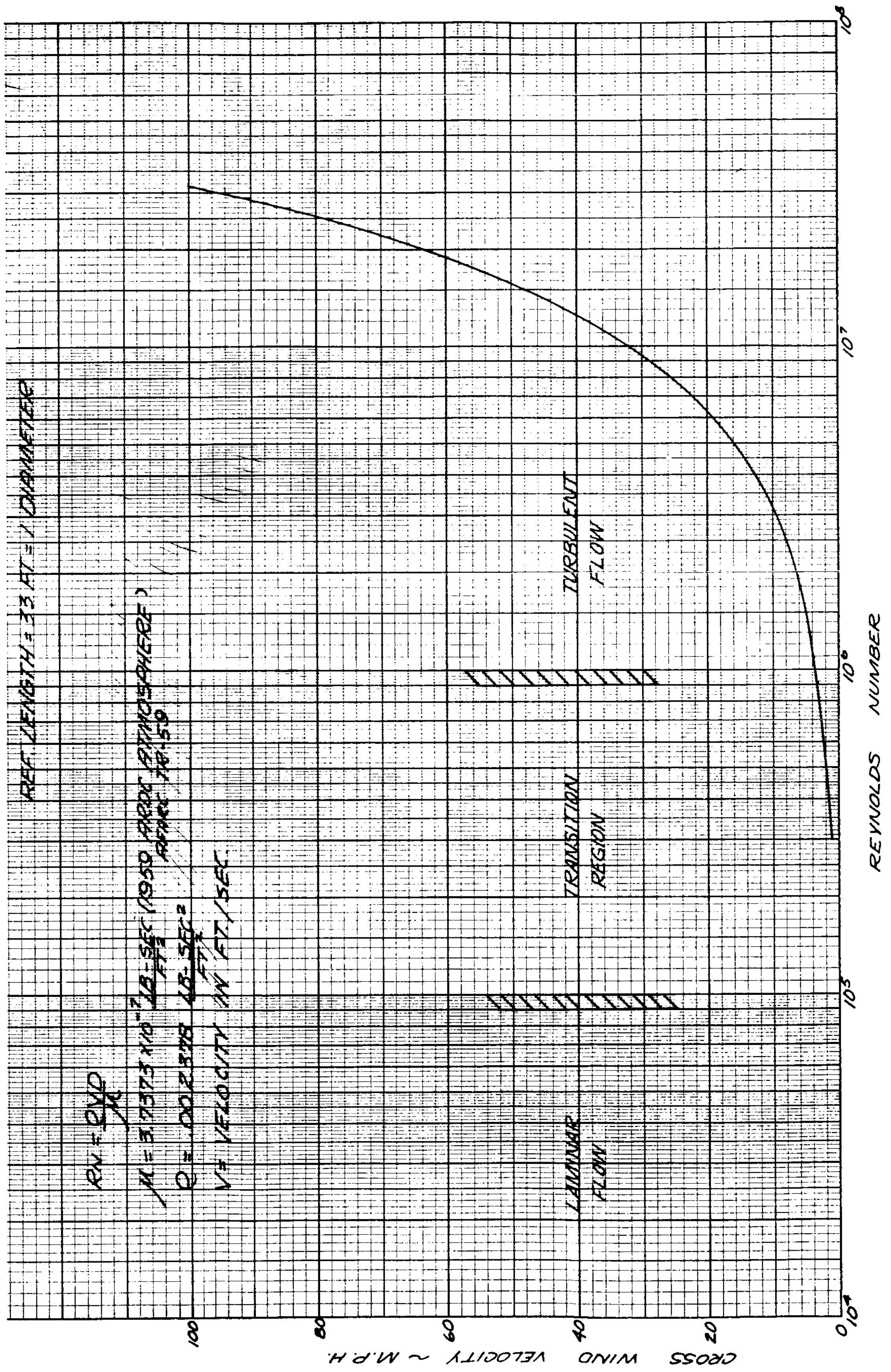

NSP 6663

Fig. 6-1 Reynolds Numbers Relationship to Wind Conditions for Vehicle at Ground Level

Drag due to lift (similar effect on wings) is an assumption included in the ground proximity factor.

Lift coefficient for a sphere in close proximity to the ground is given as 0.4 in Ref. 16 (p. 12−4). A value of lift coefficient for the stage is taken as 0.5. Total drag force and lift force is then calculated according to:

$$\text{DRAG} = 1.4\ (1/2\ \rho\, V^2)\ (L \times D)$$

$$\text{LIFT} = 0.5\ (1/2\ \rho\, V^2)\ (L \times D)$$

where:

L = stage cylindrical length ~ ft
D = stage diameter ~ ft
ρ = sea-level density ~ slugs/ft^3
V = wind velocity ~ ft/sec

In addition to the steady lift and drag forces, oscillatory forces may be induced by the trailing vortex system. At present, means of calculating such effects are unknown, and tests would be required for accurate evaluation.

6.2 ONSITE STAGE TRANSPORTER

Steady-state and oscillatory (transverse) force coefficients have been estimated to facilitate design of the S-N stage onsite transporter used within the test facility. The results show that the oscillatory transverse forces can be of the same order-of-magnitude as the steady-state drag forces. Steady-state drag coefficients distributed along the structure are noted in Fig. 6-2 for the onsite transporter. Integration of this distributed coefficient along the tank will give the total drag coefficient of the stage. The support dolly structure (Fig. 6-3) coefficients are shown in Fig. 6-2 as concentrated forces for ease in computation. Local drag is calculated according to:

$$\text{LOCAL DRAG} = C_{D_c}\ q(x)\ A_{ref} \sim \text{lb/in.}$$

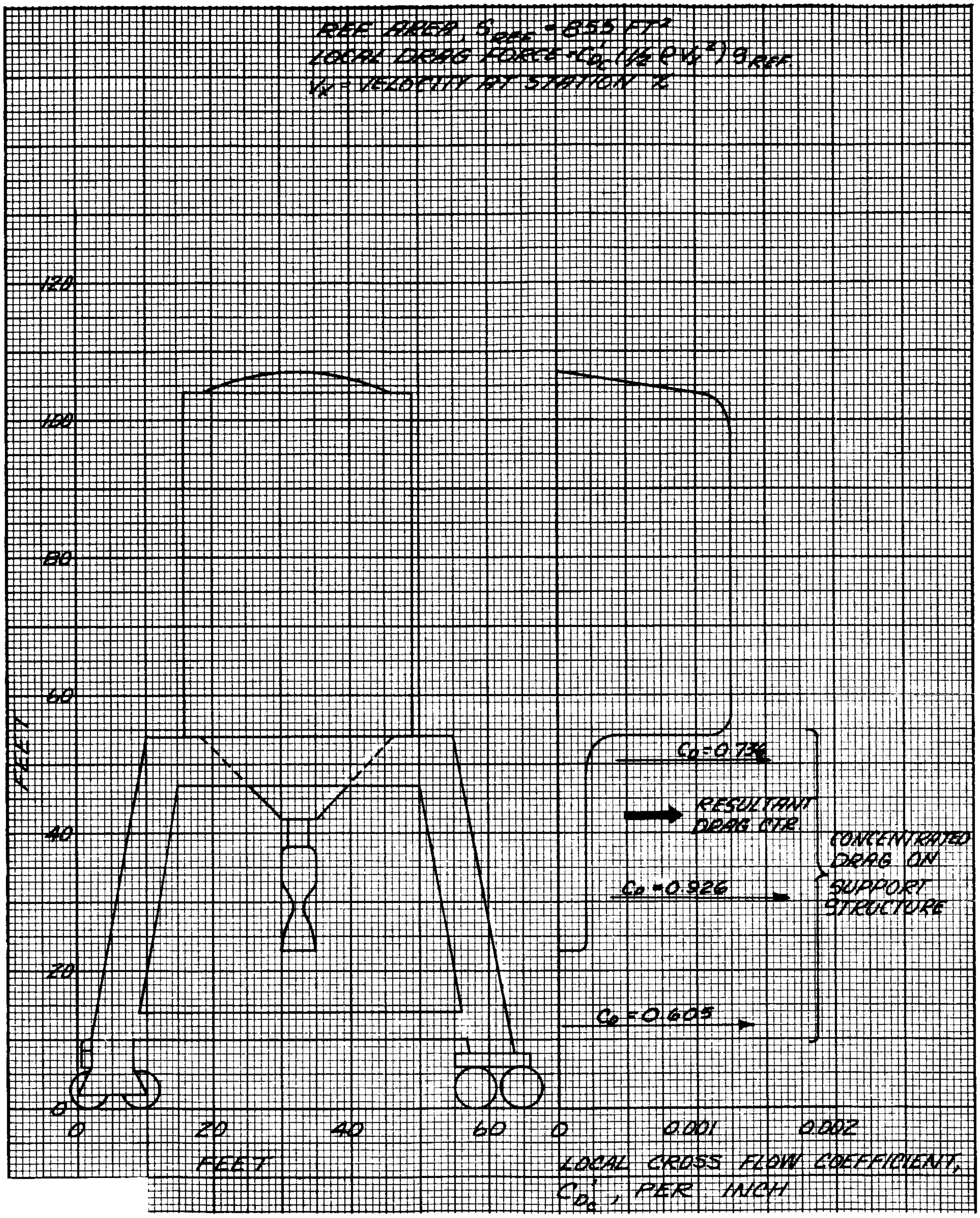

NSP 6664

Fig. 6-2 Steady-State Drag Coefficients Distribution for Onsite Transporter

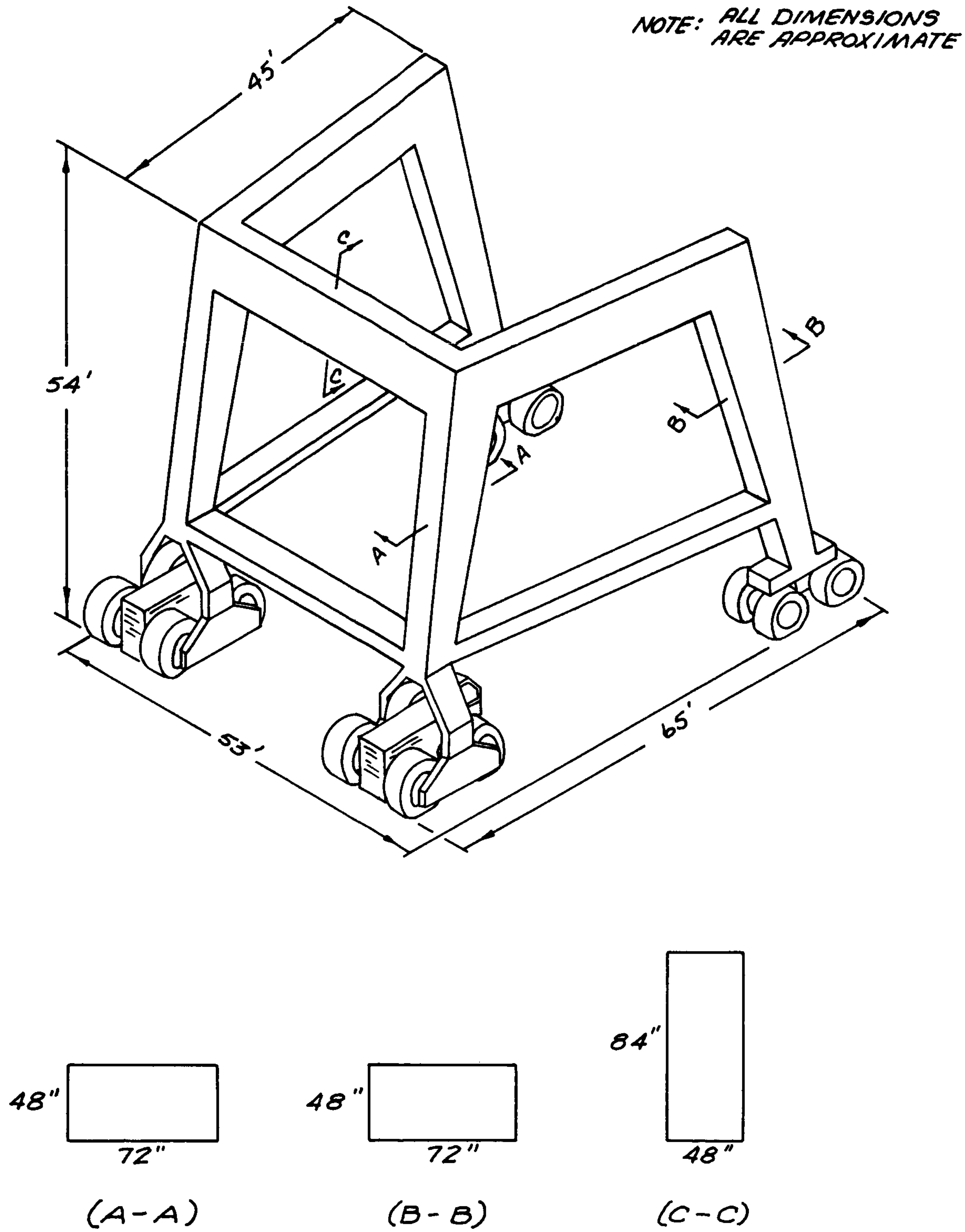

NSP 6665

Fig. 6-3 Detailed Coefficient Distribution for Onsite Transporter where:

$q(x)$ = dynamic pressure at station (x), (99.9% wind)

A_{ref} = 855 ft^2

For the S-N stage, a drag coefficient of 0.7 (based on planform area) was adjusted to compensate for end effects utilizing a fineness ratio drag factor (η) of 0.56 as per Ref. 41. These results are applicable for Reynolds numbers 5.0×10^6 (at 30 mph the Reynolds number is 9.3×10^6). A flat-plate drag coefficient of 2.0 (Ref. 16) was utilized for the tank supporting structure.

Distributed oscillatory lift-force coefficients acting in a plane transverse to the flow direction are presented in Fig. 6-4. The oscillatory transverse forces are random with time; therefore, these forces are treated in the frequency domain utilizing power spectral density representation of the random lifting forces. The method described in Ref. 42 was utilized for estimating these unsteady forces. Distributions of the oscillatory lift coefficients (Fig. 6-4) are presented for a 99.9 percent wind profile (Fig. 6-5), and for frequencies of 0.25, 0.50, and 1.0 cps. Phase relations between the structure oscillation and the aerodynamic force are unknown.

The results presented here are preliminary in nature and are representative of current methods in handling unsteady transverse forces on upright structures. The steady-state drag coefficient results presented are independent of ground wind profiles, whereas the oscillatory lift coefficients are dependent upon wind profiles. These oscillatory lift coefficients are used in calculations of the vehicle structural dynamics.

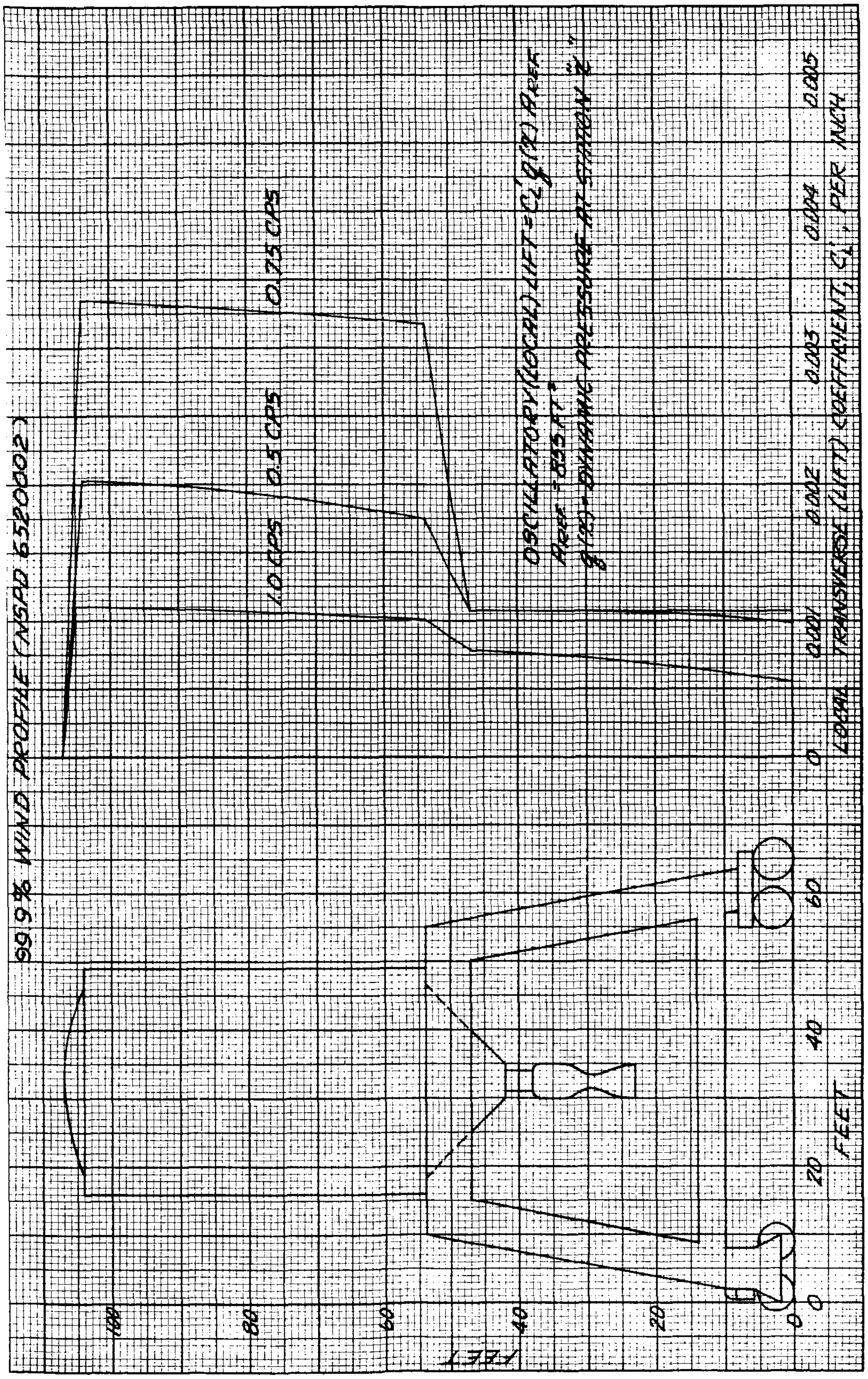

NSP 6666

Fig. 6-4 Transverse Oscillatory Lift Force Coefficients Distribution for Onsite Transporter

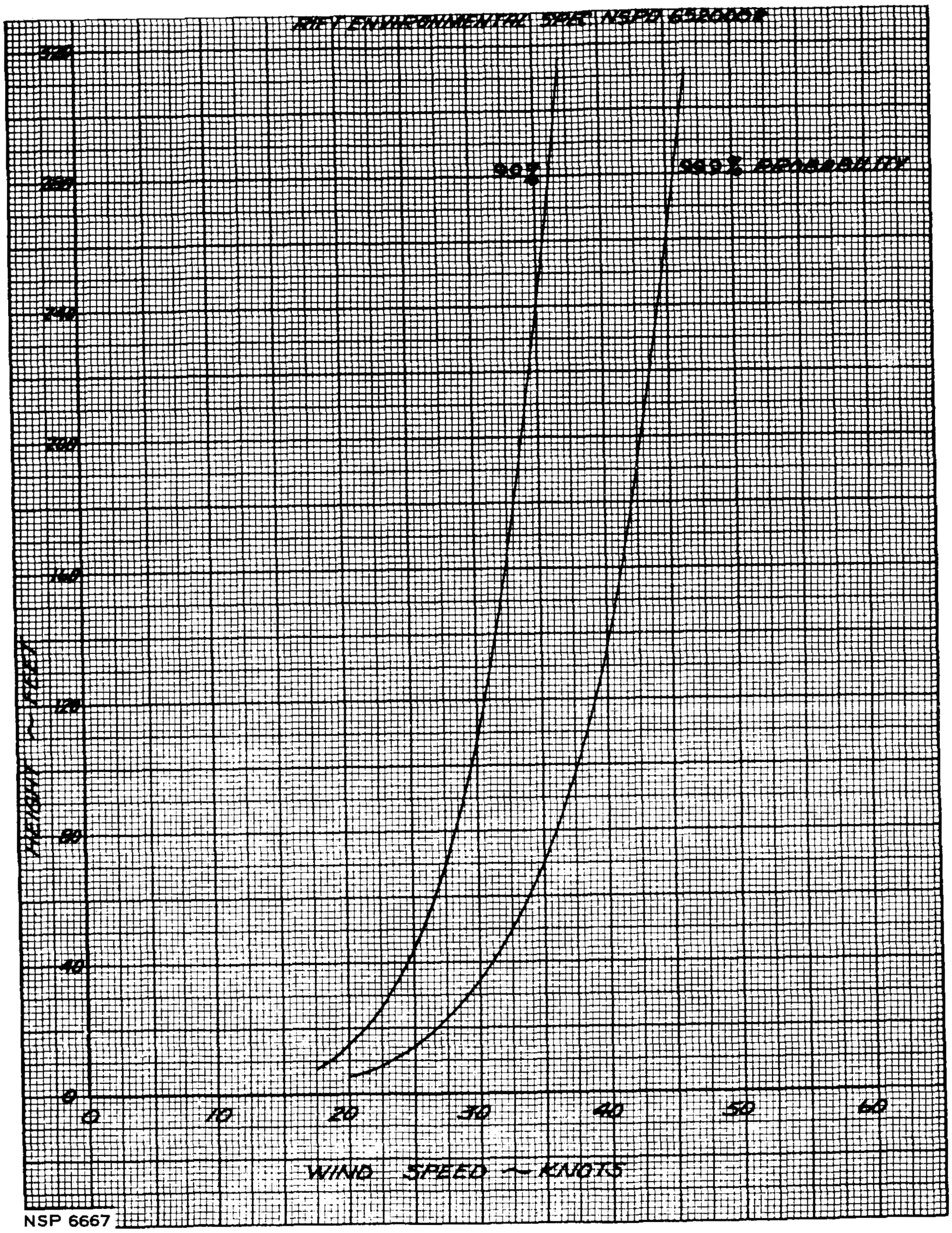

Fig. 6-5 Ground Wind Speed Profiles Under Steady-State Conditions

Section 7
ROCKET PLUME INVESTIGATIONS

7.1 ATTITUDE CONTROL MOTOR WAKE CHARACTERISTICS

The jet wake from the attitude control jets has been determined for two operating conditions: (1) 28 psia chamber pressure and 250°R chamber temperature and (2) 16 psia chamber pressure and 38°R chamber temperature. These plume characteristics are being used as a guide to the placement of the control system. Figure 7-1 presents lines of constant Mach number and Fig. 7-2 lines of constant flow angle for the high pressure case. Figures 7-3 and 7-4 present similar data for the low pressure case. In each case, the ratio of specific heats is assumed to remain constant at the value in the chamber throughout the expansion.

In these calculations, the hydrogen is assumed to act as an ideal gas. Because of the low temperature in the chamber, this assumption is not completely true throughout the jet wake. If the gas temperature and pressure fall below the condensation limit, the gas may liquify or become solid. However, some degree of supercooling may be expected to exist. Tests of steam turbines indicate that steam can be cooled approximately 25 percent below the condensation limit before appreciable flow changes occur. For air, tests in hypersonic wind tunnels show a maximum cooling of 55 or 60 percent below the condensation limit. The actual amount of supercooling that can exist in hydrogen is unknown. It is assumed in this study that hydrogen can be supercooled to a maximum value of 50 percent of the condensation limit. Figure 7-5 presents the vapor pressure curve of hydrogen versus temperature and also the isentropic expansion curves for hydrogen for the two cases being considered. As indicated in Fig. 7-1, for the high pressure case, condensation will start at approximately Mach number of 7.5 and is supercooled 50 percent by Mach number of 10.5. In the low pressure case, 50 percent supercooling occurs at a temperature of 19°R which corresponds to condensation in the

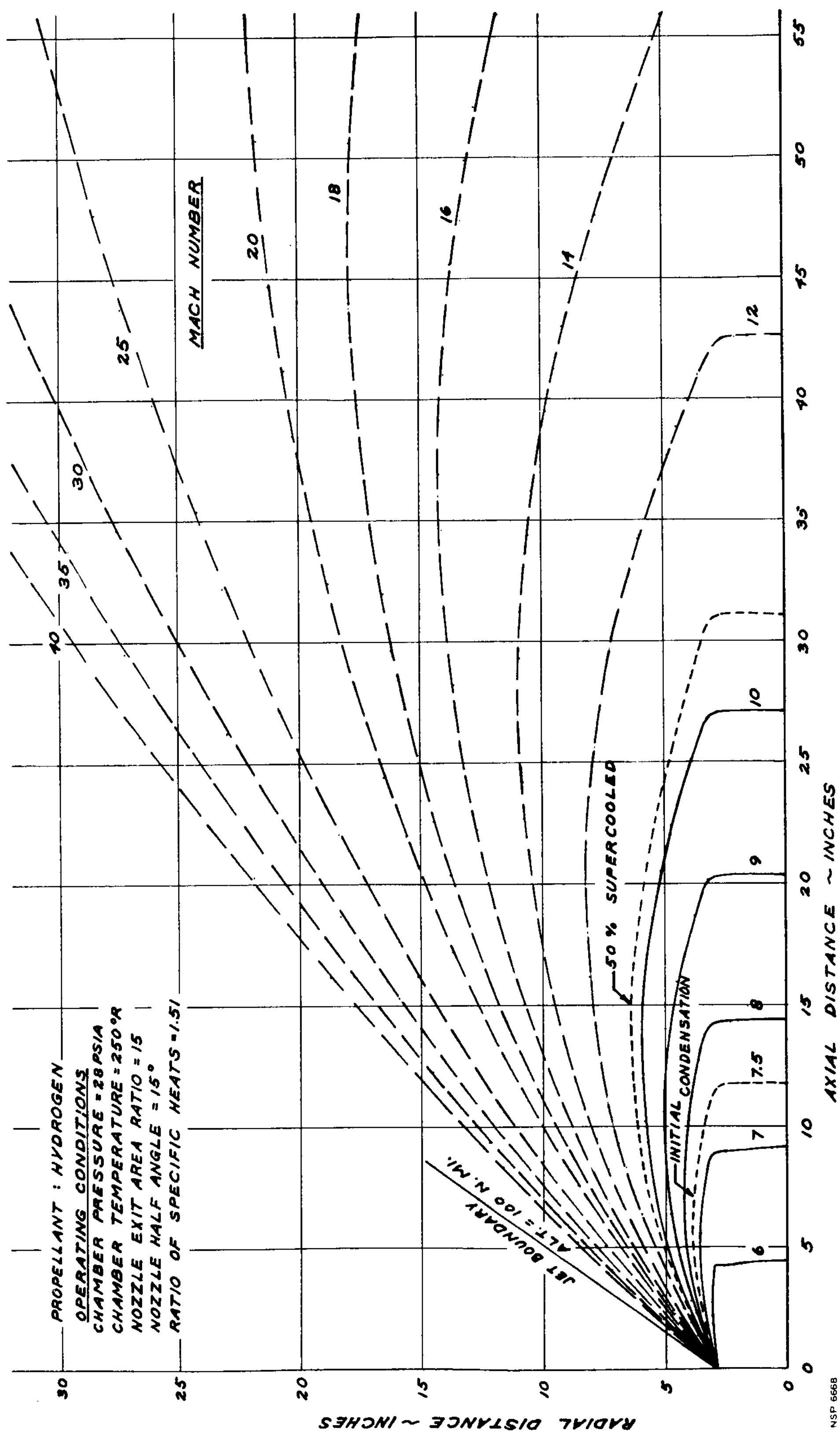

Fig. 7-1 RIFT Attitude Control Motor Set Wake With Constant Mach Number Contours at High Pressure

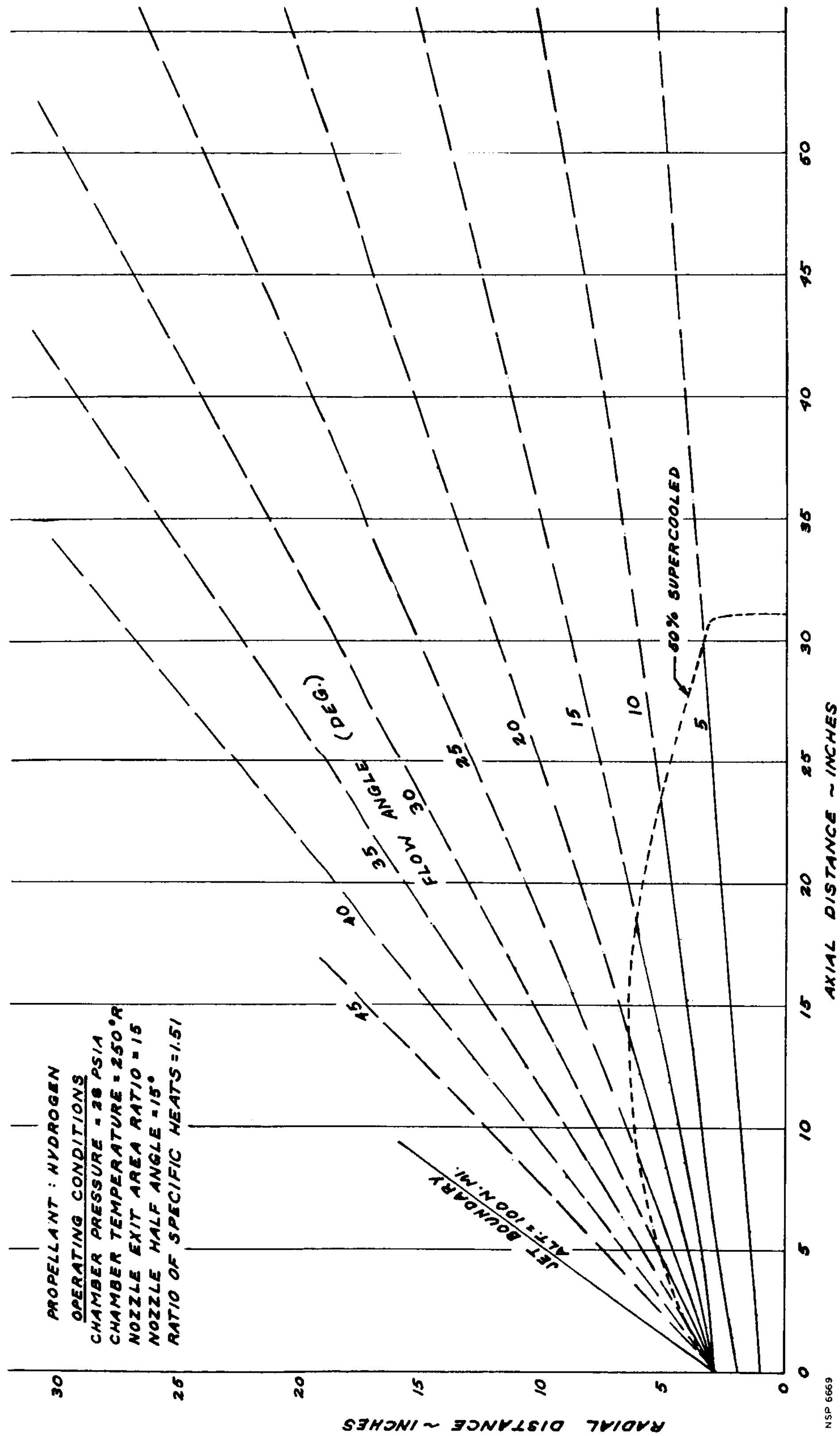

Fig. 7-2 RIFT Attitude Control Motor Set Wake With Constant Flow Angle Contours at High Pressure

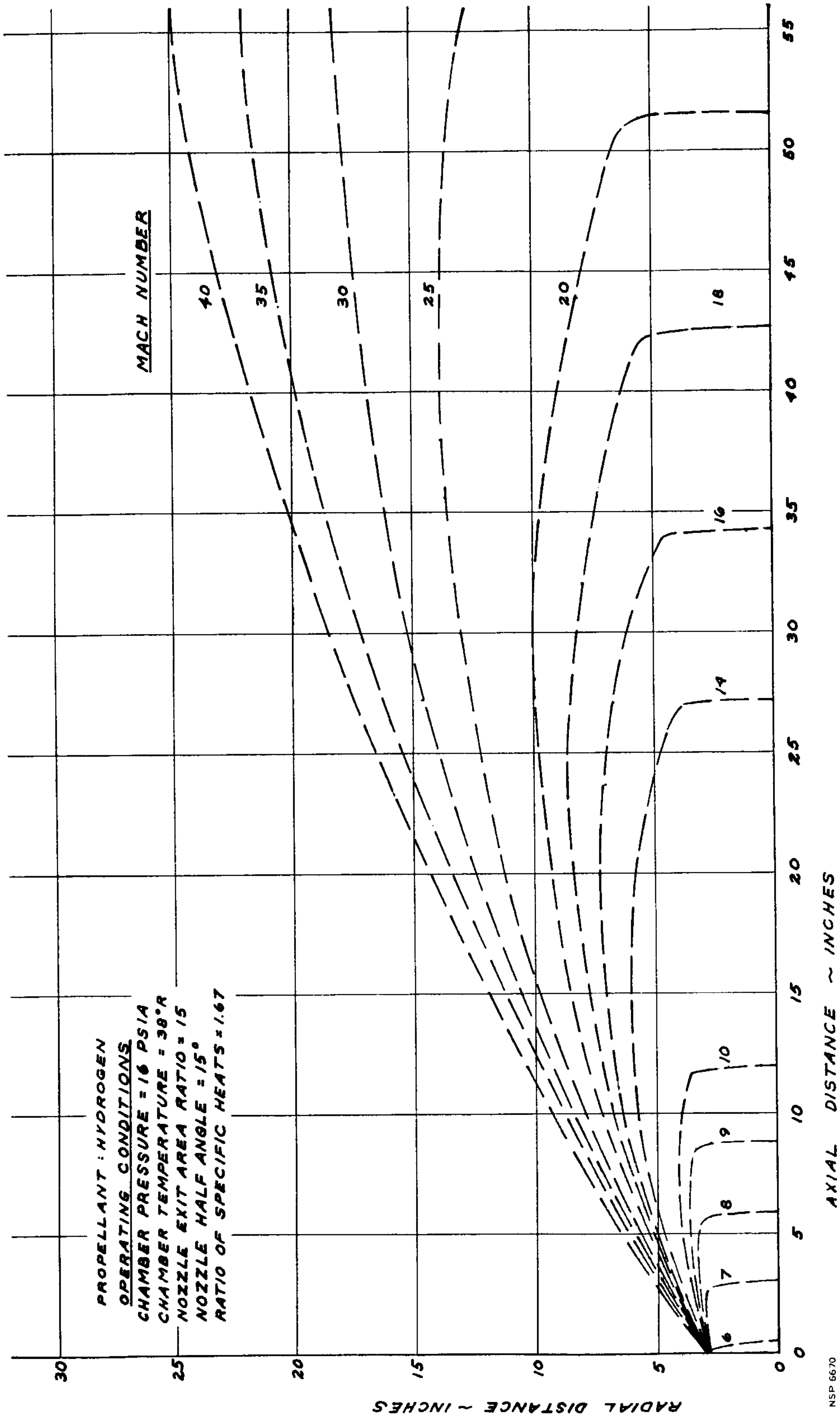

Fig. 7-3 RIFT Attitude Control Motor Set Wake With Constant Mach Number Contours at Low Pressure

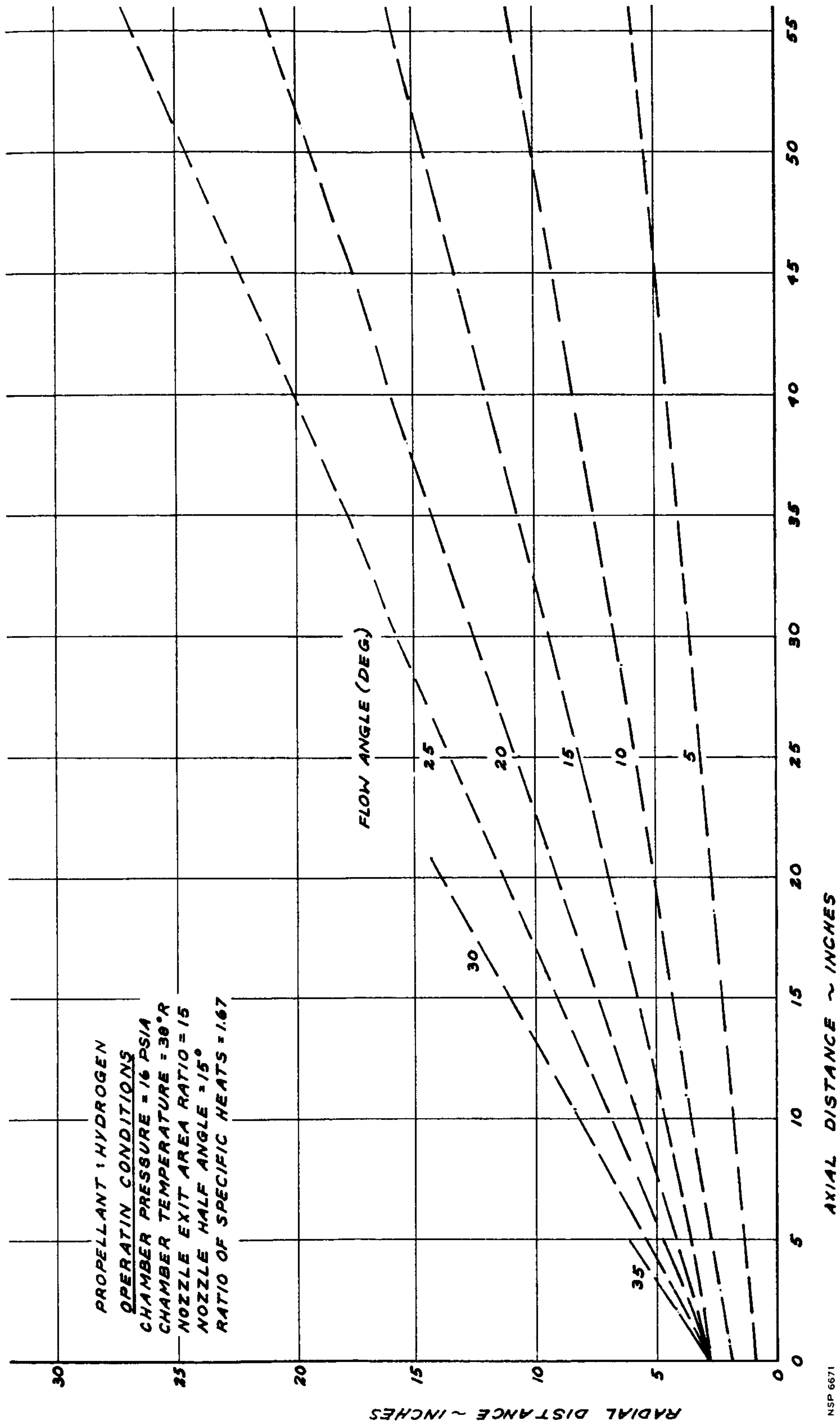

Fig. 7-4 RIFT Attitude Control Motor Set Wake With Constant Flow Angle Contours at Low Pressure

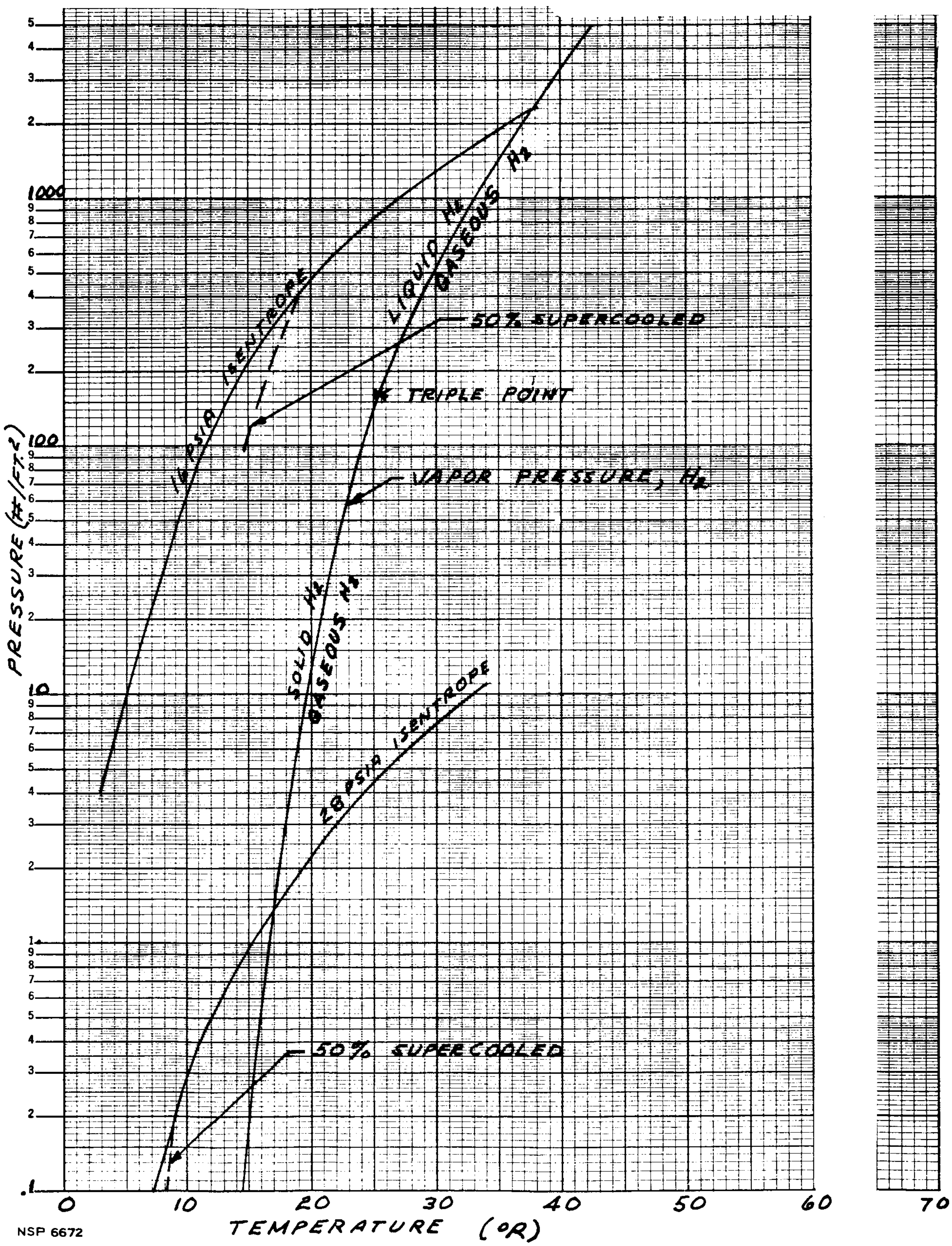

Fig. 7-5 RIFT Attitude Control Motor Hydrogen Gas Condensation Limits

nozzle at an area ratio of about 1.30. In this case, the jet wake presented is hypothetical and may not exist at all in a gaseous state. In either case, the jet wake presented is invalid once appreciable condensation occurs.

7.2 INTERSTAGE RETROROCKET IMPINGEMENT

A limited investigation was conducted to determine possible methods of mounting the retrorockets. Investigation of the effective angle of the retrorockets required for satisfactory separation shows that the resultant thrust of these rockets should be at an angle of 14.8 deg with respect to the centerline of the S-N stage (subsequent to this study, this angle has been revised to 14.4 deg).

Of the several ways of mounting these motors internally, the best way seems to be as shown in Fig. 7-6 with the motor mounted parallel to the vehicle centerline and a deflector surface shaped so as to produce the required thrust angle. This study is preliminary and is intended only to investigate the feasibility of the design. Therefore, this investigation does not determine optimum deflector shape or the optimum mounting depth of the retro motor but only the forces produced by a selected deflector shape and motor mounting.

Figure 7-7 shows the effect of varying the length of the deflector. A deflector having a length of 55 in. is required to produce the desired 14.8-deg thrust angle.

An alternate method of installation that was investigated consists of using a blast tube of circular crosssection with a diameter equal to the nozzle exit diameter connecting the motor to the surface. In this case, as the angle of the nozzle is reduced, the normal force caused by the bevel of the blast tube increases. Calculations show the minimum effective thrust angle is 41.5 deg with the motor nozzle canted 20 deg. Since this angle is much greater than desired, this method is not useable in this case.

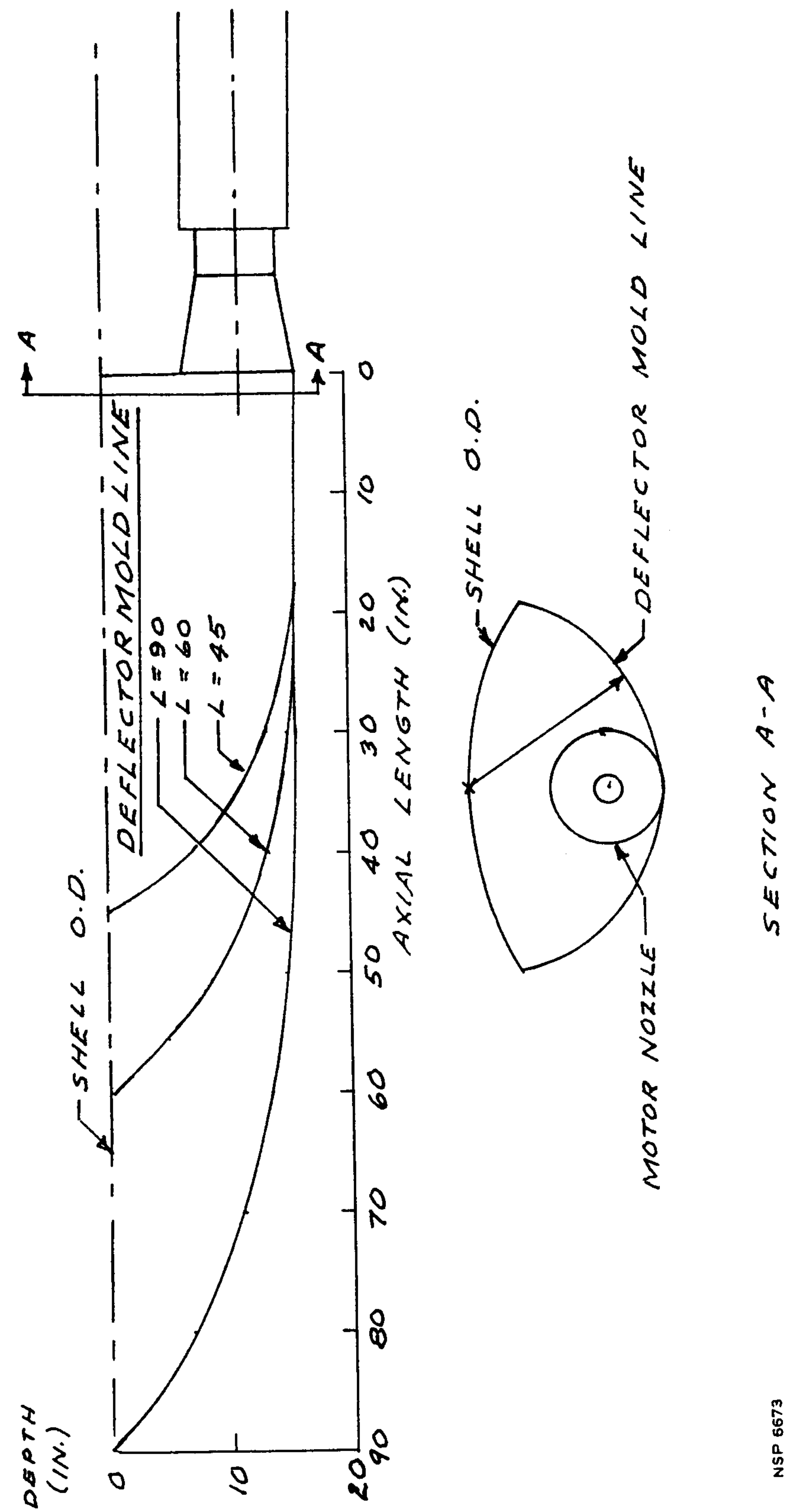

Fig. 7-6 Retrorocket Installation on Interstage

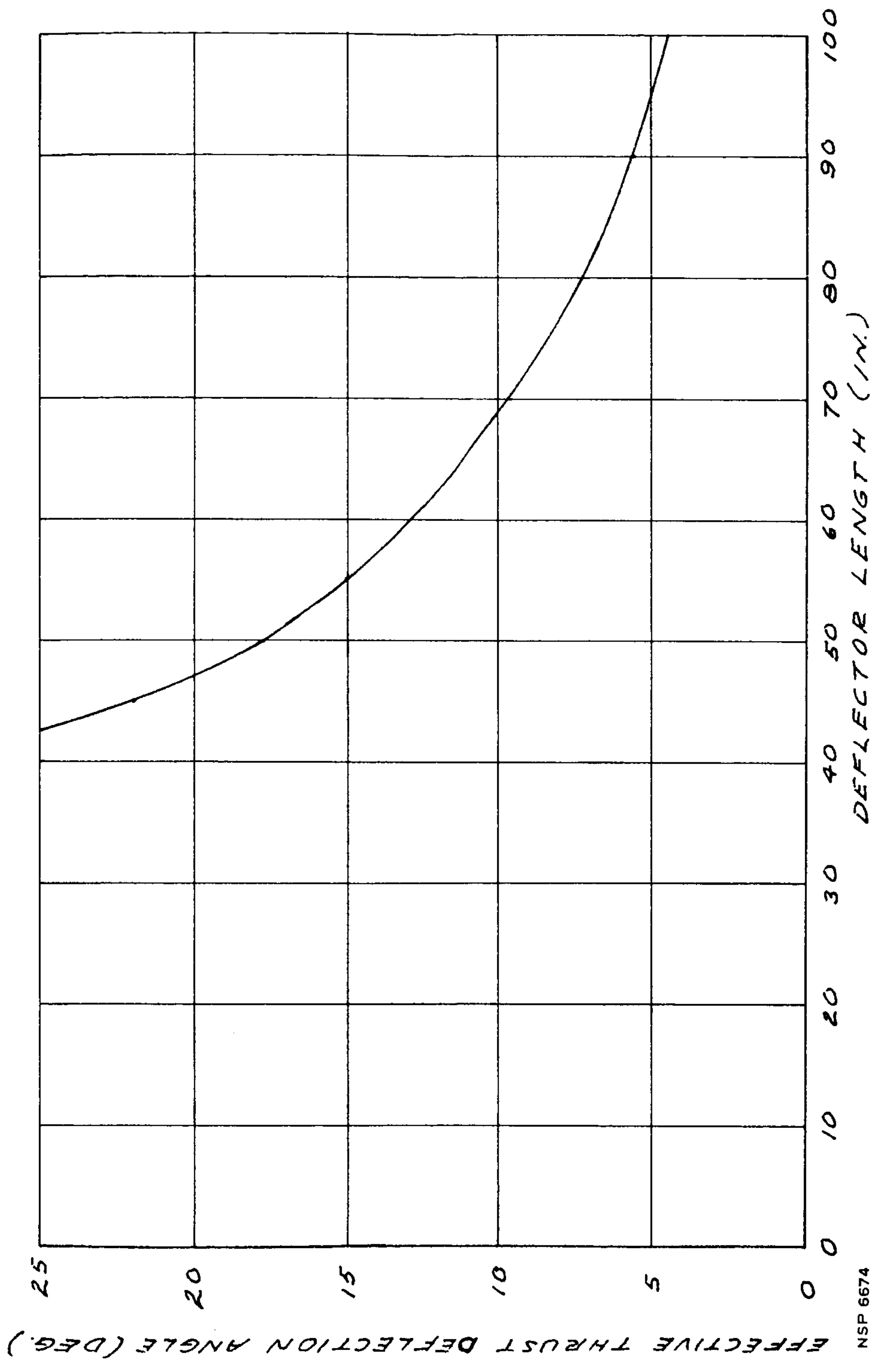

Fig. 7-7 Retrorocket Effective Thrust Deflection Angle versus Reflector Length

Section 8
REFERENCES

1. "Preliminary Test Results from P-41 Pressure Tests of the Saturn C-5 at Ames Unitary Wind-Tunnel," 28 Dec 1962
2. Air Load Manual, Saturn C-5 Three Stage to Escape (LOR), 1 Oct 1962
3. MSFC-M-AERO-E-158-63, "Presentation of Basic Data from Supersonic Wind Tunnel Investigation of Static Longitudinal Stability and Axial Force Characteristics of the Saturn V Chemical, RIFT, and Nuclear Vehicles (MSFC Project P-34)," 16 May 1963
4. MSFC-M-AERO-E-86-63, "Presentation of Basic Data from Transonic Wind Tunnel Investigations of Static Longitudinal Stability and Axial Force Characteristics of the Saturn V Chemical, RIFT, and Nuclear Vehicles (MSFC Project P-34)," 26 Feb 1963
5. GT. BRIT. RAE AERO TN-2621, "Wind Tunnel Measurements of Normal Force and Pitching Moment on Four Cone Cylinder Combinations at Transonic and Supersonic Speeds," by E. Huntley, B. SC., May 1959
6. NACA RM A50L07, "Characteristics of Flow Over Inclined Bodies of Revolution," by H. Julian Allen and Edward W. Perkins, 5 Mar 1951
7. NACA RM L51J09, "An Investigation of the Aerodynamic Characteristics of a Series of Cone-Cylinder Configurations at a Mach Number of 6.86," by Ralph D. Cooper and Raymond A. Robinson, 17 Dec 1951
8. MPT-AERO-61-38, "Aerodynamic Characteristics of Spherically Blunted Cones at Mach Numbers from 0.5 to 5.0," 11 Dec 1962, (U)
9. AEDC-TDR-62-166, "Hypersonic Static Stability of Blunt Slender Cones," by Jack D. Whitfield and W. Wolny, Aug 1962, (U)

10. NACA TR-921, "Theoretical Symmetric Span Loading at Subsonic Speeds for Wings Having Arbitrary Planform," by John DeYoung and D. W. Harper, 1948

11. ATS/60-159, "Stability and Control Manual," by D. C. Olsen

12. "Engineering Supersonic Aerodynamics," by E. A. Bonney, 1950

13. NACA RM A53G08, "A Method for Calculating the Lift and Center-of-Pressure of Wind-Body Tail Combinations at Subsonic and Supersonic Speeds," by J. N. Nielson, G. E. Kaatari, and R. T. Anastasio, 12 Nov 1953

14. Boeing D5-11245, "Final Data Report Saturn V-RIFT Wind Tunnel Pressure Test P-61," 16 Nov 1962

15. LMSC/448514-1, Appendix C, "Free Molecule Flow Theory and Its Application to the Determination of Aerodynamic Forces," by Lee H. Sentman, 1 Oct 1961

16. "Fluid Dynamic Drag," by Dr. Ing S. F. Hoerner, 1958

17. Journal of the Aeronautical Sciences, Vol. 18, No. 3, "Turbulent Boundary Layer in Compressible Fluids," by E. R. Van Driest, Mar 1951

18. Jet Propulsion, "Estimate of Slip Effect on Compressible Laminar-Boundary-Layer Skin Friction," by H. Mirels, Oct 1958

19. MSFC M-AERO-A-92-62, Aerodynamic Design Section M-AERO-AA, "Estimation of the Preliminary Aerodynamic Characteristics of the Saturn C-5, RIFT Vehicle," 16 Nov 1962

20. NACA RM E54L14, "Wind Tunnel Investigation at Mach 1.9 of Multijet-Missile Base Pressures," by Eugene Baughman, 3 Mar 1955

21. MSFC-M-AERO-A-92-62, "Protuberances on Rocket Vehicles," 8 Aug 1962

22. NASA RN D-793, "Aerodynamic Characteristics in Pitch and Sideslip of a 1/15-Scale Model of the Scout Vehicle at a Mach Number of 2.01," R. B. Robinson, May 1961

23. NASA TN D-794, "Transonic Wind-Tunnel Investigation of the Static Longitudinal Aerodynamic Characteristics of Several Configurations of the Scout Vehicle and of a Number of Related Models," by T. C. Kelley, May 1961

24. MSFC-M-AERO-E-185-62, "Presentation of Basic Data from Transonic Wind Tunnel Investigation of Static Longitudinal Stability Characteristics of a 1.75% Scale Model of the Saturn C-1 Block II Vehicle at Angles of Attack up to 25°," 7 Nov 1962

25. NASA TN-711, "Investigation of the Static Longitudinal and Lateral Stability Characteristics of a 0.10 Scale Model of a Three-Stage Configuration of the Scout Research Vehicle at Mach Numbers of 2.29, 2.96, 3.96, and 4.65," by L. S. Jernell, Mar 1961

26. Boeing D5-11230, "C-5 Wind Tunnel Pressure Test No. P-43 Final Data Release," 11 Dec 1962

27. Boeing Aero-H-152, "Preliminary Data Release Saturn V – RIFT Test P-61," 28 Mar 1963

28. NASA TR-1328, "A Second-Order Shock Expansion Method Applicable to Bodies of Revolution Near Zero Lift," by C. H. Syvertson

29. WADC-TR-58-343, Vol II, "Methods of Space Vehicle Noise Prediction," 1958

30. NASA TN D-997, "In-Flight Noise Measurements for Three Project Mercury Vehicles," by W. H. Mayes, D. A. Hilton, and C. A. Hardesty, Jan 1962

31. NASA TN D-450, "Noise Considerations for Manned Re-entry Vehicles," by D. A. Hilton, W. H. Mayes, and H. H. Hubbard, Sep 1960

32. M-P & VE-VA-226, "C-5 Launch Vehicle Design Data Document," 18 Dec 1962

33. WADC-TR-676, "University of Minnesota Conference of Acoustical Fatigue," Edited by W. J. Trapp and D. M. Forney, Jr., Mar 1961

34. NASA TN D-280, "Flight Measurement of Wall-Pressure Fluctuations and Boundary-Layer Turbulence," by H. R. Mull and J. S. Algranti, Oct 1960

35. GT. BRIT. USAA 131, "Boundary Layer Noise Research in the U. S. A. and Canada; A critical Review," by E. J. Richards, J. R. Bull, and J. L. Willis, Feb 1960

36. NASA MEMO 3-17-59W, "Space-Time Correlations and Spectra of Wall Pressure in a Turbulent Boundary Layer," by W. W. Willmarth, Mar 1959

37. NASA TN D-1160, "Flight-Determined Aerodynamic Noise Environment of an Airplane Nose Cone up to a Mach Number of 2," by N. J. McLead, Mar 1962

38. American Rocket Society Paper, "Design Criteria for Space Vehicles to Resist Wind Induced Oscillations," by A. A. Ezra and S. Birmbaum of Martin Co., Denver, Colorado, Apr 1960

39. Journal of Fluid Mechanics, "Experiments of the Flow Past a Circular Cylinder at Very High Reynolds Numbers," by A. Rashko, May 1961

40. LMSC/926036, "Design Study Overland Transporter for RIFT Stages," by T. T. Drahos and S. Berman, Dept 69-41, 1 Apr 1963

41. NACA TN 2960, "Drag of Circular Cylinders for a Wide Range of Reynolds Numbers," by Forrest E. Gowen and Edward W. Perkins, Jun 1953

42. AFCRL 62-273 (I), Proceedings of the National Symposium on Winds for Aerospace Vehicle Design, Vol. I, "Random Excitation of Missiles Due to Winds," by J. D. Wood and J. G. Berry, Mar 1962

43. NACA TR 1135, "Equations, Tables, and Charts for Compressible Flow," by the Ames Research Staff, 1953

DISTRIBUTION LIST

1	M-P&VE-N	Col. W. S. Fellows*
1	M-P&VE-N	W. A. Brooksbank
5	M-P&VE-NS	D. B. Gardiner
	M-P&VE-NE	A. D. Smith
	M-P&VE-NH	G. A. Keller
	M-P&VE-NI	F. J. Magliato
	M-P&VE-NC	J. F. Wood
	M-P&VE-NT	R. C. Brouns
	M-P&VE-NR	A. H. Nordstrom
	M-P&C-SSR	G. Ridgeway*
	M-FIN-P	J. E. Sharkey
1	M-MS-IP	MSFC Tech. Pub. Section
8	M-MS-IPL	MSFC Tech. Library
7	M-AERO-PS	H. Ledford
1	M-AERO-F	M. A. Horst
	M-AERO-G	C. K. Hill
	M-P&VE-PC	R. D. Sanders
1	M-P&VE-VC	L. Lawson
1	M-P&VE-REL	Heathcock
2	M-P&VE-FN	Manning
	M-P&VE-FN	Harris
	M-P&VE-FN	Austin
	M-P&VE-FN	Whiton
	M-P&VE-FN	Nixon
1	M-P&VE-FS	Orillion
3	M-P&VE-S	J. H. Furman
1	M-P&VE-M	L. K. Zoller
1	M-P&VE-EA	Rendall
1	M-P&VE-EL	Dotson
	M-P&VE-EF	W. Kistler
	M-P&VE-EG	M. Beck
	M-P&VE-ES	Hoffman
1	M-P&VE-EE	Devenish
	M-P&VE-EE	McDaniel
	M-P&VE-EE	Anderson
	M-P&VE-EE	McCullough
	M-P&VE-EE	Graham
	M-P&VE-EE	Williams
1	M-P&VE-PA	Jacobs
1	M-P&VE-VA	Glover

*Plus copy of transmittal letter.

1	M-TEST-F	V. Cornett
1	M-TEST-TP	E. Ward
	M-TEST-TS	J. S. Hamilton
	M-TEST-TS	K. Key
	M-TEST-DIR	Capt. Evans
	M-TEST-DIR	Balch
1	M-COMP-DIR	C. L. Bradshaw
1	M-FE-PM	J. Graham
1	M-SAT-SS	R. O. Barnes
	M-SAT	Dr. P. Farrish
1	M-REL-E	J. D. Beal
1	M-QUAL-S	J. Hamil
1	M-ME-U	W. F. Peak
7	M-ASTR-TSN	R. Currie
	M-CP-P	R. W. Bollinger
	M-LGL	W. E. Guilian
	M-RP-R	J. Downey
2	LO-DF3	D. Cramblit
1	NVPO-S	J. E. Wright
1	NVPO-N	D. W. Sheridan
1	LO-PE	R. C. Hock
	LO-A	Dr. Debus
	LO-F	Col. Bidgood
	LO-S	King
	LO-PC	Body
	LO-V	Dr. Grune
1	LO-VG	Rigell
1	LO-VM	Pickett
1	LO-VE	Williams
	Ofc. Nuc. Sys.	Harold B. Finger
	Ofc. Nuc. Sys.	D. Novik
	SNPO	Harold B. Finger
	SNPO	R. S. Decker
3	SNPO-C	R. W. Schroeder
	SNPO-N	B. P. Helgeson
1	NASA/WOO	Patent Counsel
	AGC/REON	W. C. House
	WANL	H. Faught
	LASL/ROVER Flt. Saf. Ofc.	L. D. P. King